

Optimal design of materials for energy conversion

Thesis by
Lincoln Nash Collins

In Partial Fulfillment of the Requirements for the
degree of
Doctor of Philosophy

The Caltech logo is displayed in a bold, orange, sans-serif font.

CALIFORNIA INSTITUTE OF TECHNOLOGY
Pasadena, California

2017
Defended 9th June 2017

ACKNOWLEDGEMENTS

I would first like to thank my thesis advisor, Kaushik Bhattacharya. He has been an invaluable part of my life over the last six years and I would not have been able to do this without his guidance. Thank you for teaching me how to ask the right questions, the nature of research, and for introducing me to the wonderful world of solid mechanics. I cannot express how grateful I am for being able to work on this fascinating project that has somehow perfectly combined my interdisciplinary interests.

The courses I have taken at Caltech have shaped how I analyze problems and seek solutions. Education will always be an integral component of my life, and I'd like to thank the amazing professors I've been fortunate enough to have. Professors Ravi, Oskar Bruno, Thomas Hou, Brent Fultz, Bill Johnson, and Mark Wise have all shaped how I think and how I present ideas. Thank you, it has been truly inspiring. I would also like to thank Professor Sossina Haile for the guidance and fruitful input to various aspects of my project, and for making sure I don't completely lose ties with experimental work.

I was fortunate enough to have an excellent funding source through NSF, PIRE: Science at the triple point between mathematics, mechanics and materials science, that perfectly matched my research interests and introduced me to a wonderful community. I would especially like to thank Professor Robert Kohn for his discussions on my work, and for the body of literature that laid a framework for my research.

I could go on for pages thanking friends that I have made while at Caltech, and for the lasting ones that have stuck around while I've been buried in graduate studies. I will never forget our adventures, banter, and distractions from work; this would not have been possible without you all. Also, all current and former members of the Kaushik and Ravi groups: thanks for support, ideas, feedback, and inspiration. I will be missing our weekly lunches, and I apologize for consistently making the office smell like coffee around two o'clock.

Words cannot describe how I miss my family, and being able to see them when I can has been essential in maintaining some sanity over the last six years. Thanks for the support and endless love.

Finally, I'd like to thank my girlfriend, Norah. It has been an amazing journey, and I can't wait to see where we go next.

RIP Banzie.

ABSTRACT

The efficiency of fuel cells, batteries and thermochemical energy conversion devices depends on inherent material characteristics that govern the complex chemistry and transport of multiple species as well as the spatial arrangement of the various materials. Therefore, optimization of the spatial arrangement is a recurrent theme in energy conversion devices. Traditional methods of synthesis offer limited control of the microstructure and there has been much work in advanced imaging for these uncontrolled microstructures and optimizing gross features. However, the growing ability for directed synthesis allows us to ask the question of what microgeometries are optimal for particular applications. Through this work, we study problems motivated by metal oxides used in solar-driven thermochemical conversion devices designed to split water or carbon dioxide into fuels. We seek to understand the arrangement of the solid and porous regions to maximize the transport given sources and sinks for the gaseous oxygen and vacancies. Three related problems are investigated with the common theme of understanding the role of microstructure design.

We derive the transport equations for electrons and oxygen vacancies through ceria under an externally-applied electric potential in an oxygen environment using various balance laws and constitutive equations. From this, we obtain various thermodynamic potentials that take into consideration the thermal, chemical, and mechanical state of the material. Accordingly, we obtain a system of partial differential equations describing ambipolar diffusion. We present the applicability of strain-engineering as a way to design systems to improve the behavior of thermochemical conversion devices. We look at an idealized thin film of mixed conductor attached to an inert substrate with a thermal mismatch as a way to induce strain into the film. The resulting impact on equilibrium non-stoichiometry is analyzed using data describing non-stoichiometry in ceria as a function of oxygen pressure and temperature.

The optimal design of material microstructure for thermochemical conversion is addressed from two standpoints: the mathematical homogenization of associated transport models, and from topology optimization. We present the homogenization of coupled transport through porous media consisting of linearized Stokes flow, convective diffusion, and diffusion in the solid phase with interface reaction. Depending on the strength of the interface chemistry, different forms of effective behavior are described at the macroscale, and we gain insight into the impact cell-design and

pore shape has on the behavior.

The topology optimization of a model energy-conversion reactor is then presented. We express the problem of optimal design of the material arrangement as a saddle point problem and obtain an effective functional which shows that regions with very fine phase mixtures of the material arise naturally. To explore this further, we introduce a phase-field formulation of the optimal design problem, and numerically study selected examples. We find that zig-zag interfaces develop to balance mass transport and interface exchange.

TABLE OF CONTENTS

Acknowledgements	iii
Abstract	v
Table of Contents	vii
List of Illustrations	viii
List of Tables	xi
Chapter I: Introduction	1
Chapter II: background	10
2.1 Mixed conductors	10
2.2 Homogenization	17
2.3 Optimal design	23
Chapter III: Continuum transport in mixed conductors	28
3.1 Formulation	28
3.2 Balance laws	29
3.3 Constitutive equations	32
3.4 Consistency with previous literature	35
Chapter IV: Strained Oxides	41
4.1 Formulation	41
4.2 Conclusions	45
Chapter V: Homogenization theory	47
5.1 Reactive-Diffusion Formulation	47
5.2 Convection-Absorption-Diffusion	58
5.3 Summary	67
Chapter VI: Optimal design	69
6.1 Introduction	69
6.2 Formulation	70
6.3 Optimal design problem	74
6.4 Characterization of the optimal design problem	75
6.5 Phase-field formulation of the optimal design problem	79
6.6 Numerical study of the optimal design problem	80
Chapter VII: Conclusions	89
7.1 Future work	91
Bibliography	93
Appendix A: A Γ -convergence result	105

LIST OF ILLUSTRATIONS

<i>Number</i>	<i>Page</i>
1.1 Schematic representation of a single solid oxide fuel cell, from [9].	2
1.2 SOFC cathodes: (a) porous single-phase electronically conductive oxide such as LSM; (b) porous single-phase mixed conductor; (c) porous two-phase composite. From [9]	3
1.3 Three-dimensional reconstruction of a Ni-YSZ anode using focussed ion beam (FIB) and scanning electron microscope (SEM) images. Ni is shown in green, YSZ in gray, and pore space in blue. Connected TPB's are shown on the right as white segments. Off-white segments are disconnected, and therefore ineffective reaction sites. From [3].	4
1.4 3D mesoporous silicon anode material. From [24].	6
1.5 Honeycomb silicon: (a) before lithiation and (b) after lithiation. From [32].	7
1.6 Sample solar thermochemical reactor, from [34].	7
2.1 Lattice diffusion mechanisms (a) via vacancy, (b) via interstitial site and (c) via interstitialcy mechanism.	11
2.2 A sample two-step solar thermochemical cycle using a generic non-stoichiometric metal oxide, MO_y . δ represents the degree of oxygen non-stoichiometry. The right side half-reaction represents the high temperature reduction, and the left side is the subsequent low-temperature hydrolysis.	12
2.3 Example ceria microstructures: (a) as sintered at 1773K (top) and after 500 cycles between 1073K and 1773K (bottom), [35]; (b) inverse opal ceria, [4]; (c) dual-scale RPC ceria, [53].	15
2.4 A matter of length scales. From [81].	18
2.5 The benchmark optimal design problem. From [108].	24
3.1 Schematic arrangement of the mixed conductor.	28
3.2 Total conductivity of samarium doped ceria, (SDC15), presented by [50]. Solid, cross-hair inscribed and open symbols respectively indicate data points obtained using H_2/H_2O , CO/CO_2 and dry O_2/Ar mixtures. Ionic conductivity shown in inset.	39

3.3	Neutral oxygen ambipolar diffusivity samarium doped ceria, (SDC15), as presented by [35].	40
4.1	Idealized mixed conductor thin film problem, with thermal mismatch.	41
4.2	Oxygen non-stoichiometry, δ in $\text{CeO}_{2-\delta}$ measured in 100K intervals using thermogravimetry from [48].	43
4.3	Equilibrium strain effect: $\log(\delta)$ vs. T at $p_{\text{O}_2} = 10^{-11}$ atm for various substrate thermal expansion coefficients.	44
4.4	Equilibrium strain effect: $\log(\delta)$ vs. T at $p_{\text{O}_2} = 10^{-11}$ atm for various reference conditions: (a) varying T_{ref} ; (b) varying $p_{\text{O}_2,ref}$	45
4.5	Residual stress in ceria film for different substrate thermal expansivities, using the same conditions and parameters as in Fig. 4.3.	46
5.1	Generic problem setting.	48
5.2	(a) Hexagonal arrangement of triangles; (b) close packed disks; (c) single disk; (d) single diamond.	57
5.3	Dashed plot corresponds to the rigid case ($\lambda = 1$), and solid is the fully penetrable case ($\lambda = 0$).	58
6.1	The physical setting: chemical species 1 enters through the source $\partial_1\Omega$, diffuses through Ω_1 , is converted to chemical species 2 through a surface reaction at the interface \mathcal{S} , chemical species 2 diffuses through Ω_2 and leaves through the sink $\partial_2\Omega$	70
6.2	Contour plot of \bar{W} for fixed ν, λ . The shaded regions indicate where mixed phase ($\chi \in (0, 1)$) occurs. (a) $k_{11} = k_{22} = k_s = 1, k_{12} = k_{21} = 0.1, (\nu_1 - \nu_2)^2 = 1, \lambda = 0$. (b) Parameters as in (a) except $k_{11} = 5$, (c) Parameters as in (a) except $\lambda = 1$, (d) Parameters as in (a) except $(\nu_1 - \nu_2)^2 = 10$	78
6.3	(a) Square reactor with a source of species 1 on the left and a sink of species 2 on the right. (b) Optimal design (χ) for the parameters in (6.14)).	81
6.4	Designs with volume fraction $\nu = 0.5$ as we vary diffusion coefficients with $\alpha = 0.1, \beta = 5 \times 10^{-5}, k_{12} = 10^{-3} \times k_{11}, k_{21} = 10^{-3} \times k_{22}, d_\chi = 1 \times 10^{-2} - 1.5 \times 10^{-2}, d_u = 7 \times 10^{-4} - 1 \times 10^{-3}, k_s = 1 \times 10^2$	83
6.5	Concentration field u_1 associated with the designs presented in Figure 6.4.	83
6.6	Concentration field u_2 associated with the designs presented in Figure 6.4.	84

6.7	Distribution of reaction zones associated with the designs presented in Figure 6.4; normalized units.	84
6.8	Parameter sweep with $\nu = 0.3$, $\alpha = 0.1$, $\beta = 5 \times 10^{-5}$, $k_{12} = 10^{-3} \times k_{11}$, $k_{21} = 10^{-3} \times k_{22}$, $d_\chi = 1 \times 10^{-2} - 2 \times 10^{-1}$, $d_u = 7 \times 10^{-4} - 2 \times 10^{-2}$, $k_s = 1 \times 10^2$	86
6.9	Designs for a cylindrical reactor with a source of the first species at the inner edge and a sink for the second species at the outer edge. The parameters are in (6.14) except as noted in the rows and columns of the figure. Further, $k_{12} = 10^{-2} \times k_{11}$, $k_{21} = 10^{-2} \times k_{22}$	87
6.10	Periodic square distribution of circular sources and sinks. (a) Unit domain, (b) Resulting design on the unit domain, (c) Periodic design.	88
A.1	A division for the piecewise affine approximation of $\bar{\chi}_{\eta,\epsilon}$	107
A.2	Grouping regions <i>II</i> and <i>III</i> into linear transition regions <i>II'</i>	109

LIST OF TABLES

<i>Number</i>	<i>Page</i>
6.1 Contributions to the energy functional $L(u, \chi)$, the phase field regularization, the flux J_i of each species calculated at the boundary, and the reaction (right hand side of Eq. (6.1) ₁) integrated on the domain for $\nu = 0.5$	85

Chapter 1

INTRODUCTION

The scientific quest for developing novel ways to convert and store energy is an ever-growing effort. It is undeniable that at some point in the not so distant future, the planet as a whole will need to shift away from traditional energy sources to methods that are economical, efficient, sustainable, and clean. Regardless of background, there is no clear answer to solve this grand challenge and proposed solutions are highly interdisciplinary and require collaboration across fields. Experimental and theoretical studies spanning length scales from atoms, to microstructures, and up to power plants continue in the search for changing the energy industry.

The high energy density found in the chemical bonds making up traditional hydrocarbons is one of the most effective ways of storing energy. Contemporary energy conversion and storage methods rely on chemical energy as a way to provide power when necessary. Being that more energy from sunlight strikes the Earth in one hour than the global energy consumed in one year [1], conversion methods utilizing this unbounded energy source have an inherent advantage over other sustainable sources. The conversion of solar energy into useful forms has reached a critical stage where large-scale industrial applications are allowing it to be a relevant method in energy conversion [2]. The conversion of solar energy to electricity via photovoltaic cells is becoming extremely cheap and efficient, and with growing battery technologies the problem of storage is becoming a more relevant issue. Solar energy can also be used as a heat source for fuel cells, where it is converted to chemical energy in a storable fuel, as an energy source for direct generation of fuels through the thermochemical splitting of molecules, or through the combination of light harvesting techniques and chemical energy conversion using a photoelectrochemical cell. Regardless of the proposed solution, countless materials science challenges in these devices must be overcome to shift away from traditional energy sources.

The efficiency of fuel cells, batteries and thermochemical energy conversion devices depends on inherent material characteristics that govern the complex chemistry and transport of multiple species as well as the spatial arrangement of the various materials. Therefore, optimization of the spatial arrangement is a recurrent theme in energy conversion devices. Traditional methods of synthesis offer limited control

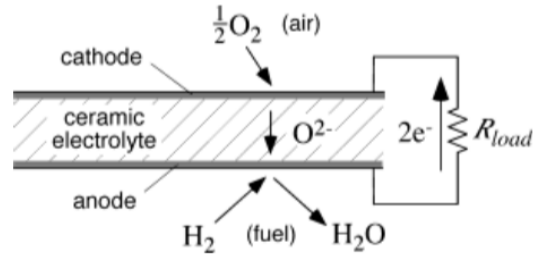


Figure 1.1: Schematic representation of a single solid oxide fuel cell, from [9].

of the microstructure and there has been much work in advanced imaging for these uncontrolled microstructures (e.g., [3]) and optimizing gross features. However, the growing ability for directed synthesis [4, 5, 6, 7] allows us to ask the question of what microgeometries are optimal for particular applications. In this sense we direct the problem to one of optimal design where we are not limited by the imagination in determining new microstructures but instead allow for the underlying physical behavior and optimization techniques to direct architecture and microstructure, and eventually lead synthesis to unprecedented performance.

Solid oxide fuel cells (SOFCs) have been at the forefront of materials science research since the early 2000's because of their promise as a low-cost, clean, and highly efficient energy source hosting a plethora of interesting research topics. The flexible use of different fuels (such as hydrocarbons, biofuels, or coal-derived syngas) and with CO_2 production being marginal, and easily managed, compared to other energy sources are highlights of why industrial scale-up or small-scale, sub-grid, implementation of these devices is so attractive. Material challenges associated with the devices span materials development, microstructural and phase characterization, and multi-scale design and modeling with the goal of increasing reliability at a lower cost [8]. SOFCs are one of many ways to convert chemical energy to electrical energy without the combustion of fuels, and exemplify the application of unique materials for energy production.

SOFC device architecture is sketched in Fig. 1.1. Oxygen enters the system on one side of the membrane and is reduced at the porous cathode. The oxygen ions are then transported through the dense supporting ion-conductive electrolyte to the porous anode, where an oxidation reaction occurs with a reactant fuel to produce H_2O and CO_2 . The electrons released and consumed at the anode and cathode and conducted through an external circuit. Electrode and electrolyte materials are commonly perovskite- or fluorite-structured oxides that rely on large non-stoichiometry (oxygen vacancy concentration) to afford ion conduction and various atomic impurities

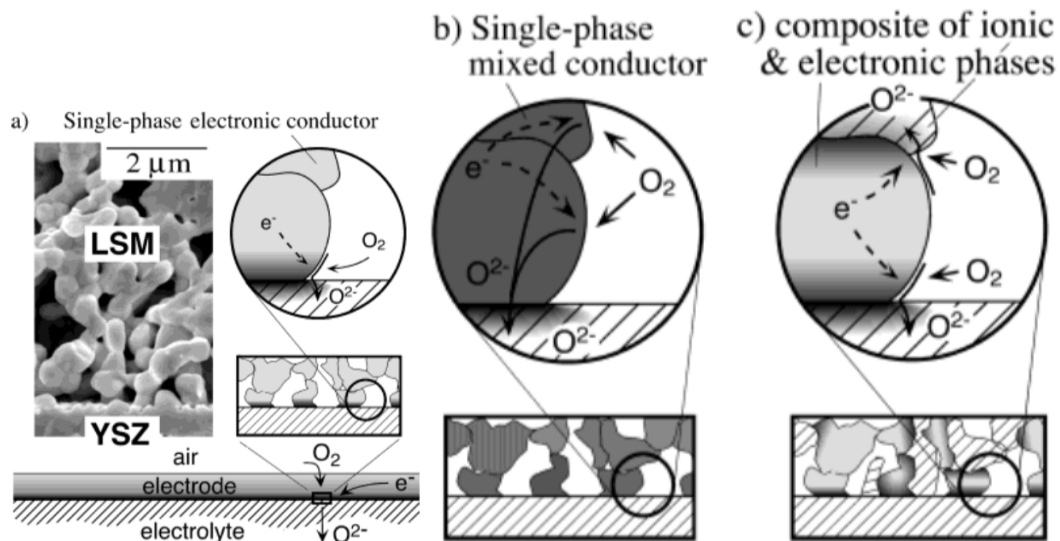


Figure 1.2: SOFC cathodes: (a) porous single-phase electronically conductive oxide such as LSM; (b) porous single-phase mixed conductor; (c) porous two-phase composite. From [9]

(dopants) to increase kinetic behavior [10]. Ytria-stabilized zirconia (YSZ) and ceria-based metal oxides are commonly used as an electrolytes because of their high-temperature stability, general compatibility with other materials used, and ability to effectively transport oxygen ions with minimal electrical conduction [11, 12].

In both porous electrodes, microstructure must be chosen to provide an abundance of electrochemical reaction sites (to promote charge-transfer) and high phase connectivity (for electron and ion conduction, and mass transport in the gas phase). These features are coupled with volume fractions, surface area densities, interfacial curvatures, and phase tortuosities to find the optimal balance between surface reaction and transport [13]. Widely used cathode materials include strontium-doped lanthanum manganite (LSM), strontium-doped lanthanum colbaltite (LSC) and other similar mixed ionic/electronic conductors, eliminating the need for metal electrocatalysts or current collectors [11]. Composite SOFC designs have allow a balance of the thermal-mechanical-electrochemical properties of different materials used [9]. For example, varying mixtures of LSM and YSZ have been examined for use in the cathode with the intent of increasing the contact area between electronically and ionically conductive phases. A full microstructural characterization by [14] proved that the design space has not been completely established.

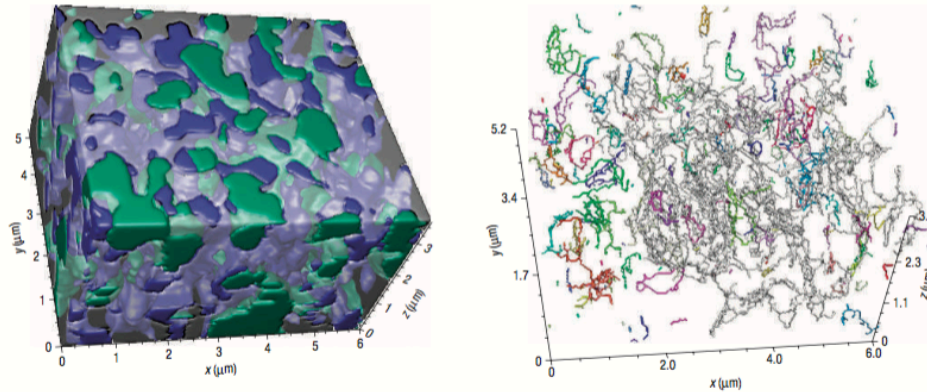


Figure 1.3: Three-dimensional reconstruction of a Ni-YSZ anode using focussed ion beam (FIB) and scanning electron microscope (SEM) images. Ni is shown in green, YSZ in gray, and pore space in blue. Connected TPB's are shown on the right as white segments. Off-white segments are disconnected, and therefore ineffective reaction sites. From [3].

Similarly, the importance of microstructure on anode performance has also been established [15, 16, 17, 18]. Efficient current generation relies on electron conductor (metal), ion conductor (oxide), and reactants (in the pore space) coming together at triple phase boundaries (TPB) [11]. Connectivity is a requirement in each of the phases present: the pore must be well connected to the fuel stream, the Ni phase to the external electrical circuit, and the YSZ phase to the bulk electrolyte [3]. A typical anode is comprised of a ceramic-metallic composite such as YSZ and nickel (Ni), and a typical arrangement can be seen in Fig. 1.3. The choice of these materials depends on the electrolyte used, the operating conditions of the cell, as well as the desired fuel, as reactivity is heavily dependent on all three [8].

The morphology of materials used in lithium ion batteries is of interest from both the theoretical [19, 20, 21, 22] and experimental standpoint [23, 24, 6]. The generalized battery structure takes a similar form to SOFCs, as with many material design constraints. While a battery is being discharged, lithium atoms are oxidized at the anode, releasing electrons to the current collector, leaving ions to travel through an electrolyte and separation membrane to the cathode material where they are reduced. Charging a battery requires external current to reverse the process, requiring lithiation, or intercalation, of the anode material. Mass and ion transport and interface measure in battery electrodes directly impact the storage capacity and rate performance and is an ideal problem for optimization across many length scales. Charge transport, heat conduction and mechanical stresses are all coupled through the battery's use and present complex obstacles in design and materials

development.

Graphite is traditionally used as the anode material because of its abundance, low-cost and stability. The preferable electrochemical behavior of graphite stems from the ability for lithium ions to intercalate in the graphene sheets, as well as mechanical stability and electrical conductivity. However, the recent wave of alloying with silicon in the anode to increase capacity, energy density, and rate has opened countless new design challenges because of the extreme anisotropic chemical expansion upon lithiation, and its low conductivity compared to graphite. Thus, interesting composite designs have been the most successful to ensure mechanical stability and desirable conductivity [25].

Electrolytes are typically composed of lithium salts dissolved in a non-aqueous, organic, solvent to allow for the transport of lithium ions. However, because of interactions with either electrode, electrolyte development is very difficult. A possible solution framework lies in creating solid polymer electrolytes which present ideal manufacturability and high energy density. Nanocomposites have been investigated as a method to increase the ionic conductivity of the solid-state components by numerous additional phases are introduced into the matrix to optimize lithium transport [26].

Cathodes are traditionally made up of transition metal oxides such as LiCoO_2 whose crystal structure allow for easy intercalation of guest ions. Current research is focused on cost reduction and heat management at the anode. In general, the design considerations for lithium batteries can be reduced to dimension reduction, composite formation, doping and functionalization, morphology control, coating and encapsulation, and electrolyte modification [25]. Regardless of cathode or anode, nanostructured materials based on carbon, metal/semiconductor, metal oxides and metal phosphides/nitrides/sulfides show promising applications in lithium ion batteries because of high surface area, low diffusion distance, high electrical and ionic conductivity [27].

The tailoring of material microstructure and nanostructure is not new to energy conversion and storage [7, 26]. Particular designs can range across length scales: from nano-defects to microscale morphologies. Regardless of device, classical synthesis methods usually involve randomized pore structure arriving from sintering processes from a slurry mixture. The development of hierarchical structures and directed porosity affords balancing interfacial reactions and chemical transport to maximize efficiency. In SOFCs, development of new cell structures can reduce

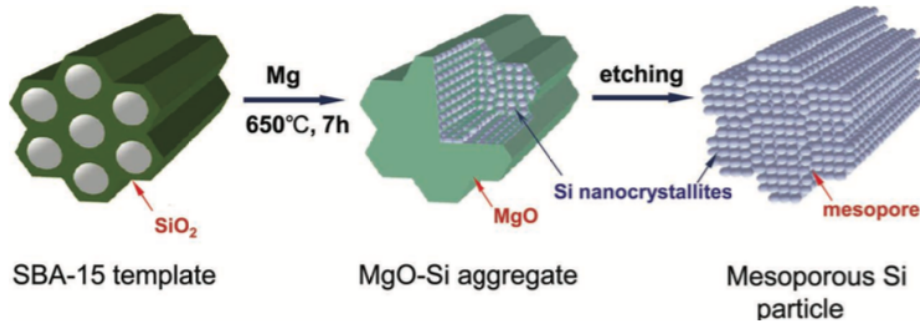


Figure 1.4: 3D mesoporous silicon anode material. From [24].

operating temperatures. For example, it has been shown that 100-nm-thick zirconia-based electrolyte and 80-nm porous Pt electrodes (cathode and anode) could be fabricated with the help of sputtering, lithography, and etching and produce high energy density at a lower temperature [28]. SOFC's implementing microtubular designs have been proposed for low-temperature operation because of high thermal stability under rapid heating, as well as high volumetric power density [16]. Battery anodes can benefit from similar composite designs across a variety of length scales. For example, nanostructured Si-composite materials can be prepared by dispersing nanocrystalline Si in carbon aerogel followed by carbonization [29]. Additionally, macroscopic carbon monoliths with both mesopores and macropores can be prepared by using meso/macroporous silica as a template [23].

Advanced synthesis techniques commonly rely on forming secondary structures as a precursor. For example, in Fig. 1.4, a mesoporous Si anode material was fabricated using a scaffold-like framework. Li et al. [7] review a fascinating mix of hierarchical techniques for application to energy conversion and storage. The process of coating polymer scaffolds, whether they be a collection of spheres or printed network, with slurry before sintering is one route for increased control over microstructure [30]. Direct laser sintering of ceramic materials and metal oxides and other additive techniques has the possibility of designing complex structures for electrodes [31]. An example of a silicon anode designed to accommodate the strains involved with lithiation and produced by photolithography and etching can be seen in Fig. 1.5. Other structures based on porous media, inverse templates, pillars or nanowires with the intent of solid-state battery structures have been reviewed in [33]. Combining design and synthesis methods at a variety of length scales using cellular construction allows for hierarchical materials with prescribed behavior. The design space for SOFCs, batteries, and thermochemical conversion devices goes well

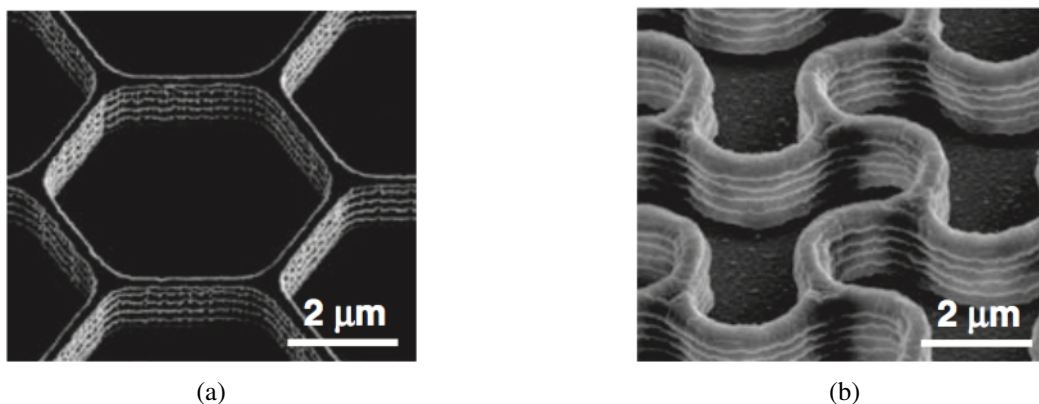


Figure 1.5: Honeycomb silicon: (a) before lithiation and (b) after lithiation. From [32].

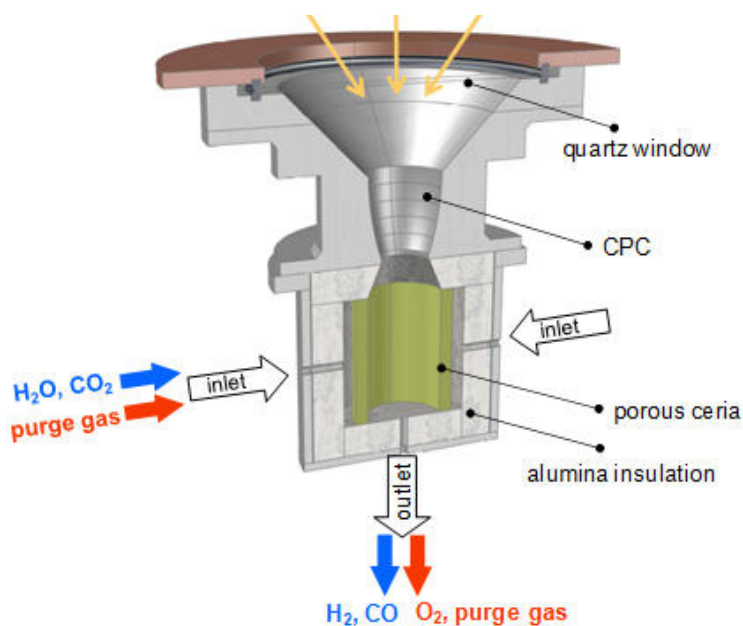


Figure 1.6: Sample solar thermochemical reactor, from [34].

beyond the standard, intuitive, composite structures and is open for optimization.

Through this work, we study problems motivated by metal oxides used in solar-driven thermochemical conversion devices. An example solar reactor, Fig. 1.6, has been developed and tested for the conversion of H_2O to hydrogen as a sustainable fuel source [34]: These conversion devices consist of porous, two-phase, material (solid oxide and pore) where reactions at the surface create oxygen in the carrier gas in the pores and bound oxygen in the solid oxide; the oxygen diffuses through the carrier gas in the porous region and bound oxygen diffuses through the solid oxide. Various metal oxides are possible candidates for these processes, but nonsto-

stoichiometric cerium oxide, especially when doped, display applicable thermodynamic and kinetic traits [35]. Details of these materials and processes will be the focus of Sec. 2.1. Alternate methods for generation of hydrogen from water using solar radiation can be categorized generally by their procedure [36]: solar thermolysis, solar thermochemical cycles, solar reforming, solar cracking, and solar gasification. The latter three require input from fossil fuels, and the associated sequestration of CO_2 . However, all offer preferable routes to energy production over the traditional, combustion-based, methods. Similar effort has been put into developing photocatalytic cycles for the conversion of CO_2 into combustible hydrocarbons, as reviewed by [37]. Solar-driven thermochemical approaches to CO_2 and H_2O provide an attractive path to solar fuel production at high rates and efficiencies in the absence of precious metal catalysts, and the relatively simple reaction framework makes them ideal candidates for modeling and optimization.

There is a common thread between these three examples: they all use nonstoichiometric, ionically conductive ceramic materials where the effectivity of the device is largely dependent on the microstructural design of the material. We focus on thermochemical conversion as a model energy conversion system to study because of the relative ease of modeling, and the low complexity of material integration. We seek to understand the arrangement of the solid and porous regions to maximize the transport given sources and sinks for the gaseous oxygen and vacancies. Three related problems are investigated with the common theme of understanding the role of microstructure design of mixed conductors for their application to devices like those depicted in Fig. 1.6. Our goal is develop a framework for designing materials that is not specific to one application, but can be easily modified to optimize any energy conversion device.

The first problem lies in exploring the applicability of strain-engineering as a way to design systems to improve the behavior of thermochemical conversion devices. Many of the mixed conductors mentioned, under reducing conditions, expand as vacancy defects are introduced into the crystal structure, and there is a strong coupling between the chemical, electrical, thermal, and mechanical environments of the material. We find that inducing a strain into an ionic conductor allows for the equilibrium vacancy concentration to be tailored. In Ch. 3 we derive a thermodynamic potential describing the concentration of ionic and electronic species in mixed conductors considering the environmental chemistry and coupling transport with the associated strains associated with varying nonstoichiometry in the material.

Then in Ch. 4, we look at an idealized thin film of mixed conductor attached to an inert substrate with a thermal mismatch as a way to induce strain into the film. The resulting impact on equilibrium non-stoichiometry is analyzed using data describing non-stoichiometry in ceria as a function of oxygen pressure and temperature.

Then, the optimal design of material microstructure is addressed from two standpoints: one is from the mathematical homogenization of the transport models associated with thermochemical conversion, and the other is from topology optimization. Homogenization is a mathematical technique in which studying a periodic, cellular, structure with a fine length scale yields volume averaged behavior of the media at the macroscale. We gain insight into the impact cell-design and pore shape has on the behavior of materials in energy conversion devices. By understanding this connection, the optimal design of cell-structures can be properly examined. In Ch. 5, we present the homogenization of coupled transport through porous media consisting of linearized Stokes flow, convective diffusion, and diffusion in the solid phase with an interface reaction. Depending on the strength of the interface chemistry, different forms of effective behavior are described at the macroscale.

Topology optimization is a broad description of methods to determine the best arrangement of material to meet a prescribed measure of performance. An objective function is chosen and instead of optimizing over parameters, we instead optimize over designs. Chosen physical models are then implemented as constraints and become the guide to designing materials, rather than intuition or synthesis. In Ch. 6, we look at the topology optimization of a porous material, where two chemical species each reside in separate phases (pore space and solid), and undergo an interfacial conversion reaction. We analyze both the reactive-diffusive transport model in this setting, as well as optimal design problem associated with maximizing through-put through a generalized device. The optimization is then implemented numerically to determine designs under varying parameters.

We start by presenting relevant background information on the metal oxides used in these thermochemical conversion systems, the experimental and theoretical efforts to studying them, and the current status of morphological studies in Ch. 2. An introductory description to mathematical homogenization theory and other efforts in studying transport problems follows. Finally, a description of the mathematical theory of topology optimization is described, along with relevant examples and previous studies.

Chapter 2

BACKGROUND

2.1 Mixed conductors

The ability of various metal oxides to conduct ionically and electronically make them invaluable for countless applications ranging from electrodes in fuel cells, selective membranes, sensors, oxygen generators and catalysts because of their unique electrochemical behavior [38]. For example, the 2020 Mars rover will include a device, MOXIE, consisting of a "reverse fuel cell" utilizing a ceramic mixed conductor to split CO_2 from the atmosphere for oxygen generation [39]. Oxygen separation membranes consisting of fluorite-based materials, like stabilized zirconia, or perovskite structures utilize ionic conduction to pull oxygen from a source gas [40]. In these applications, we have a fascinating interplay of different transport regimes, chemical reactivity, thermal conduction, and mechanical behavior all coming together for a specified task. The microscopic design of the metal oxides is directly tied with its behavior, and subsequent application and efficiency. Large temperatures, fluctuating chemical environments, electric fields and mechanical stresses lead to varying degrees of oxidation or reduction in these materials.

For mixed conductors, low-oxygen, high-temperature reducing conditions translate to a partial nonstoichiometry of the lattice structure where charged Schottky point defects are created simultaneously with a charge-balancing electronic defect. The vacancies are created at lattice sites in the matrix where an oxygen previously resided that was removed through reduction. The shift in non-stoichiometry can result in phase transitions in some metal oxides, or it can be a continuous change in chemical composition where the lattice structure remains intact. The creation of these vacancies aids in the diffusive transport of atoms (or vacancies) through the bulk resulting in ionic conductivity, and the formation of electrons results in n-type electrical conductivity. In n-type conductors, neutral levels near the conduction bands are ionized to free an electron into a conduction band, acting as an electronic species. The movement of atoms can be through a variety of mechanisms, see Fig. 2.1, but the vacancy mechanism is most relevant in this behavior [40]. In vacancy mechanism, the atom in question fills a vacancy, thereby creating a new one in its previous location. Interstitial diffusion requires jumping between neighboring lattice-site atoms

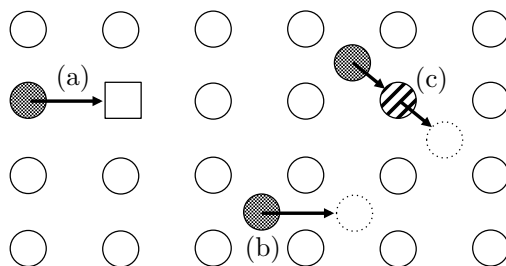


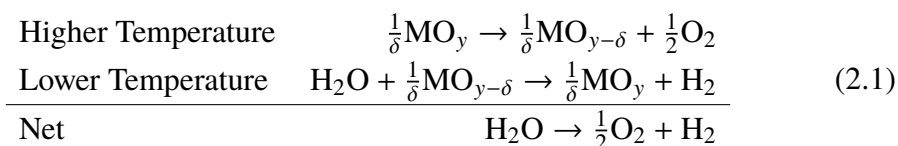
Figure 2.1: Lattice diffusion mechanisms (a) via vacancy, (b) via interstitial site and (c) via interstitialcy mechanism.

to a neighboring interstitial, and thus requires overcoming a large energy barrier for the the jump. Finally, it is possible for an interstitial atom to "bump" a neighboring lattice atom to a near-by interstitial site through the interstitialcy mechanism, again at the expense of a large energy barrier. Factors effecting a metal oxide's ionic and electronic conductivity are primarily based on the crystal structure and the bandgap structure, respectively. Thus, dopants and non-stoichiometry impact the ionic and electronic conductivity and constitutes a large portion of mixed conductor research.

This complex behavior and the stability of metal oxides over a wide range of conditions is essential for many applications [41, 42, 15, 43]. Formulating relevant mathematical models to explore this connection between physical behavior and material morphology offers a method to engineer and tailor new materials, but to also explore new applications and devices. Recent advances made in the materials research community indicate many possible candidates for these applications, and lend themselves to advanced synthesis techniques facilitating directed architecture, where significant improvements can be made [44].

Energy conversion

Application of mixed ionic-electronic conductors (MIECs) to thermochemical energy conversion offers a feasible route of sustainable energy production [45, 34, 35, 46]. As depicted in Fig. 2.2, a porous, redox active oxide is cyclically exposed to inert gas at high temperature, generating oxygen vacancies in the structure, and reactant gas (H_2O , CO_2), at moderate temperature, releasing fuel upon reoxidation of the oxide. The process for splitting water can be described as the combination of the two reactions:



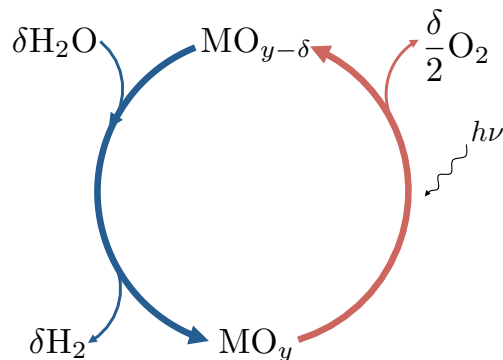


Figure 2.2: A sample two-step solar thermochemical cycle using a generic non-stoichiometric metal oxide, MO_y . δ represents the degree of oxygen non-stoichiometry. The right side half-reaction represents the high temperature reduction, and the left side is the subsequent low-temperature hydrolysis.

A similar set of half reactions describes the the process for CO_2 , albeit with many different products. A mixture of hydrocarbons is produced when combining H_2O and CO_2 including CH_4 , CH_3OH , or CO for syn-gas, and opens this type of thermochemical conversion to a variety of applications and post-processes for energy production [47]. Similar processes were examined in the 1970's with the intent of using the heat from nuclear reactors to activate these reaction pathways. Since then, research has centered on increasing the efficiency, longevity, and practicality of thermochemical conversion and the materials involved. Metal-metal oxide systems have been around since the initial research into these processes and have theoretically large conversion rates, but because of the high temperatures required and the low stability of the phases involved, many alternatives have become the focus of research. One such alternative is the application of non-stoichiometric oxides to these conversion processes. Despite the lower conversion rates (a complete phase change isn't required), the increased stability and electrochemical activity make them an attractive energy source. The lack of complex and expensive catalyst systems and full use of the entire solar spectrum separate these devices from many other photo-based energy sources.

One such candidate is ceria, cerium oxide. Its electrochemical behavior is well-suited to this application, and the relative abundance of cerium globally makes scale-up and implementation feasible [34, 48]. Ceria, CeO_2 , takes on a cubic fluorite structure, with tetrahedral oxygen atoms residing within an FCC base lattice of cerium in the +4 oxidation state. Under reducing conditions, i.e. low ambient oxygen and temperatures above $\sim 1000^\circ C$, the non-stoichiometry can reach $\delta \sim 0.25$

[49]. The application of ceria to thermochemical conversion has been successfully demonstrated on the material scale and the reactor scale, where productivity of up to 11.8 ml of hydrogen per gram of ceria at 6.2 ml per gram per minute has been recorded [45, 34]. Thermal losses from conductive and radiative heat transfer limit the efficiency and cycling rates. Thermodynamic analysis based solely on the material properties of CeO_2 , the higher heating value of one mole of hydrogen, and the total heat input to the cycle indicate that 16 to 19% efficiency of converting solar radiation and water to hydrogen are attainable, even without heat recovery [35]. Steinfeld presents a similar analysis for reactor-scale processes, presenting the ideal efficiency, $\eta_{\text{exergy, ideal}}$, depending on solar absorption and the ideal Carnot efficiency:

$$\begin{aligned}\eta_{\text{exergy, ideal}} &= \eta_{\text{absorption}} \times \eta_{\text{Carnot}} \\ &= \left[1 - \frac{\sigma_{SB} T^4}{I\tilde{C}} \right] \times \left[1 - \frac{T_L}{T} \right].\end{aligned}$$

Here, \tilde{C} represents the mean solar flux concentration ratio, T_L is the temperature of the thermal reservoir, and σ_{SB} is the Stefan-Boltzmann constant. By maximizing this efficiency with respect to temperature, with $\tilde{C} = 5000$, they present $T_{\text{optimum}} = 1507$ K, with a maximum theoretical efficiency of 75% [36]. However, with experimental efficiencies found two order of magnitude less, $\sim 0.7\%$ [34], much is left to be optimized at the material and reactor scale. Thermal stability, cycleability, and mechanical stability are only some of the issues found in the high-temperature application of metal oxides for thermochemical conversion.

Experimental efforts

Current research in the application of ceria-based materials to thermochemical conversion processes centers around increasing the kinetic and thermodynamic response of the materials. At the material level, investigations are being done in adding dopants to increase the equilibrium vacancy concentration (thermodynamic behavior) and the electrochemical conductivity (kinetic behavior). The non-stoichiometry depends on the temperature and oxygen environment, and is controlled by the enthalpy and entropy change involved with the reduction, and measures the total fuel productivity of material. Thermogravimetric analysis (TGA) consists of measuring (by mass), the non-stoichiometry as a function of temperature and oxygen environment at equilibrium. The kinetic behavior is determined by the diffusivity of oxygen (and/or) vacancies through the bulk with a coefficient D_{chem} , and a surface exchange constant k_s describing the ability to uptake and release oxygen. D_{chem} is

a material property dependent on the oxygen activity and temperature, whereas k_s also depends on the gas phase composition, surface morphology and surface composition. Electrical conductivity relaxation (ECR) experimentally provides these intrinsic material properties [50, 51, 52]. The electrical conductivity of a known-geometry of mixed conductor is dependent on the vacancy concentration, and by fitting analytical transport models to an experimental set-up, the kinetic behavior can be obtained by exposing samples to a step-change in oxygen environments [38]. The models associated with these experimental measurements will be presented in a generalized framework in Ch. 3.

Improving the efficiency of the thermochemical conversion processes is an interdisciplinary task, and is a unique opportunity to explore new methods both experimentally and theoretically at the material design scale. The efficiency of materials in this setting is determined by the kinetic behavior described, where there is a balance between bulk transport, and interface chemistry, and direct relation between efficiency and morphology has been examined [4]. Thus, porous ceramics are being used to increase the kinetic and thermal response of these materials by increasing the specific surface area available for heterogenous reaction, the importance of the material pore structure becomes a relevant problem. In theory, one should a balance between gas flow, interface exchange, and bulk flow will be optimized for improving the conversion efficiency. Varying degrees of controlled synthesis have been examined already, see Fig. 2.3. As-sintered ceramics are usually a random pore network on the 10 μm -mm scale with minimal surface area per volume, leaving significant room for improvement. The directed-synthesis method of reticulated porous ceramics (RPC) offers one degree more control of pore structure and specific surface area. Work done in the Steinfeld group presents both direct pore level simulations of transport and reactions, as well as an experimental framework for construction of these ceramic foams [30]. A random polymer foam is coated in a ceramic slurry so that during the sintering process, a skeleton of the foam is left behind comprised of the desired metal oxide. They present a dual-scale, hierarchical, RPC where a mm-size foam network is comprised of μm scale porous ceramic [53]. The larger strut structure offers good thermal conduction and mechanical support, whereas the smaller length scale maximizes the specific surface area. Inverse opal designs offer yet another method for directed synthesis, where PMMA beads are embedded in a slurry, and thus sintering leaves a highly-ordered honeycomb ceramic structure with tunable length scales [44, 4]. Additional shapes and construction methods have been explored at differing length scales in all areas of energy conversion and storage, and

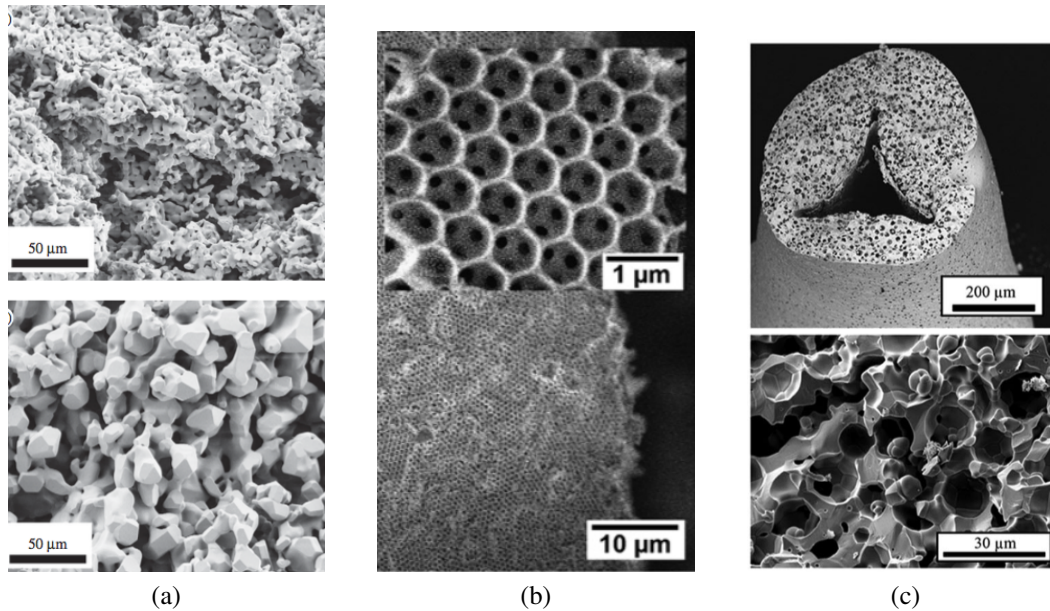


Figure 2.3: Example ceria microstructures: (a) as sintered at 1773K (top) and after 500 cycles between 1073K and 1773K (bottom), [35]; (b) inverse opal ceria, [4]; (c) dual-scale RPC ceria, [53].

couple well with the current attention to additive manufacturing methods [31, 54, 26, 7, 13, 20, 14, 55, 5].

Modeling

There is a wide-spectrum of current modeling efforts in current research. One side of the spectrum centers on both analytical and numerical ambipolar diffusion modeling essential to ECR and other characterization methods. The classical of theory of transport in mixed conductors is in-line with diffusional transport in solids, and is usually described with electrochemical potentials describing the electronic and ionic species in the material [56, 38]. The thermodynamic and kinetic behavior of these materials are well-studied with application to ceria [52, 35, 57, 46], and the relevant relations describing the mass and charge transport occurring through the bulk will be reviewed in Ch.3. Smaller scale studies through density functional theory (DFT) is a common theme in concurrent research as well [58]. Transport, and equilibrium concentrations, can be explained using an electrochemical potential for the relevant species. There is a variety of different methods for deriving these thermodynamic potentials, and in the work presented in Ch. 3 we take the classical continuum mechanics standpoint, following the rationalizations presented by Coleman and Noll [59], with an extension to the relevant chemical behavior.

On the other end of the spectrum is the full-scale coupled transport through porous mixed conductors [60, 61, 62, 63, 64]. By considering fluid-flow, interface reaction, and solid-state transport in reconstructed pore morphologies, the effective behavior of known structures can be analyzed numerically, and the volume-averaged behavior for various structures has indicated a strong connection between microstructure and energy conversion efficiency [65]. Tomographic reconstructions used in these pore-level studies yield porosity, specific surface area, pore size distribution, thermal conductivity, convective heat transfer coefficient, permeability, and tortuosity. Haussener et al. go on to examine tailored foam designs over this parameter space, as well as examine artificial structures of bimodal spherical distributions of pores [63, 64, 62]. A formal extension of these modeling techniques is presented from the homogenization viewpoint in Ch. 5 to address the averaged reactivity and multi-physics transport through mixed conductors.

Strain engineering

As ceria and other transition metal oxides are reduced at high temperatures, the decrease in oxygen content in the metal matrix and the formation of a vacancy and electronic species changes the average lattice parameter of the material. As the surrounding atoms relax around the vacancy, a continuous change in average bond length occurs in the material, and a resulting macroscopic stress-free strain is observed

$$\varepsilon = \frac{\Delta L}{L_0},$$

that varies with both temperature (using the typical coefficient of thermal expansion) and the surrounding oxygen environment as described through a coefficient of chemical expansivity [66, 67, 68, 69]. At the strongly reducing conditions required for thermochemical conversion, high temperature and low p_{O_2} , the stress-free strains associated with thermo-chemical expansion can result in potentially large, and detrimental, residual stresses in mixed conductors like ceria. Through their seminal series of papers, Larche and Cahn established the theory behind these compositional stresses in metals [70, 71, 72, 73]. Both applied stresses, as well as these "self"-stresses, are correlated with the diffusive transport of species through the material, and can be described using thermodynamic potentials. Accordingly, the interplay of stress and transport behavior of metal oxides and their mechanical stability are relevant concerns for applications in thermochemical conversion and solid oxide fuel cell systems [74]. The numerical values of this coefficient of chemical expansion (α_c), have been investigated experimentally [75, 76] as well as

numerically through DFT studies, e.g. [41], and indicate a strong involvement of the oxygen environment on the mechanical behavior of ceria. The associated Young's modulus also varies with composition significantly, and is commonly attributed to weakening inter-atomic forces due to the increased concentration of point defects [77, 67, 68]. The thermodynamic potentials describing this behavior are natural extensions of the typical notion of chemical potential, as well as the electrochemical potential commonly used in MIEC modeling [78, 79]. A derivation of these thermodynamic potentials, and the corresponding transport behavior is presented in by Ch. 3.

The concept of strain engineering relies on using an induced strain in a material to tailor its performance for a certain application. We can consider using the notion chemical expansion to alter the behavior of nonstoichiometric metal oxides for uses in thermochemical conversion devices. Inducing a mechanical stress can be performed by attaching a film onto a substrate with a thermal expansivity mismatch, a lattice mismatch, or by applying a local mechanical stress. On one side, using an induced stress to increase the rate of hydrogen production and oxygen conductivity offers a pathway to increase efficiency. Yildiz et al. [77] fully review the current efforts examining the kinetic impacts of strain engineering, spanning molecular-scale models to experimental measurements and material architectures [80]. In theory, as the material is strained, the energetic barriers of reaction and diffusion kinetics are altered as the inter-atomic potentials are shifted. The oxygen defect formation enthalpy, migration energy barrier, adsorption energy, dissociation barrier, and charge transfer barrier are all decreased as the strain increases. On the other side, using the state of stress in the material to increase the equilibrium non-stoichiometry in thermochemical conversion is yet to be investigated and offers a pathway to increase the net fuel produced per cycle for energy conversion devices. We pose the problem as a model problem where a thin-film of mixed conductor (ceria) is attached to an inert substrate with a different thermal expansivity, and examine the resulting impact on equilibrium non-stoichiometry using traditional TGA data [48]. This can be approached by just considering chemical equilibrium of the system (see Ch. 4), or by exploiting the thermodynamic potentials described previously (Ch. 3).

2.2 Homogenization

The behavior of the observable continuum is governed by physics acting on a much smaller (and larger) length scales. Considering the scene depicted in Fig. 2.4, we see that a wood beam supporting a mass on a brick wall is actually comprised

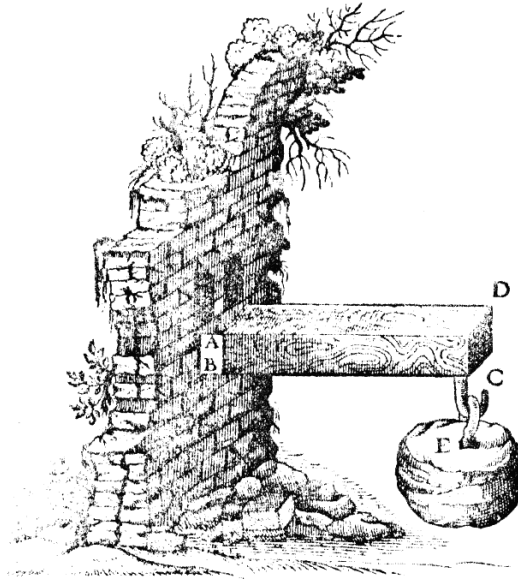


Figure 2.4: A matter of length scales. From [81].

of elemental units: the individual bricks, the sediment and grains comprising the bricks, the mortar, the wood grains and fibers, the individual cells making up wood. The mass itself is transferred over all over these elemental units, but at our length scale, we see all of these entities as an averaged continuum. Studies in homogenization seek to find a connection between these length scales; how does the shape and composition of the bricks and wood cells impact their ability to hold the mass at E ? Homogenization theory seeks macroscopic descriptions of behavior and material behavior, and has applications in countless areas including porous media, composites, damaged material, and optimal design [82, 83]. The concept of designing materials and composites hierarchically has the potential to open new realms of applications and properties. For example, studies have been extended to optimal design and homogenization in the thermomechanical setting with three separate phases displaying metamaterial behavior and unique mechanical responses [84, 85]. Coupling the microscale and macroscale designs through homogenization and optimization is a key to advancing engineering and fabrication over a multitude of length scales [86].

Studies are not limited to solely the structural problem, but instead, mathematical models describing behavior at the microstructure are averaged to an "effective behavior" at the macroscale in the asymptotic sense, where a description length scale, ε , vanishes. In other words, as we consider multi-phase composites or materials with finer and finer mixtures of the materials involved to the point of acting like an ideal

homogenous material. Thus, in the mathematical sense, homogenization theory focussed on the asymptotic analysis involved with ordinary and partial differential models with fast-oscillating behavior in coefficients (such as electrical, thermal, or chemical conductivity, elasticity coefficients etc.) and thus, in solutions. In light of studying mixed conductors and porous ceramics, we focus on the homogenization of transport equations, namely combining conductive-diffusive transport and linear fluid flow with reaction to address the problem of porous ceramics for energy conversion. Tracking the gaseous species traveling through the pore space requires a coupled problem of linear Stokes flow, and convective-diffusion with interface reaction. In the solid matrix, bulk diffusion describes the movement of relevant ions and/or electrons, both coupled to the gas phase through the interface. A goal of the homogenization process is examining the coupling between these different models that comes about through considering different scalings between each regime as the effective behavior is obtained asymptotically.

Two-scale asymptotics

The primary tool we will implement is the mathematical rationalization of length scales and convergence methods developed by [87, 88] and others, and made rigorous by Allaire [89] and Tartar [90]. To illustrate the concept of two-scale asymptotics, we consider a periodic PDE-system over a unit-cell of a periodic (or quasi-periodic) medium in Ω with the operator L_ε depending on the layout in the unitcell, with an associated family of solutions u_ε :

$$L_\varepsilon u_\varepsilon = f \text{ in } \Omega,$$

with some appropriate boundary conditions. The process of homogenization [82, 88, 91] implies that there exists some macro-scale behavior that describes, in the limit of $\varepsilon \rightarrow 0$, that somehow $u_\varepsilon \rightarrow u$ and we have a homogenized operator \bar{L} :

$$\bar{L}u = f \text{ in } \Omega.$$

The two-scale approach [92, 91, 87, 88] creates two coordinate systems: one tracking the macroscopic behavior, x , and another for the microscopic behavior $y = \frac{x}{\varepsilon}$. The method is built on the ansatz that solutions can be written

$$u_\varepsilon(x) = u^0(x, \frac{x}{\varepsilon}) + \varepsilon u^1(x, \frac{x}{\varepsilon}) + \varepsilon^2 u^2(x, \frac{x}{\varepsilon}) + \dots \quad (2.2)$$

with $u^i(x, y)$ periodic in y . Inserting this expansion into the governing problem at hand, terms are collected depending on the order of ε . Volume averaging, at

some point in the process, leads to the desired homogenized behavior dependent, u^0 on the microstructure seen at the y length scale in a cell problem. In general, this asymptotic examining is strictly formal, and more advanced techniques are required to prove the transition $u_\varepsilon \rightarrow u$. In the problems presented in Ch. 5, we stick to the formal examination as proofs explaining the desired convergence are well documented. In addition to Allaire's work on the subject, [89], the "energy-method" of Tartar complements other convergence methods including G -convergence (and G -closure), explaining the set of possible homogenized properties, H -convergence, and H -measures [93], compensated compactness [94], and Γ -convergence describing the coupled convergence of energy functionals and associated minimizing sequences [82].

In general, rigorous methods rely on analysis of the weak formulation of a problem. In a rudimentary sense, we can imagine multiplying the governing PDE but a suitable, and creative, choice of test function and then integrating over the domain. The key is then passing to the limit $\varepsilon \rightarrow 0$, which is made possible for the weakly converging sequences by exploiting the compensated compactness from the test functions. The efforts mentioned previously, as well as Allaire's two-scale method provide ways in dealing with this convergence, and the assurance of the homogenized behavior, and solutions. When dedicated to the periodic setting, two-scale convergence allows for efficient analysis and is centered around the following theorem.

Theorem 2.2.1 (From [89]). *Let u_ε be a bounded sequence in $L^2(\Omega)$, with $\Omega \subset \mathbb{R}^N$, open. There exists a subsequence, denoted by u_ε , and a function $u^0(x, y) \in L^2(\Omega \times Y)$ ($Y = (0, 1)^N$ is the unit cube cell) such that*

$$\lim_{\varepsilon \rightarrow 0} \int_{\Omega} u_\varepsilon(x) \psi\left(x, \frac{x}{\varepsilon}\right) dx = \int_{\Omega} \int_Y u^0(x, y) \psi(x, y) dx$$

for any smooth test function $\psi(x, y)$, which is Y -periodic in y . Such a sequence u_ε is said to two-scale converge to $u^0(x, y)$.

For the convergence of the ansatz, Eq. 2.2, a corrector result is needed:

Theorem 2.2.2 (From [89]). *Let u_ε be a sequence that two-scale converges to $u^0(x, y)$. Then, u_ε weakly converges in $L^2(\Omega)$ to $u(x) = \int_Y u^0(x, y) dy$, and we have*

$$\lim_{\varepsilon \rightarrow 0} \|u_\varepsilon\|_{L^2(\Omega)} \geq \|u^0\|_{L^2(\Omega) \times Y} \geq \|u\|_{L^2(\Omega) \times Y} \quad (2.3)$$

Furthermore, if equality is achieved in the left part of Eq. 2.3

$$\lim_{\varepsilon \rightarrow 0} \|u_\varepsilon\|_{L^2(\Omega)} = \|u^0\|_{L^2(\Omega) \times Y},$$

and if $u^0(x, y)$ is smooth, then we have

$$\lim_{\varepsilon \rightarrow 0} \left\| u_\varepsilon(x) - u^0\left(x, \frac{x}{\varepsilon}\right) \right\|_{L^2(\Omega)} = 0.$$

These two theorems provide a rationalization of the ansatz that is used in many formal studies on homogenization, and will only be presented here for validity of the methods used in this work. The rest of the two-scale method proceeds by multiplying the microscale PDE by a suitably smooth Y -periodic test function, integrating by parts and then passing to the two-scale limit and obtaining the variational form of $u^0(x, y)$. Volume averaging $u^0(x, y)$ leads to the macroscopic field as well as the effective properties of the material as a function of the cell topology. These formal methods can be extended to quasi-periodic oscillations in compositions, and there are various convergence theorems examining such problems that offer more accurate descriptions of real composites, or graded materials. [95]

Previous transport problems

Taking the problem addressed in Ch. 3 and looking at it from a homogenization standpoint requires examining relevant transport models in porous media. One class of problems lies in the convective-diffusion transport with chemical reaction regime. Various formal and rigorous homogenization studies have examined these problems in the past, and the most relevant results will be presented in Ch. 5. The simple conductivity problem is well established [87, 96, 97] and provides a framework for extending to the non-linear case and for involving multiple chemical species and reactions. Competing processes of diffusion, convection, adsorption, and reaction have all been analyzed in various settings and couplings, including porous media, fractured material, multi-phase composites, etc. [98, 99].

The question of adding convective behavior has been addressed previously including applications involving time-varying flow [100, 101, 102]. Most results presented can be formally examined with the two-scale approximation technique, and to account for the time-dependence, a drift behavior is built into the asymptotic expansion of solutions. Interfacial effects including adsorption, interfacial reaction, and interfacial resistance rely on prescribing an internal boundary condition within the unit cell, describing the flux and/or field value dependent on an arbitrary, possibly non-linear, function. The interface kinetics discussed in Ch. 3 coincide with an "im-

perfect interface" in the conduction problem, and in keeping track of separate fields in the different phases, the selective diffusion process can be modeled accurately [103, 104]. Here, the temperature of concentration fields are taken to be separate in each material phase, as the interface can cause a jump in the temperature and flux. In the electrical setting, the current has a discontinuity across the interface, whereas the potential remains continuous [105]. Results carry over to studies of diffusion under pressure in partially fissured material [106], and the homogenization results couple well with traditional composite theory. Lipton and Talbot [107, 105] present effective conduction behavior for fine-scale materials and the associated bounds on effective behavior. A very similar asymptotic examination of two-species diffusion described by generalized Poisson-Nernst-Planck (PNP) equations, and an unscaled interfacial Butler-Volmer exchange was examined by Ciucci and Lai for developing a micro/macro model for lithium battery models [22]. These previous studies lay a foundation of homogenization theory to build off, and the methods can be adapted to the thermochemical system in question.

One of the classic derivations from homogenization theory is obtaining Darcy's Law from linearized Stokes-flow through periodic porous material. [87, 88] The general framework relies on the same formal approach described: expanding all the relevant fields in a series dependent on orders of ε and collection the resulting array of equations to determine the homogenized behavior. The Stokes equations for flow through the pore space are denoted

$$-\nabla p + \Delta b + f = 0 \quad \text{in } \Omega_p^\varepsilon \quad (2.4)$$

$$\nabla \cdot b = 0 \quad \text{in } \Omega_p^\varepsilon \quad (2.5)$$

$$b = 0 \quad \text{on } \Sigma \quad (2.6)$$

where b (the velocity vector) and p (the pressure) are unknown functions defined over our domain Ω_p^ε that is scaled with ε , with interface Σ , and a possible body force f . Following the traditional two-scale expansion method, Darcy's law can be derived:

$$\tilde{b}_j^0 = K_{ij} \left(f_i - \frac{\partial p^0}{\partial x_i} \right),$$

describing that the volume averaged (denoted by $\tilde{\cdot}$) velocity is proportional to the gradient of the pressure at the macroscale. The tensor K_{ij} describing the permeability is dependent on the fine-scale structure of the unit cell, and is comprised of solutions to the unit-cell problem obtained in the ε ordered array of equations. A formal derivation of this will be presented in Ch. 5.

2.3 Optimal design

In considering the interplay between material microstructure and the electrochemical behavior required for application to thermochemical conversion devices, synthesis techniques and the resulting morphology are relatively uncontrolled. The various attempts at controlling the porous topology are limited by random structure and tunable parameters are chosen based on intuition and a prescribed pore shape. Optimization methods of design exploit physical models describing the behavior of a material under prescribed boundary conditions to determine the ideal material arrangement with a given goal in mind. It leads to two widely used methods, topology optimization (e.g. [108]) and shape optimization (e.g. [109]). Shape optimization fixes the topology of a domain and determines the ideal morphology of the inclusions or boundaries between phases. The resulting sensitivities used are well established in theory and in numerical studies, but the common short-coming is that the topology of an ideal arrangement is not known beforehand. For example, in optimal design of elastic plates, the solution is to have an increasing number of thinner plates for optimal behavior [86], which motivates the introduction of microstructure into design. Homogenization theories similar to those presented in Ch. 5 carry over to the optimal design realm seamlessly in this setting.

Topology optimization is the more generalized form of these approaches, and seeks to address the limitations of shape optimization by allowing for optimization to be carried out over both the shape of the material and the topology. Originally established in the seminal paper from Bendsøe and Kikuchi [86], there is a growing body of literature applying the methods of topology optimization to new areas and physical regimes. The traditional benchmark example of optimal design seeks to minimize compliance for a prescribed load by arranging material in a fixed domain. A sketch of this problem and the resulting configuration can be seen in Fig. 2.5. Topology optimization uses finite element or finite difference analysis to discretize the domain, where the material parameters vary over each voxel. Even with varying degrees of filtering and post processing, there is still the possibility for intermediate densities to arise in the result. This is seen in Fig. 2.5 as the gray regions, and represents the formation of material with microstructure, or a composite of two base materials.

Mathematical theory in the search for optimality

It is understood that the underlying problem of optimal design is ill-posed in that the resulting designs often lie outside of the set of "classical admissible designs" and

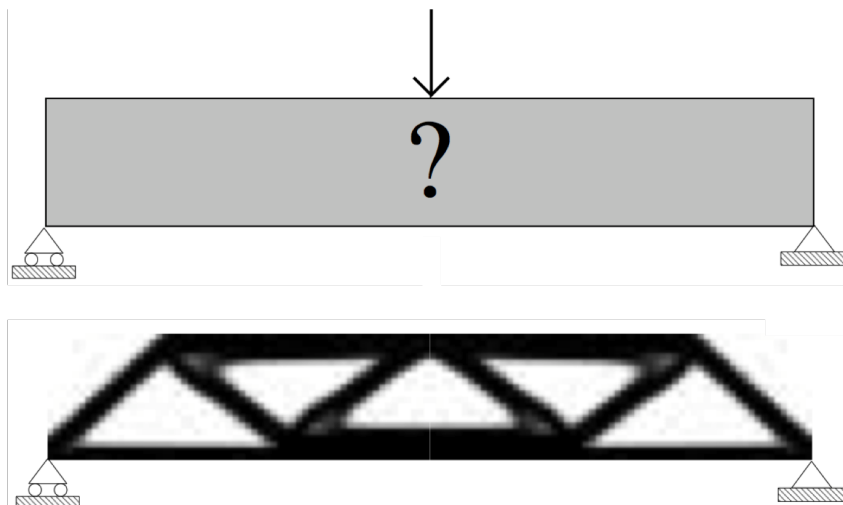


Figure 2.5: The benchmark optimal design problem. From [108].

one has to either relax the problem by homogenization [109, 110, 111] or regularize it by the introduction of perimeter constraints [112, 113]. The general framework for optimal design can be sketched as follows:

Reference domain:	$\Omega \subset \mathbb{R}^N$
Volume fractions:	$0 \leq \theta \leq 1$
Admissible designs:	$D \subset \Omega$
	$ D \leq \theta \Omega $
Optimal design problem:	$\inf_{D \text{ admissible}} F(D)$
Optimize iteratively:	$\partial_D F(D)$.

Typically, the admissible designs described here form a discrete subset of the design domain that we optimize over. The existence and nature of minimizers of our objective $F(D)$ are not insured, and sequential designs progressing to these infimums often are outside of the relevant functional class. Additionally, iterative optimization typically requires a notion of sensitivity with respect to designs, which become very cumbersome in the "discrete" material setting. Relaxation allows for intermediate densities, or areas of microstructure, to be considered through the optimization. Objective functions can be an prescribed quantity using the field solved for in the constraining PDE; mechanical compliance, total stored energy, conductivity, and resonant frequency are just a small sample of the problems that have been explored in this framework. Because of the complex structure of optional design problems, they have a background rich in theory and analysis. Since the optimization is coupled to solving a physical problem, the existence of minimizing solutions in the design space and solutions to the physical problem are coupled. Studies seek to

find a relation between these two as well as general existence theories, typically in the variational setting [97]. The general mathematical analysis of these problems is well established by the classic series from Kohn and Strang [111, 114, 115], and guides the analysis presented in Ch. 6.

Optimization methods and applications

Numerical methods in design optimization can usually be broken down into two steps: first is solving the underlying physical problem using finite element or finite difference methods for a chosen initial design, secondly, the design is updated using optimization method utilizing a notion of sensitivity of the objective function with respect to the design field. Relaxation is commonly a key aspect in this sensitivity analysis, and accordingly, the physical models have to be formulated to accommodate intermediate densities. This relaxation of design space requires interpolating material behavior between the phases in question. For example, if we consider a topology optimization problem in linear elasticity, the elastic modulus of the material will be interpolated as follows:

$$K(x) = K_1\rho(x) + K_2(1 - \rho(x)),$$

where K_i represents the modulus in the i -phase, and ρ is our design field, or density. Relaxing the problem in the optimization setting usually results in large areas of intermediate, or composite, densities throughout the design domain. To enforce manufacturability, or a minimum length scale for features, penalties are usually enforced on these intermediate densities. Classically, topology optimization uses the Solid Isotropic Material with Penalization (SIMP) approach, [108, 116] where these intermediate densities are limited through the material response:

$$\tilde{K}(x) = K_1\rho^p(x) + K_2(1 - \rho^p(x)),$$

where p is typically chosen based on the problem and typically takes values, $3 < p < 10$. The effective behavior is \tilde{K} is made unfavorable through the optimization and thus, near discrete results are obtained. Different "phase functions" can be used to describe how material parameters vary with the design field ρ . Additional, heuristic, post-processing, filtering, and adjustments are made numerically in these methods with the assumption that optimality is not severely impacted. The level set approach is an alternative to relaxation, where material interfaces are tracked implicitly through the computation as zero contours of a level set function and thus lends itself more to shape optimization rather than topology optimization.

Methods rely on different notions of sensitivity, commonly based on the Hamilton-Jacobi equation to alter the material boundaries [117, 118, 119]. Although adaptive numerical meshing is not always required, the method pays the cost of being very dependent of the initial guess of the structure, and re-initialization does not always lead to a solution. The level-set method has been found in other research areas including fluid mechanics, where fluid-solid interfaces are important, and image analysis for tracking boundaries.

In applying a regularization, specifically "perimeter-controlled" optimization, adding a penalty of the surface area term to the objective functional solves the issues of not obtaining admissible designs. By limiting the perimeter of the resulting designs, sequences of solutions with rapid oscillations, or areas of fine-scale mixtures, are penalized, and the resulting problem becomes well posed [112]:

$$\inf_{D \text{ admissible}} F(D) + \lambda \mathcal{H}^{N-1}(\partial D),$$

where \mathcal{H}^{N-1} is the Hausdorff measure, the length (are area) of ∂D . However, the theory lacks a viable numerical approach, and so it must be coupled with relaxation. The approach that we take in our optimization (Ch. 6) grows from relaxation to applying a phase-field model where intermediate densities and interfaces are numerically penalized. We implement an energy form seen from work done in surface dynamics modeling in phase transitions by Cahn-Hilliard [120] and Allen-Cahn [121]. Phase-field methods have been numerically implemented in dendrite growth [122], crack propagation [123], and grain evolution [124] and are well suited to the typical frameworks in optimal design. This penalty relies on an artificial two-well potential favoring each phase, and an interfacial term relying on the gradient of the density ρ ,

$$\int_{\Omega} W(\rho) + |\nabla \rho|^2 dx,$$

where $W(\rho) \propto \rho^2(1 - \rho)^2$. This method of penalization is an alternative to the heuristic filtering techniques typically found in numerical topology optimization as well as the assumed microstructural design found in homogenization techniques. There is an associated length scale arising from the phase-field penalty that is numerically controlled, and it has been found that in the limit, this reduces to the same perimeter penalty. This affords minimal numerical filtering, relatively unaltered optimization methods, mesh independent results, and allows for complete generality in topology optimization without dependence on initial guesses. It has

proved to be effective in various multi-physics settings, and also allows for rigorous mathematical analysis of the resulting problems [113, 125, 126, 127].

Applying topology optimization techniques to the transport and reaction that occurs in thermochemical conversion devices is a new endeavor, but similar applications have been examined previously. In the mechanics problems commonly examined, loads on a structure are applied externally, and are independent to the design field and its fluctuations. However, when multi-physics problems are examined where the "loads" placed on the system depend on the design field (i.e. a pressure force, gravity, or a chemical source), a separate group of literature exists to address these "design-dependent loads" [113, 128]. The presence of two species lends a vectorial character to our problem, and the presence of the surface sources makes the problem at hand different from those in the literature. The diffusive transport considered bears the most resemblance to problems of heat conduction, where the task of optimizing a thermal lens by designing a conducting body with the objective of maximizing the heat flux through a sink in the domain [129, 130, 131]. This can be extended to include convective behavior with similar results displaying a hierarchical, branched arrangement of the conducting material [132]. The general topology optimization approach can be extended to any multi-physics situation (e.g. MEMS), where a consistent system of PDE's can be used as constraints on the optimization [108]. Including fluid flow and reaction has been investigated as well, albeit in slightly different settings than we propose here. Stokes flow has been investigated with the goal of minimizing the dissipated power in a fluid flowing through a structure [133], and chemical reaction in single-phase flow was investigated for optimizing reactive fluid transport in microfluidic (bio-)reactors [134, 135, 136]. Osanov and Guest have recently written an inspiring review presenting the application of topology optimization for architected materials, where a variety of length scales are involved in creating materials with unique, tailored, properties [137]. We apply topology optimization techniques in combination with the phase-field method for designing pore structure in an idealized thermochemical reactor setting in Ch. 6.

CONTINUUM TRANSPORT IN MIXED CONDUCTORS

We derive the transport equations for electrons and oxygen vacancies through ceria under an externally-applied electric potential in an oxygen environment using various balance laws and constitutive equations. From this, we obtain various thermodynamic potentials that take into consideration the thermal, chemical, and mechanical state of the material. Accordingly, we obtain a system of partial differential equations describing ambipolar diffusion (or the diffusion-drift equation) from the continuum mechanics framework. As a confirmation, the transport equations obtained are consistent with those used in experimental literature under certain specific constitutive relations.

3.1 Formulation

We consider the transport of charged vacancies and the coupled electron movement without considering possible polarization or inter-band electron transfer [52, 34, 35]. Additionally, we ignore phase transitions that could occur as a function of the non-stoichiometry. Under reducing atmospheres (obtained here by mixing H_2 and H_2O), cerium undergoes partial reduction from the 4+ to 3+ oxidation state, giving rise to mixed ionic and electronic conduction. On the surface of the mixed conductor, the formation of localized electrons and intrinsic oxygen vacancies can

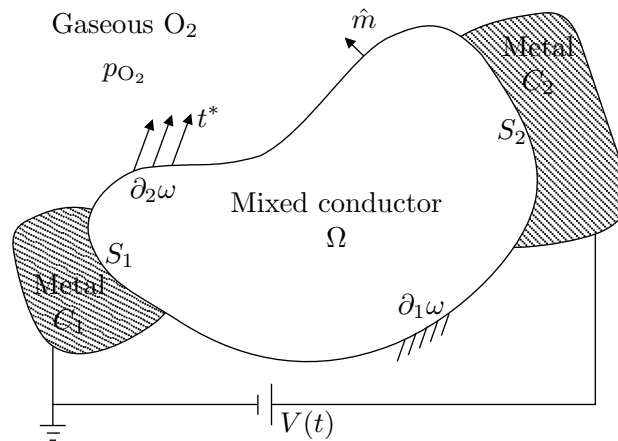
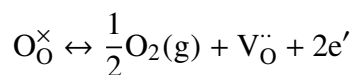


Figure 3.1: Schematic arrangement of the mixed conductor.

be expressed as



Consider a sample of ceria (or similar oxide-conducting ceramic) occupying a region Ω with boundary $\partial\Omega$ and outward normal \hat{m} . The metal electrodes it is connected to are denoted by C_1, C_2 with boundaries $\partial C_1, \partial C_2$ respectively. Let $\partial\Omega \cap \partial C_1 = S_1$ and $\partial\Omega \cap \partial C_2 = S_2$. We complete the circuit with a varying potential across the system, $V(t)$, as well as expose the system to a partial pressure of oxygen, p_{O_2} . Additionally, we prescribe displacements over $\partial_1\omega$ boundary tractions t^* over a portion of the boundary $\partial_2\omega$. Now, noting the species in question, we denote:

Species	Conc.	Charge	Flux
O vacancy	$c_{ion} = c_i$	$z_i = +2$	J_i
Electron	$c_{eon} = e_e$	$z_e = -1$	J_e
Neutral oxygen	c_O	$z_O = 0$	J_O

We assume that the displacements, u , and displacement gradients are small. So, the strain $\varepsilon = \frac{1}{2}(\nabla u + \nabla u^T)$, and we don't distinguish between reference and current configuration in writing the balance laws.

3.2 Balance laws

Conservation of mass

We start with the general formulation for a well-behaved subdomain $D \subset \Omega$:

$$\begin{aligned} \frac{\partial}{\partial t} \int_D c_i dx &= - \int_{\partial D} J_i \cdot \hat{n} ds \\ \frac{\partial}{\partial t} \int_D c_e dx &= - \int_{\partial D} J_e \cdot \hat{n} ds. \end{aligned}$$

Localizing these equations yields the desired conservation equations

$$\begin{aligned} \dot{c}_i &= -\nabla \cdot J_i \\ \dot{c}_e &= -\nabla \cdot J_e. \end{aligned}$$

Here, the overdot represents a time derivative.

Electrostatics

In the absence of polarization, the electrostatic potential ϕ solves Maxwell's equation:

$$\begin{cases} \nabla \cdot (-\epsilon_0 \nabla \phi) = \rho \chi_\Omega \text{ in } \mathbb{R}^3 \setminus (C_1 \cup C_2) \\ \phi = 0 \text{ in } C_1 \\ \phi = V \text{ in } C_2 \end{cases}$$

with charge density ρ and χ_Ω as the indicator function for our mixed-conductor domain:

$$\chi_\Omega(x) = \begin{cases} 1, & \text{if } x \in \Omega \\ 0, & \text{otherwise.} \end{cases}$$

The charge density can be represented by a combination of the electronic and ionic charges:

$$\rho = e(z_i c_i + z_e c_e),$$

where e is the magnitude of the charge of an electron.

Conservation of momentum

We use the standard balance laws from continuum mechanics. Using the Cauchy stress tensor, σ , we denote the conservation of linear momentum:

$$\nabla \cdot \sigma = 0.$$

The conservation of angular momentum is simply written as the symmetry constraint

$$\sigma^T = \sigma.$$

Further,

$$t^* = \sigma \hat{m} \text{ on } \partial_2 \omega.$$

Conservation of energy

We write the first law of thermodynamics, $dU = \bar{d}Q - \bar{d}\tilde{W}$, as follows:

$$\begin{aligned} \frac{d}{dt} \left(\int_D U + \epsilon_0 |\nabla \phi|^2 dx \right) &= - \int_{\partial\Omega} q \cdot \hat{m} dA + \int_\Omega r dx \\ &\quad - \int_{\partial\Omega} (\tilde{\mu}_e J_e \cdot \hat{m} - \tilde{\mu}_i J_i \cdot \hat{m}) dA \\ &\quad + \int_{\partial D} \phi (\epsilon \nabla \dot{\phi} \cdot \hat{m}) dA + \int_{\partial\Omega} \sigma \hat{m} \cdot \dot{u} dA. \end{aligned}$$

Here, U denotes the internal energy density, q the heat flux, r the radiative heat transfer, $\tilde{\mu}$ refers to the typical electrochemical potential of the species in question, and σ_q is the surface charge density:

$$\sigma_q = \llbracket -\epsilon_0 \nabla \phi \rrbracket \cdot \hat{m} \text{ on } \partial(C_1 \cup C_2),$$

Here, $\llbracket \cdot \rrbracket$ denotes the jump across an interface: $\llbracket \xi \rrbracket = \xi^+ - \xi^-$, with ξ being a variable denoted in both domains; \hat{m} is the unit norm of the interface, pointing to our conductor, D^+ , from D^- , the rest of \mathbb{R}^3 . Notice the surface charge density can be simplified in terms of the potential outside of the conductors:

$$\begin{aligned} \sigma_q &= \llbracket -\epsilon_0 \nabla \phi \rrbracket \cdot \hat{m} \\ &= -\epsilon_0 (\nabla \phi^+ - \nabla \phi^-) \cdot \hat{m} \\ &= \epsilon_0 \nabla \phi \cdot \hat{m}. \end{aligned}$$

On the left hand side, terms denote the rate of change of total energy, taking into account the internal energy stored in our body as well as the energy from the electrostatic potential in space. We also consider the contribution due to the external oxygen environment, measuring the capability for the fixed potential to do work on the body, which is dependent on the potential and the maximum amount of exchange that can occur, $\int c_i dx$. On the right hand side, contributions due to the chemical energy being transferred via the flux of species, the heat flux (q), and a body source r , and finally the mechanical work done on the system. In this formulation, we have neglected the surface free energy as well as blackbody-radiation and separate contributions to the entropy (e.g. vibration and configurational).

Multiplying Maxwell's law by the field ϕ , and integrating over our subdomain D yields

$$\int_D \epsilon_0 |\nabla \phi|^2 dx - \epsilon_0 \int_{\partial D} \phi (\nabla \phi \cdot \hat{n}) dA = \int_D \rho \phi dx.$$

Taking the time derivative yields:

$$2\epsilon_0 \int_D \nabla \dot{\phi} \cdot \nabla \phi dx = \frac{d}{dt} \int_{\partial D} \epsilon_0 \phi (\nabla \phi \cdot \hat{n}) dA + \int_D (\dot{\rho} \phi + \rho \dot{\phi}) dx.$$

Similarly, by multiplying Maxwell's law by $\dot{\phi}$ and integrating we obtain:

$$\epsilon_0 \int_D \nabla \dot{\phi} \cdot \nabla \phi dx - \epsilon_0 \int_{\partial D} \dot{\phi} \nabla \phi \cdot \hat{n} dA = \int_D \rho \dot{\phi} dx.$$

Subtracting the second relation from the first yields:

$$\frac{d}{dt} \int_D \frac{1}{2} \epsilon_0 |\nabla \phi|^2 dx = \int_{\partial D} \dot{\phi} (\epsilon_0 \nabla \phi \cdot \hat{n}) dA + \int_D \rho \dot{\phi} dx.$$

Using this, the first law becomes:

$$\int_D \dot{U} + \dot{\rho}\phi \, dx = \int_D (-\nabla \cdot q + r - \nabla (\tilde{\mu}_i J_i + \tilde{\mu}_e J_e) + \nabla \cdot (\sigma \dot{u})) \, dx.$$

Notice how we no longer have contributions from the boundary of D . Accordingly, we can localize the first law of thermodynamics to obtain:

$$\dot{U} + \dot{\rho}\phi = -\nabla \cdot q + r - \nabla (\tilde{\mu}_i J_i + \tilde{\mu}_e J_e) + \sigma \cdot \nabla \dot{u}, \quad (3.1)$$

where we have enforced mechanical equilibrium $\nabla \cdot \sigma = 0$.

3.3 Constitutive equations

Entropy inequality

We now turn to the second law:

$$\frac{d}{dt} \int_D \eta \, dx \geq - \int_{\partial D} \frac{q}{\theta} \cdot \hat{n} \, dA + \int_D \frac{r}{\theta} \, dx.$$

where η represents the specific entropy density, and θ is being used a thermodynamic temperature scale. The left hand side denotes the entropy production. The contribution involving r represents any body sources, and q measures any boundary fluxes. Localizing yields,

$$\theta \dot{\eta} \geq -\nabla \cdot q + \frac{1}{\theta} q \cdot \nabla \theta + r.$$

Applying the first law, 3.1, yields

$$\theta \dot{\eta} \geq \dot{U} + \dot{\rho}\phi + \nabla (\tilde{\mu}_i J_i + \tilde{\mu}_e J_e) - \sigma \cdot \nabla \dot{u} + \frac{1}{\theta} q \cdot \nabla \theta.$$

Derivation of driving forces

We introduce the Helmholtz free energy density, $W = U - \theta\eta$, and apply the localized mass conservation equations to obtain

$$0 \geq \dot{W} + \dot{\theta}\eta + \dot{\rho}\phi - \tilde{\mu}_i \dot{c}_i - \tilde{\mu}_e \dot{c}_e + \nabla \tilde{\mu}_i \cdot J_i + \nabla \tilde{\mu}_e \cdot J_e - \sigma \cdot \dot{\varepsilon} + \frac{1}{\theta} q \cdot \nabla \theta.$$

At this point, there is no assumption made on the form of our free energy, but rather its dependence on the desired variables:

$$W = W(c_i, c_e, \theta, \varepsilon),$$

so that in computing \dot{W} , we are left with

$$\dot{W} = \frac{\partial W}{\partial c_i} \dot{c}_i + \frac{\partial W}{\partial c_e} \dot{c}_e + \frac{\partial W}{\partial \theta} \dot{\theta} + \frac{\partial W}{\partial \varepsilon} \dot{\varepsilon}.$$

Therefore, we obtain an expression resembling the local dissipation:

$$\begin{aligned}
& - \left(\frac{\partial W}{\partial c_i} + z_i e \phi - \tilde{\mu}_i \right) \dot{c}_i - \left(\frac{\partial W}{\partial c_e} + z_e e \phi - \tilde{\mu}_e \right) \dot{c}_e \\
& - \left(\frac{\partial W}{\partial \theta} + \eta \right) \dot{\theta} - \left(\frac{\partial W}{\partial \varepsilon} - \sigma \right) \dot{\varepsilon} \\
& - \nabla \tilde{\mu}_i \cdot J_i - \nabla \tilde{\mu}_e \cdot J_e - \frac{q \cdot \nabla \theta}{\theta} \geq 0.
\end{aligned}$$

Notice that each of these terms is a product of a conjugate pair: generalized velocity (time rate of change of some quantity or flux of some quantity) multiplied by a generalized force (a quantity that depends on the state and not the rate of change of the state). Following [59], we consider various processes that are in the same state at an instant but have varying "velocities". Insisting that the second law holds for these processes implies that:

$$\begin{aligned}
\tilde{\mu}_i &= \frac{\partial W}{\partial c_i} + z_i e \phi \\
\tilde{\mu}_e &= \frac{\partial W}{\partial c_e} + z_e e \phi \\
\eta &= - \frac{\partial W}{\partial \theta} \\
\sigma &= \frac{\partial W}{\partial \varepsilon}.
\end{aligned}$$

It follows that the non-conjugate pairs must be negative:

$$\begin{aligned}
\nabla \tilde{\mu}_i \cdot J_i &\leq 0 \\
\nabla \tilde{\mu}_e \cdot J_e &\leq 0 \\
q \cdot \nabla \theta &\leq 0.
\end{aligned}$$

Note that the potentials $\tilde{\mu}_i$ and $\tilde{\mu}_e$ we have derived are the typical electrochemical potentials.

Transport equations

In order to satisfy the negative quantities, we heuristically write that the flux is the product of the particle concentration per volume, the particles mobility, and the mean force per particle that we denote as the gradient of the electro-chemical potential gradients,

$$\begin{aligned}
J_i &= -K_i c_i \nabla \tilde{\mu}_i, \\
J_e &= -K_e c_e \nabla \tilde{\mu}_e,
\end{aligned}$$

with positive definite symmetric proportionality tensors K_i and K_e . For the temperature behavior, we meet the requirements of the entropy inequality by assuming Newton's law of cooling:

$$q = -\kappa \nabla \theta.$$

We assume there is no flux of electrons through the free surface of the sample, i.e. $J_e = 0$ on $\partial\Omega \setminus (S_1 \cup S_2)$, and that there is no flux of oxygen vacancies through the surfaces shared with the conductors, i.e. $J_i = 0$ on $S_1 \cup S_2$. To consider the influence of the oxygen environment, we enforce the Butler-Volmer[38] linear exchange boundary condition for vacancies on the rest of the boundary, dependent on an externally applied partial pressure of oxygen. For the flux of electrons through the boundaries shared with the conductors, we use boundary conditions used in the semiconductor community [138] dependent on the work function $\Phi_{1,2}$ and metal potential. Compiling these yields the final equations; starting with the electrostatic potential:

$$\begin{aligned} \nabla \cdot (-\varepsilon_0 \nabla \phi) &= \rho \chi_\Omega \text{ in } \mathbb{R}^3 \setminus (C_1 \cup C_2) \\ \phi &= 0 \text{ in } C_1 \\ \phi &= V \text{ in } C_2 \\ \phi &\rightarrow 0 \text{ as } |x| \rightarrow \text{inf}. \end{aligned}$$

The electron and vacancy transport is determined via:

$$\begin{aligned} \dot{c}_i &= \nabla \cdot \left(K_i c_i \nabla \left(\frac{\partial W_i}{\partial c_i} + z_i e \phi \right) \right) = \text{in } \Omega \\ \dot{c}_e &= \nabla \cdot \left(K_e c_e \nabla \left(\frac{\partial W_e}{\partial n} + z_e e \phi \right) \right) = \text{in } \Omega, \end{aligned}$$

with the corresponding boundary conditions

$$\begin{aligned} J_e \cdot \hat{m} &= k_4 (e^{\beta(\mu_e + \Phi_1)} - 1) \text{ on } S_1 \\ J_e \cdot \hat{m} &= k_5 (e^{\beta(\mu_e + \Phi_2 + eV)} - 1) \text{ on } S_2 \\ J_e \cdot \hat{m} &= 0 \text{ on } \partial\Omega \setminus (S_1 \cup S_2) \\ J_i \cdot \hat{m} &= k(\mu_i + \mu_{O_2}) \text{ on } \partial\Omega \setminus (S_1 \cup S_2) \\ J_i \cdot \hat{m} &= 0 \text{ on } S_1 \cup S_2. \end{aligned}$$

For the aforementioned boundary condition on the flux of vacancies, we use the following rationale. We assume that the normal flux of vacancies through the open surface is dependent on the chemical potential of neutral oxygen in the matrix, μ_O , and that at equilibrium this potential must match that of the externally prescribed partial pressure of oxygen. Thus, linearizing about this equality we write:

$$J_O \cdot \hat{m} = k(\mu_O - \mu_{O_2}).$$

However, from the conservation of oxygen in the lattice,

$$\begin{aligned} dc_i + dc_O &= 0 \\ \Rightarrow \mu_O &= \frac{\partial W}{\partial c_O} = \frac{\partial W}{\partial c_i} \frac{\partial c_i}{\partial c_O} = -\mu_i, \end{aligned}$$

Thus, we obtain the desired boundary condition

$$J_i \cdot \hat{m} = -J_O \cdot \hat{m} = k(\mu_i + \mu_{O_2}).$$

Prescribing a form of the Helmholtz free energy

To examine the form of these thermodynamic potentials, and the multi-physics coupling, we assume the free energy density takes a prescribed additive form:

$$W(c_i, c_e, \varepsilon, \theta, x) = W_i(c_i) + W_e(c_e) + \frac{1}{2}(\varepsilon - \varepsilon^*(c_i, \theta)) \cdot \mathbb{C} \cdot (\varepsilon - \varepsilon^*(c_i, \theta)) - c_p \theta (\ln \theta + 1).$$

Here, $\varepsilon^*(c_i, \theta)$ describes the stress-free strain resulting from thermal and chemical expansion of the material. This implies that:

$$\tilde{\mu}_i = \frac{\partial W_i}{\partial c_i} + z_i e \phi - \varepsilon^* \cdot \mathbb{C} \cdot (\varepsilon - \varepsilon^*) \frac{\partial \varepsilon^*}{\partial c_i} \quad (3.2)$$

$$\tilde{\mu}_e = \frac{\partial W_e}{\partial c_e} + z_e e \phi \quad (3.3)$$

$$\eta = \varepsilon^* \cdot \mathbb{C} \cdot (\varepsilon - \varepsilon^*) \frac{\partial \varepsilon^*}{\partial \theta} + c_p (\ln \theta + 2) \quad (3.4)$$

$$\sigma = \mathbb{C} \cdot (\varepsilon - \varepsilon^*). \quad (3.5)$$

3.4 Consistency with previous literature

Single transport equation for neutral oxygen

To compare to models used in experimental work, e.g. [52, 34, 35], we derive an expression for the diffusivity " D_{chem} ," describing the mass transport of neutral oxygen as a function of the concentrations of electrons and vacancies in the bulk. Additionally, we re-derive the Nernst-Einstein relationship relating the conductivity

and diffusivity of a species. To start, we define new electrical-equivalents of the chemical and electro-chemical potential. We note that the charge flux due to a certain species is related to the mass flux via:

$$\begin{aligned} J_i^{\text{charge}} &= z_i e J_i^{\text{mass}} \\ &= -z_i e K_i c_i \nabla \mu_i - K_i c_i \nabla \phi. \end{aligned}$$

We now define

$$\begin{aligned} \mu_i^* &= \frac{\mu_i}{z_i e}, \\ \tilde{\mu}_i^* &= \mu_i^* + \phi, \end{aligned}$$

to represent the electrical equivalent of the chemical potential and the electro-chemical potential, respectively. Thus, the charge flux becomes:

$$\begin{aligned} J_i^{\text{charge}} &= -K_i c_i \nabla \mu_i^* - K_i c_i \nabla \phi \\ &= -K_i c_i \nabla \tilde{\mu}_i^* \\ &= -\sigma_i \nabla \tilde{\mu}_i^*. \end{aligned}$$

Here, we have defined our conductivity $\sigma_i = K_i c_i$ to match what is typically used with Ohm's law. In general, the conductivity of a charged species is the product of its charge, mobility, and concentration. Now, we can re-derive the Nernst-Einstein relation by noting that in the absence of a field, the charge flux can be written using Fick's first law:

$$J_i^{\text{charge}} = -z_i e D_i \nabla c_i,$$

where we have used the traditional definition of diffusivity D_i . Also, note that without a field, $\tilde{\mu}_i^* = \frac{\mu_i}{z_i e}$, and assuming ideal behavior, $\nabla \mu_i = k_B T / c_i \nabla c_i$, we can write the charge transport as

$$J_i^{\text{charge}} = -\frac{k_B T}{c_i z_i e} \sigma_i \nabla c_i.$$

To match the behavior described by Fick's law, we require:

$$D_i = \frac{k_B T}{c_i (z_i e)^2} \sigma_i,$$

which is our desired relationship.

Now, continuing towards D_{chem} , we impose inherent material behavior, noting that the vacancy and electron transport are coupled:

$$\begin{aligned} J_{\text{ion}}^{\text{charge}} + J_{\text{eon}}^{\text{charge}} &= 0 \\ \Rightarrow -K_i c_i \nabla \mu_i^* - K_i c_i \nabla \phi - K_e c_e \nabla \mu_e^* - K_e c_e \nabla \phi &= 0 \\ \nabla \phi &= \frac{-\sigma_i \nabla \mu_i^* - \sigma_e \nabla \mu_e^*}{\sigma_i + \sigma_e}. \end{aligned}$$

Using this in the expression for the charge flux due to vacancy movement yields,

$$\begin{aligned} J_i^{\text{charge}} &= -\sigma_i \nabla \mu_i^* - \sigma_i \left(\frac{-\sigma_i \nabla \mu_i^* - \sigma_e \nabla \mu_e^*}{\sigma_i + \sigma_e} \right) \\ &= \frac{-\sigma_i \sigma_e}{\sigma_i + \sigma_e} (\nabla \mu_i^* - \nabla \mu_e^*). \end{aligned}$$

At this point, we enforce local charge neutrality $\rho = z_i c_i + z_e c_e = 0$, and assume ideal behavior for the components

$$\nabla \mu_i^* = \frac{k_B T}{z_i e c_i} \nabla c_i.$$

From which it follows that we can relate the driving force of the two species through

$$\nabla \mu_e^* = -\frac{k_B T}{z_e e c_e} \frac{z_i}{z_e} \nabla c_i.$$

Equipped with this, and returning to the charge flux,

$$\begin{aligned} J_i^{\text{charge}} &= \frac{-\sigma_i \sigma_e}{\sigma_i + \sigma_e} \left(\frac{k_B T}{z_i e c_i} - \frac{k_B T}{z_e e c_e} \frac{z_i}{z_e} \right) \nabla c_i \\ &= \frac{-\sigma_i \sigma_e}{\sigma_i + \sigma_e} \left(\frac{k_B T z_i e}{e^2} \right) \left(\frac{1}{z_i^2 c_i} + \frac{1}{z_e^2 c_e} \right) \nabla c_i. \end{aligned}$$

Employing mass balance of the total oxygen in the domain (or, equivalently, the number of oxygen lattice sites) in order to relate the movement of neutral oxygen to the movement of vacancies,

$$dc_i + dc_{\text{O}} = 0,$$

or equivalently,

$$J_i^{\text{mass}} + J_{\text{O}}^{\text{mass}} = 0.$$

As a result, we find the desired transport equation describing the net movement of neutral oxygen through the domain,

$$\begin{aligned} J_{\text{O}}^{\text{mass}} &= \frac{-\sigma_i \sigma_e}{\sigma_i + \sigma_e} \left(\frac{k_B T}{e^2} \right) \left(\frac{1}{z_i^2 c_i} + \frac{1}{z_e^2 c_e} \right) \nabla c_{\text{O}} \\ &:= -D_{\text{chem}} \nabla c_{\text{O}}. \end{aligned}$$

However, without ideal behavior, using the fact that the movement of neutral oxygen requires the simultaneous movement of vacancies and electrons in ceria, we can write the effective diffusivity as:

$$D_{\text{chem}} = -\frac{\sigma_i \sigma_e}{4e^2(\sigma_i + \sigma_e)} \frac{\partial \mu_{\text{O}}}{\partial c_{\text{O}}},$$

where we have applied the charges of the species in question.

Experimental findings

Experimental results consist of data recording the thermodynamic behavior, equilibrium concentration of vacancies under various oxygen environments and temperatures, as well as the kinetic behavior: the conductivities (σ_e and σ_i), and surface reaction constant. The equilibrium data for non-stoichiometry is performed using thermogravimetric analysis (TGA), which consists of fixing the oxygen environment and temperature and yields data seen in Fig. 4.2. Through some technical assumptions, this data yields the thermodynamic behavior of the material. Additionally, we can use it in-part to determine the form of our free energy. Primarily, from the requirement for equilibrium, we can write the partial Gibb's energy as:

$$\Delta \bar{G}_{\text{O}} = \mu_{\text{O}} - \frac{1}{2} \mu_{\text{O}_2}^* = \frac{1}{2} RT \ln P_{\text{O}_2}.$$

Thus, we can convert this to

$$\ln P_{\text{O}_2} = 2\Delta \bar{H}_{\text{O}}/RT - 2\Delta \bar{S}_{\text{O}}/R.$$

So, one can obtain $\Delta \bar{H}_{\text{O}}$ and $\Delta \bar{S}_{\text{O}}$ from the slope/intercept of the $\ln P_{\text{O}_2}$ vs. $1/T$ plot.

It is possible to use this data to find the contribution of the vacancy concentration of the form of the free energy we prescribed earlier, W . In the absence of an electric potential (i.e. setting $\phi = 0$), at equilibrium we know that the chemical potential of the neutral oxygen in the lattice matches that of the gaseous oxygen in the pores:

$$\begin{aligned} \frac{1}{2} \mu_{\text{O}_2}(c_i, \theta) &= \mu_{\text{O}}(c_i, \theta) \\ &= \frac{\partial W}{\partial c_{\text{O}}}(c_i, \theta) \\ \Rightarrow W(c_i, c_e, p_{\text{O}_2}, \theta) &= \int_{c_i^*}^{c_i} \frac{1}{2} \mu_{\text{O}_2}(c) dc + \bar{W}(c_e, p_{\text{O}_2}, \theta). \end{aligned}$$

The total conductivity is well recorded as a function of the ionic and electronic conductivities:

$$\sigma_T = \sigma_{\text{ion}} + \sigma_{\text{eon}},$$

which are both dependent on temperature and p_{O_2} . Lai et al. [52] model this dependence by assuming the form $\sigma_T = \sigma_n^0 p_{O_2}^{-1/4} + \sigma_{ion} + \sigma_p^0 p_{O_2}^{1/4}$, where σ_p^0 and σ_n^0 are constants depending on the dopant concentration, the reduction equilibrium constant, the electronic defect equilibrium constant, and the respective electron defect mobilities: Under reducing conditions (low p_{O_2}), the total conductivity is

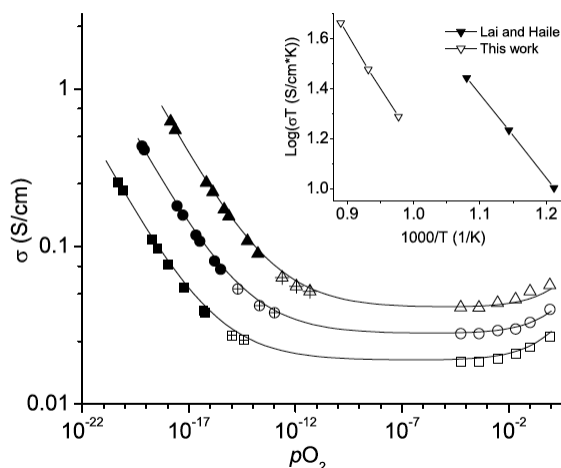


Figure 3.2: Total conductivity of samarium doped ceria, (SDC15), presented by [50]. Solid, cross-hair inscribed and open symbols respectively indicate data points obtained using H_2/H_2O , CO/CO_2 and dry O_2/Ar mixtures. Ionic conductivity shown in inset.

predominantly electronic, showing the expected n-type behavior with a -0.25 power law dependence on p_{O_2} . With increasing p_{O_2} , the conductivity remains a constant value, reflecting the occurrence of the electrolytic regime. At the highest values of p_{O_2} , the total conductivity increases, indicating the onset of p-type conductivity, which is more predominant in doped ceria materials [52].

The diffusivity also displays a similar trend as a function of oxygen environment: For undoped ceria, the electron and oxygen ion vacancy concentrations are related according to $2c_{ion} = c_{eon}$ under relevant oxygen partial pressures and temperatures. Accordingly, the ambipolar diffusion coefficient is independent of defect concentration under the ideal solution limit. At low oxygen non-stoichiometry, the chemical diffusion coefficient in SDC15 is substantially higher than it is in undoped ceria. The difference is about one order of magnitude at 923K and increases at lower temperature owing to the larger enthalpy of vacancy ion migration than electron migration [35]. The diffusivity of neutral oxygen in the bulk can be calculated to yield the dependence of the free energy on the defect concentration. Finally, the

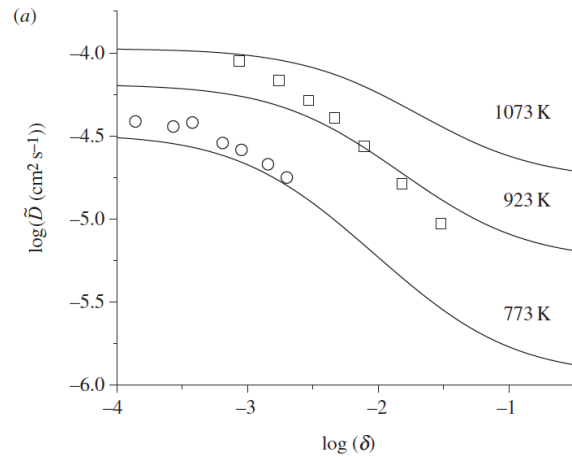


Figure 3.3: Neutral oxygen ambipolar diffusivity samarium doped ceria, (SDC15), as presented by [35].

surface reaction constant has been well documented over a range of temperature and p_{O_2} . Converting this data to involve the bulk concentrations in question (vacancies or neutral oxygen, and electrons) as well as the gaseous concentrations is an open question in MIEC modeling of ceria based metal oxides. More extensive explanations of the electrochemistry and transport in ceria is described well by [35, 52] and others, and a compilation of physical parameters over a variety of conditions can be found in [139].

Chapter 4

STRAINED OXIDES

Elastic strain engineering has been investigated with the intent of altering the energetic landscape for metals and oxides to improve their applications as catalysts, electrochemical energy conversion devices, separation membranes and memristors. A complete description of these applications can be found in the reviews by Yildiz and Bishop, [77, 140]. When variable valence oxides, such as ceria, become reduced, they undergo chemical expansion. Conversely, one would expect that if a such an oxide is exposed to a tensile stress, it should relax the stress by undergoing reduction. Induced stress could therefore be used as a means of lowering the temperature at which reduction occurs. We examine the strength of this effect, using experimental data describing the nonstoichiometry of ceria, $\text{CeO}_{2-\delta}$, [48].

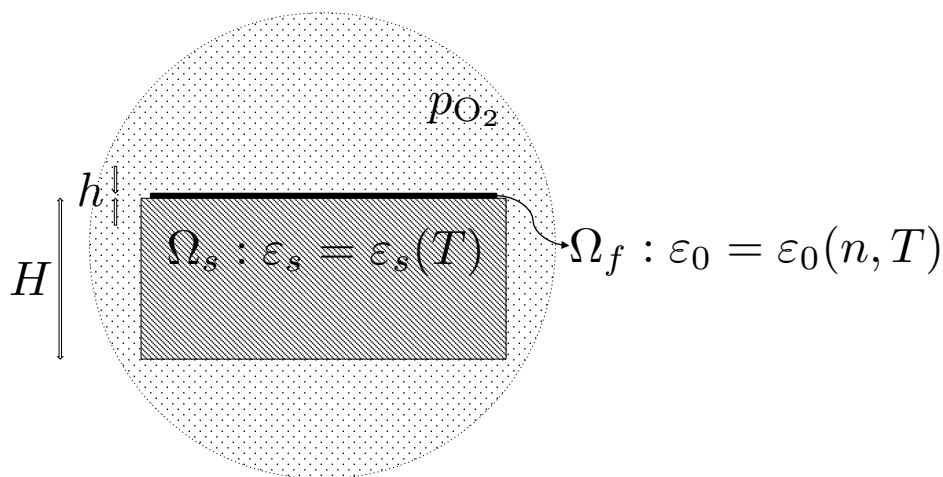


Figure 4.1: Idealized mixed conductor thin film problem, with thermal mismatch.

4.1 Formulation

For examining the possibility of strain-engineering of ceria to alter the thermodynamic (equilibrium) vacancy concentration, we neglect the electrostatic contributions and pose the problem as an ideal thin-film perfectly attached to an inert substrate. The idea is that upon inducing a strain in the oxide, the material relaxes the resulting stress via chemical expansion in addition to its thermal expansion. We formulate the mechanical problem as one resembling a bimetallic strip in two-dimensions. We consider the energy of the entire system in a continuum mechanics

setting, taking into account the thermomechanical contribution from the substrate, the chemo-thermo-mechanical energy of the film, and the effective contribution of the oxygen environment:

$$I(n, T, p_{\text{O}_2}) = \int_{\Omega_s} W_s(\varepsilon, T) dx + \int_{\Omega_f} W_f(\varepsilon, T, n) dx - \frac{1}{2} \mu_{\text{O}_2} \int_{\Omega_f} n dx, \quad (4.1)$$

where ε denotes strain, T the temperature, n the vacancy mole fraction of oxygen vacancies (note $n = \delta/3$ for ceria, CeO_2) and μ_{O_2} the chemical potential of atmospheric oxygen. The factor of $\frac{1}{2}$ reflects the fact that molecular oxygen yields two neutral oxygen atoms into the lattice. We assume that the energy densities of the substrate and film are of the form:

$$W_s(T, \varepsilon) = W_{0s}(T) + \frac{1}{2} (\varepsilon - \varepsilon_s(T)) : \mathbb{C}_s : (\varepsilon - \varepsilon_s(T)),$$

$$W_f(n, T, \varepsilon) = W_0(n, T) + \frac{1}{2} (\varepsilon - \varepsilon_0(n, T)I) : \mathbb{C} : (\varepsilon - \varepsilon_0(n, T)I),$$

where $\varepsilon_s(T)$ denotes the temperature-dependent, stress-free, strain of the substrate and $\varepsilon_f(n, T)$ denotes the composition and temperature-dependent stress-free strain of the film. We assume that $\varepsilon_f = \varepsilon_0 I$.

We use the notion of equilibrium to determine our desired relations between the strain of the film and the vacancy concentration. We assume that the film is extremely thin, and thus n and ε are uniform throughout the film. By taking the first variation with respect to the concentration, n , we find

$$\frac{\partial W_f}{\partial n} = \frac{1}{2} \mu_{\text{O}_2}, \quad (4.2)$$

$$\Rightarrow \frac{\partial W_0}{\partial n} - \frac{\partial \varepsilon_0}{\partial n} I : \mathbb{C} : (\varepsilon - \varepsilon_0(n, T)I) = \frac{1}{2} \mu_{\text{O}_2}, \quad (4.3)$$

$$\Rightarrow \frac{1}{2} \mu_{\text{O}_2} = \frac{\partial W_0}{\partial n} - \text{tr}(\sigma) \frac{\partial \varepsilon_0}{\partial n}. \quad (4.4)$$

We have used the typical definition of stress in our material, as was derived formally earlier. To find a relation between the vacancy fraction as a function of temperature when the material is strained at a fixed p_{O_2} , the mechano-chemical potential can be exploited in the following way. We fix the potential μ for oxygen via the external oxygen environment:

$$\mu_{\text{O}_2} = RT \ln p_{\text{O}_2}.$$

When the stress is zero, we obtain,

$$\frac{\partial W_0}{\partial n}(n, T) = \frac{1}{2} RT \ln p_{\text{O}_2}.$$

This relation between n and p_{O_2} has been measured using thermogravimetric analysis at various temperatures by Panlener [48] and reproduced in Fig. 4.2, (recall $\delta = 3n$).

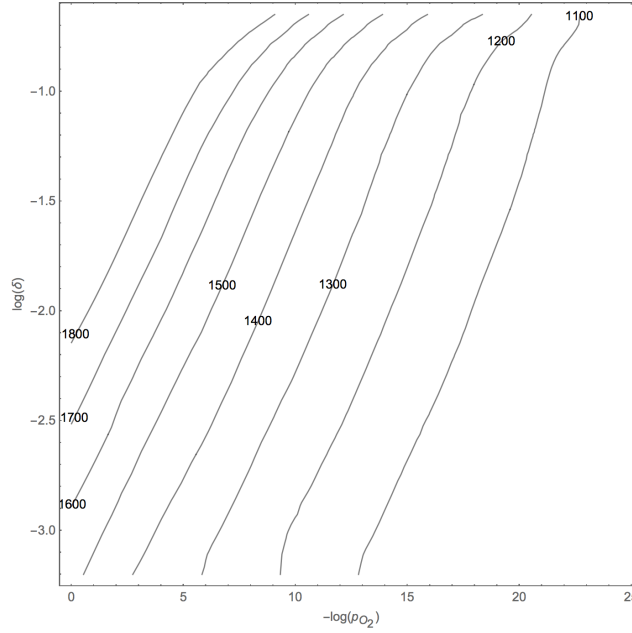


Figure 4.2: Oxygen non-stoichiometry, δ in $CeO_{2-\delta}$ measured in 100K intervals using thermogravimetry from [48].

We now turn to the mechanics problem of minimizing 4.1 with respect to the strain ε . Again, if the film is very thin compared to the substrate, the substrate dominates and we have

$$\varepsilon = \varepsilon_s(T).$$

Using and Hooke's law for plane stress, we find

$$\text{tr}(\sigma) = \frac{E}{1-\nu} (2\varepsilon_s(T) - \varepsilon_0(n, T)).$$

If we denote by T_{ref} and $p_{O_2,ref}$ the temperature and environment at which the stress-free substrate is bonded to the stress-free film (thereby creating a reference composition n_{ref}), we can linearize around these conditions:

$$\varepsilon_0(T, n) = \alpha_t (T - T_{ref}) + \alpha_c (n - n_{ref}),$$

where α_t is the coefficient of thermal expansion and α_c is the coefficient of chemical expansion. We use a similar form for the substrate's thermal strain and combining with the thermodynamic potential Eq. (4.2) yields:

$$\ln p_{O_2} = \frac{\partial W_0}{\partial n}(n, T) + \frac{2E\alpha_c}{RT(1-\nu)} \left((2\alpha_s - \alpha_t)(T - T_{ref}) + \frac{\alpha_c}{3}(\delta - \delta_{ref}) \right).$$

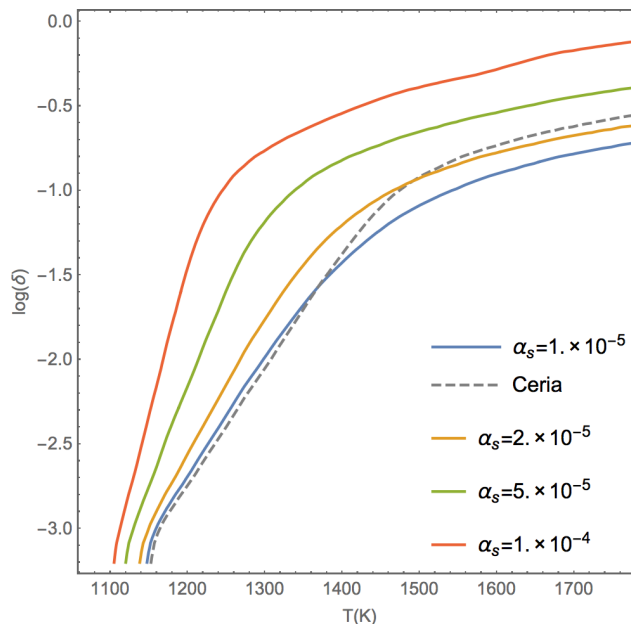


Figure 4.3: Equilibrium strain effect: $\log(\delta)$ vs. T at $p_{O_2} = 10^{-11}$ atm for various substrate thermal expansion coefficients.

Thus, upon fixing reference conditions ($T_{ref}, p_{O_2,ref}$) that determine a starting non-stoichiometry (δ_{ref}), we can implicitly plot our $\log(\delta)$ vs. T for various oxygen environments. Considering attachment at an elevated temperature in a oxygen environment akin to normal air, we examine the role the substrate has on the behavior as the expansion coefficient is altered. The parameters used are as follows: ¹

$$\begin{aligned}\alpha_T &= 10^{-5}[141, 139], \alpha_c = 3.3 \times 10^{-1}[41], \\ E &= 2.6 \times 10^8 \text{ kPa}[67], \nu = 0.3[139] \\ p_{O_2,ref} &= 0.21 \text{ atm}, T_{ref} = 1073 \text{ K} \rightarrow \delta_{ref} = 10^{-6.44}, \\ p_{O_2} &= 10^{-11} \text{ atm}.\end{aligned}$$

Under these conditions, we obtain Fig. 4.3. We examine the impact of the substrate in Fig. 4.4, picking a variety of thermal expansivities representing possible substrate candidates such as alumina or YSZ. If the substrate's thermal expansion matches

¹A range of physical parameters exist for undoped ceria, many of which are functions of temperature and oxygen concentration. The elastic modulus is known to vary with composition [67], and we use the uppermost value (at lowest nonstoichiometry). Thermal expansivity varies with temperature, and so a lower-limit is chosen for the temperature ranges considered. It also varies minimally with respect to amount of reduction [141]. Chemical expansivity (α_c) is typically defined with respect to nonstoichiometry δ , and thus our definition will be a factor of 3 larger. Marrocchelli et al. [41] compile values of chemical expansivity for undoped ceria: 0.11, 0.1102, and 0.15 w.r.t. δ . The value we use of 0.11 with respect to δ is found in other sources [76, 68, 140, 142].

that of ceria, the effect acts in reverse due to the chemical expansion of the film. The dependence on the reference configuration is investigated by changing reference temperature and reference pressure. For each prescribed environment, we set the reference non-stoichiometry in the film. Note that if we take a reference environment

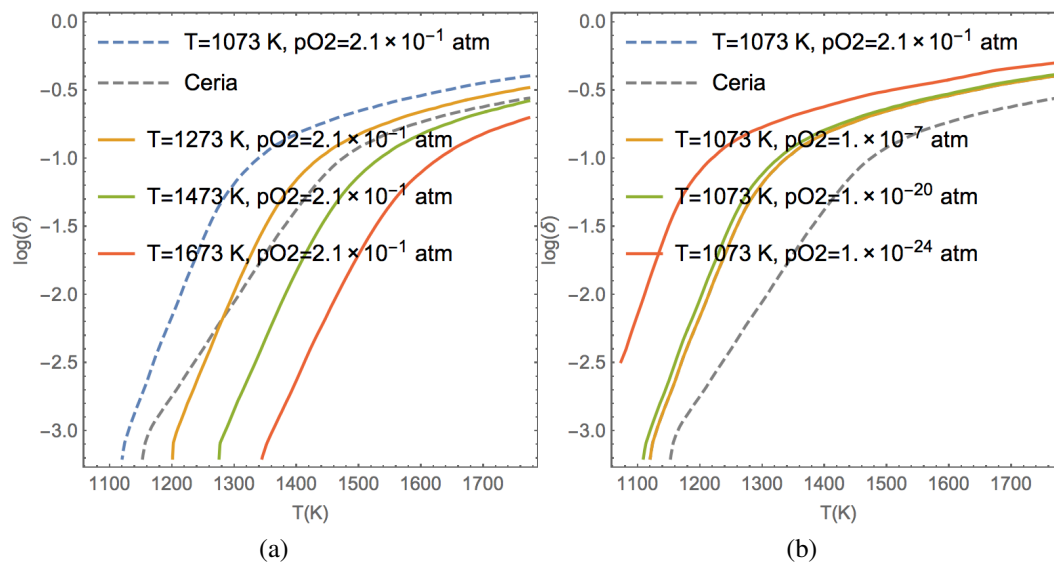


Figure 4.4: Equilibrium strain effect: $\log(\delta)$ vs. T at $p_{O_2} = 10^{-11}$ atm for various reference conditions: (a) varying T_{ref} ; (b) varying $p_{O_2,ref}$.

at the upper end of the temperature range, the effect is unfavorable since the substrate induces a compressive strain on the film, and a similar effect is observed by choosing a low-oxygen bonding environment. Examining the residual stress found in the sample leads to:

4.2 Conclusions

To recap, we have derived a generalized thermodynamic model describing the coupling the mechanical and chemical state of mixed conductors. This model could be extended to consider mass and charge transport in these materials, and could be applied to time-dependent studies of this coupling. In doing so, we were able to examine the effect of induced strain on a sample of ceria, and the subsequent change in non-stoichiometry. Alternate geometries could be considered and optimized for different applications. Instead of assuming an idealized thin-film problem, both the equilibrium relation derived here, or the time-dependent behavior described in the previous chapter, could be adapted to a finite element or finite difference scheme to examine the kinetic behavior in an arbitrary material configuration.

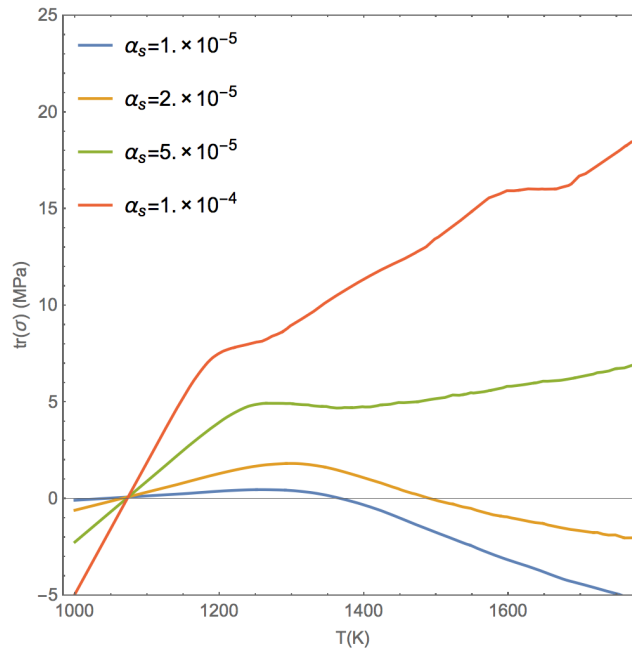


Figure 4.5: Residual stress in ceria film for different substrate thermal expansivities, using the same conditions and parameters as in Fig. 4.3.

There are obvious limitations to this model as one considers potential bonding issues and mismatch, as well as interaction between the film and substrate. The maximum strain observed by the sample is 7%, suggesting that a more rigorous, non-linear, mechanical model is necessary. The stress that the sample experiences could possibly extend beyond the elastic regime, requiring a comprehensive mechanical consideration, with a more accurate constitutive model for the film. The elastic modulus varies with the nonstoichiometry [67], but we only consider oxygen pressures such that it is approximately constant, and the softening of the material at higher nonstoichiometries only increases the desired effect. The chosen form of stress-free strain in the film linearly depends on vacancy concentration n . Other models have been investigated that suggest that the chemical expansion does not only depend on this value, but also the concentration of dopants, dimers, and trimers present in the material, eg. [68]. Finally, the additive form of the free energy could easily be expanded and made rigorous, and would be necessary if this theory is extended to other material classes, with more complicated physical considerations. The method of equilibrium alteration of mixed conductors is very generalized in this setting. Adaptation to battery components, fuel cells, and other multi-physics systems could be treated in a similar manner.

Chapter 5

HOMOGENIZATION THEORY

The mathematical homogenization of transport problems connects the design of microstructural features such as cell design in architected material or pore shape and volume in periodic composites with the macroscale behavior essential for application. When considering the optimal design of materials, homogenization theory affords two length-scales to design over allows for the development of complex, hierarchical structures to be developed. Through this chapter, we explore this interplay when considering the transport through porous mixed conductors. We start with a simpler problem of coupled diffusion as found in literature. The second portion consists of deriving homogenized transport of two chemical species determined by Stokes flow through the pore space, convective-diffusion through the gas phase, ionic diffusion through the bulk, and an interchange reaction at the interface. The primary aspect of these studies lies in determining the role the interface and reaction has on the overall behavior of the material. The results of this section guide choices in phase-field modeling of mixed conductors (as in Ch. 6), and the numerical calculation of effective behavior from reconstructed microstructures.

5.1 Reactive-Diffusion Formulation

We examine reactive diffusion through a porous material in which a gaseous species is converted to a second species through surface reaction occurring at the interface between the two phases. At the pore scale, we model the behavior of the gaseous species and the adsorbed species via coupled steady-state diffusion equations. In the subsequent section we also consider convection in the gaseous region. At the interface, we prescribe a Robin-type boundary condition, where the flux of each species is non-linear. We seek to find the macroscopic, or overall, transport equations at a scale much larger than the pores. This problem has also been studied by Auriault and Ene [103] and Peter and Böhm [143]. We include a discussion of this problem for completeness.

We consider a generic domain of porous material, Ω , with a periodic microstructure comprised of a characteristic unit cell, Y of dimension ε . In each of these unit cells, we consider the collection of solid inclusions, $S_i^\varepsilon = \varepsilon(a_i + S)$, and divide the domains and boundaries of interest as follows. In this framework, our pore-space

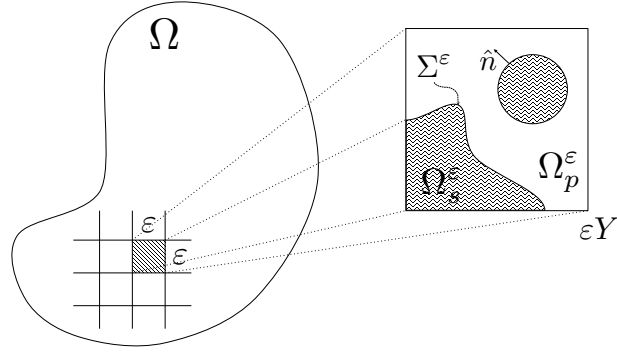


Figure 5.1: Generic problem setting.

and solid domain are defined by:

$$\begin{aligned}\Omega_p^\varepsilon &= \Omega \setminus \cup S_i^\varepsilon, \\ \Omega_s^\varepsilon &= \cup S_i^\varepsilon \cap \Omega,\end{aligned}$$

thus, our reactive boundary can be written as

$$\begin{aligned}\Sigma^\varepsilon &= \partial\Omega_p^\varepsilon \setminus \partial\Omega \\ &= \partial\Omega_s^\varepsilon \setminus \partial\Omega,\end{aligned}$$

or in the unit cell alone:

$$\begin{aligned}\Sigma &= \partial S \setminus \partial Y \\ &= \partial(Y \setminus S) \setminus \partial Y.\end{aligned}$$

The transport model describing the concentration of solid species u_1 and gaseous species u_2 and their interaction can be written:

$$\begin{aligned}-\nabla \cdot (k_1(y)\nabla u_1) &= 0 && \text{in } \Omega_p^\varepsilon, \\ -\nabla \cdot (k_2(y)\nabla u_2) &= 0 && \text{in } \Omega_s^\varepsilon, \\ -(k_1(y)\nabla u_1) \cdot \hat{n} &= -(k_2(y)\nabla u_2) \cdot \hat{n} = \varepsilon f(u_1, u_2) && \text{on } \Sigma^\varepsilon.\end{aligned}$$

Here, the diffusivities are set to vary with the pore length scale ($y = x/\varepsilon$), but could be taken to be constant in each of the domains considered. Additionally, our normal \hat{n} is defined as the outward normal to S on the reactive boundary Σ . We prescribe the scaling on the interface following the intuition presented by [103], in that we

wish to rationalize the model implemented in our optimization scheme in Ch. 6, where we have the effective body source/sink resulting at intermediate densities, corresponding to an homogenized interfacial reaction. Physically, this translates to the flux through the interface being weak compared to the diffusive transport of each species. Later, alternate scalings will be addressed.

The typical hypothesis for asymptotic behavior is that the resulting solutions u_1^ε and u_2^ε can be written as series expansions in terms of our characteristic length scale that are periodic over the unit cell:

$$u_i^\varepsilon(x, x/\varepsilon) = u_i^\varepsilon(x, y) = \sum_{j=0}^{\infty} \varepsilon^j u_i^j(x, y).$$

We perform a similar expansion of the reaction term along the interface as a series in ε :

$$f(u, v) = f(u^0, v^0) + \varepsilon f_u(u^0, v^0) u^1(x, y) + \varepsilon f_v(u^0, v^0) v^1(x, y) + \dots$$

Noting the chain rule,

$$\begin{aligned} \nabla(\cdot) &= (\nabla_x + \varepsilon^{-1} \nabla_y)(\cdot) \\ \Delta(\cdot) &= (\Delta_x + \varepsilon^{-1} \operatorname{div}_x \nabla_y + \varepsilon^{-1} \operatorname{div}_y \nabla_x + \varepsilon^{-2} \Delta_y)(\cdot), \end{aligned}$$

we start breaking our governing PDE system into subproblems corresponding to orders of ε . Starting with $\mathcal{O}(\varepsilon^{-2})$ terms from the PDE's and the boundary conditions of $\mathcal{O}(\varepsilon^{-1})$, we find

$$\begin{aligned} \nabla_y \cdot (k_1 \nabla_y u_1^0) &= 0 && \text{in } Y \setminus S, \\ \nabla_y \cdot (k_2 \nabla_y u_2^0) &= 0 && \text{in } S, \\ (k_1 \nabla_y u_1^0) \cdot \hat{n} &= (k_2 \nabla_y u_2^0) \cdot \hat{n} = 0 && \text{on } \Sigma. \end{aligned}$$

From this set of equations, we obtain the typical macroscopic solutions u_1^0 and u_2^0 . We examine their behavior by looking at the weak formulation of this system. Starting with the first equation and multiplying by a test function $u \in \mathcal{V}_1 = \{u \in H^1(Y) : (k_1 \nabla_y u) \cdot \hat{n} = 0 \text{ on } \Sigma, Y - \text{periodic}\}$, and integrate over the unit cell Y . Continuing the solution in question, u^0 , to the entirety of the cell by zero via the Hahn-Banach theorem, we write:

$$\int_{Y \setminus S} u (\nabla_y \cdot k_1 \nabla_y u_1^0) dy = 0.$$

Integrating by parts yields:

$$0 = - \int_{Y \setminus S} \nabla_y u \cdot k_1 \nabla_y u_1^0 dy + \int_{\partial(Y \setminus S)} u (k_1 \nabla_y u_1^0) \cdot \hat{m} dy,$$

where \hat{m} is the outward normal to $Y \setminus S$. Now, if we split the boundary integral based on our definitions:

$$0 = - \int_{Y \setminus S} \nabla_y u \cdot k_1 \nabla_y u_1^0 dy + \int_{\Sigma} u (k_1 \nabla_y u_1^0) \cdot \hat{m} dy + \int_{\partial Y} u (k_1 \nabla_y u_1^0) \cdot \hat{m} dy,$$

we can eliminate the integral over ∂Y due to the periodicity of our functions. Additionally, from the boundary conditions we can neglect the integral over Σ . Since $u_1^0 \in \mathcal{V}_1$,

$$0 = - \int_{Y \setminus S} \nabla_y u_1^0 \cdot k_1 \nabla_y u_1^0 dy.$$

Under the assumption that k_1 is positive semi-definite, our solution must achieve

$$\min_{u \in \mathcal{V}_1} \int_{Y \setminus S} \nabla_y u_1 \cdot k_1 \nabla_y u_1^0 dy.$$

Thus, we find our macroscopic relation stating that the homogenized solution is independent of fine scale structure:

$$u_1^0 = u_1^0(x).$$

Performing an identical procedure for the solid phase species with $v \in \mathcal{V}_2 = \{v \in H^1(Y) : (k_2 \nabla_y v) \cdot \hat{n} = 0 \text{ on } \Sigma, Y - \text{periodic}\}$:

$$\begin{aligned} 0 &= \int_S v (\nabla_y \cdot k_2 \nabla_y u_2^0) dy \\ &= - \int_S \nabla_y v \cdot k_2 \nabla_y u_2^0 dy + \int_{\partial S} v (k_2 \nabla_y u_2^0) \cdot \hat{n} dy \\ &= - \int_S \nabla_y v \cdot k_2 \nabla_y u_2^0 dy + \int_{\Sigma} v (k_2 \nabla_y u_2^0) \cdot \hat{n} dy + \int_{\partial Y} v (k_2 \nabla_y u_2^0) \cdot \hat{n} dy \\ &= - \int_S \nabla_y v \cdot k_2 \nabla_y u_2^0 dy. \end{aligned}$$

Again, we have imposed our obtained boundary conditions and the periodicity requirement on our solution u_2^0 . Via the same reasoning, we find the second macroscopic relation

$$u_2^0 = u_2^0(x).$$

Collecting the $\mathcal{O}(\varepsilon^{-1})$ terms from the governing PDE's, and the $\mathcal{O}(\varepsilon^0)$ terms from the boundary conditions yields the local problem:

$$\begin{aligned} \nabla_y \cdot \left(k_1 \left(\nabla_x u_1^0 + \nabla_y u_1^1 \right) \right) &= 0 & \text{in } Y \setminus S \\ \nabla_y \cdot \left(k_2 \left(\nabla_x u_2^0 + \nabla_y u_2^1 \right) \right) &= 0 & \text{in } S \\ k_1 \left(\nabla_x u_1^0 + \nabla_y u_1^1 \right) \cdot \hat{n} &= 0 & \text{on } \Sigma \\ k_2 \left(\nabla_x u_2^0 + \nabla_y u_2^1 \right) \cdot \hat{n} &= 0 & \text{on } \Sigma. \end{aligned}$$

We exploit the linearity of the system and the fact that u_1^0, u_2^0 are independent of y . Define U_1^i and U_2^i such that

$$\begin{aligned} -\nabla_y \cdot (k_1 \nabla_y U_1^i) &= \nabla_y \cdot (k_1 \hat{e}^i) & \text{in } Y \setminus S, \\ -\nabla_y \cdot (k_2 \nabla_y U_2^i) &= \nabla_y \cdot (k_2 \hat{e}^i) & \text{in } S, \\ (k_1 \nabla_y U_1^i) \cdot \hat{n} &= -k_1 \hat{e}^i & \text{on } \Sigma, \\ (k_2 \nabla_y U_2^i) \cdot \hat{n} &= -k_2 \hat{e}^i & \text{on } \Sigma \end{aligned}$$

and are Y -periodic. We write the solution to our local problem as the superposition:

$$\begin{aligned} u_1^1 &= \sum_{i=1}^n U_1^i (\nabla_x u_1^0 \cdot \hat{e}^i) + \bar{U}_1^1(x), \\ u_2^1 &= \sum_{i=1}^n U_2^i (\nabla_x u_2^0 \cdot \hat{e}^i) + \bar{U}_2^1(x), \end{aligned}$$

where $\bar{U}_1^1(x)$ and $\bar{U}_2^1(x)$ are arbitrary functions independent of y .

Equipped with our local solutions u_1^1 and u_2^1 , we move on to the transport equations at $\mathcal{O}(\varepsilon^0)$ and boundary conditions at $\mathcal{O}(\varepsilon^{-1})$ to obtain the compatibility conditions for our homogenization and the homogenized form of the transport equations. We find:

$$\begin{aligned} -\nabla_x \cdot (k_1 \nabla_x u_1^0) + \nabla_x \cdot (k_1 \nabla_y u_1^1) - \nabla_y \cdot \left(k_1 \left(\nabla_x u_1^1 + \nabla_y u_1^2 \right) \right) &= 0 & \text{in } Y \setminus S, \\ -\nabla_x \cdot \left(k_2 \left(\nabla_x u_2^0 + \nabla_y u_2^1 \right) \right) - \nabla_y \cdot \left(k_2 \left(\nabla_x u_2^1 + \nabla_y u_2^2 \right) \right) &= 0 & \text{in } S, \\ -k_1 \left(\nabla_x u_1^1 + \nabla_y u_1^2 \right) \cdot \hat{n} &= f(u_1^0, u_2^0) & \text{on } \Sigma, \\ -k_2 \left(\nabla_x u_2^1 + \nabla_y u_2^2 \right) \cdot \hat{n} &= f(u_1^0, u_2^0) & \text{on } \Sigma. \end{aligned}$$

The homogenized behavior is found by volume averaging over the unit cell Y . We again rely on the zero-continuation of each of our solutions to restrict the integration

to the separate domains in consideration. Rearranging the first terms and taking the derivatives with respect to x out of the integral:

$$\begin{aligned}\int_Y \nabla_x \cdot (k_1 \nabla_x u_1^0) dy &= \nabla_x \cdot \int_{Y \setminus S} k_1(y) dy \nabla_x u_1^0, \\ \int_Y \nabla_x \cdot (k_2 \nabla_x u_2^0) dy &= \nabla_x \cdot \int_S k_2(y) dy \nabla_x u_2^0.\end{aligned}$$

With the set of second terms, we apply the local solutions. Starting with the terms involving u_1 :

$$\begin{aligned}\int_Y \nabla_x \cdot (k_1 \nabla_y u_1^1) dy &= \nabla_x \cdot \int_{Y \setminus S} k_2 \nabla_y u_1^1 dy \\ &= \frac{\partial}{\partial x_i} \int_{Y \setminus S} k_{1,ij} \left(\frac{\partial U_1^k}{\partial y_j} \frac{\partial u_1^0}{\partial x_k} \right) dy,\end{aligned}$$

and similarly:

$$\begin{aligned}\int_Y \nabla_x \cdot (k_2 \nabla_y u_2^1) dy &= \nabla_x \cdot \int_S k_2 \nabla_y u_2^1 dy \\ &= \frac{\partial}{\partial x_i} \int_S k_{2,ij} \left(\frac{\partial U_2^k}{\partial y_j} \frac{\partial u_2^0}{\partial x_k} \right) dy.\end{aligned}$$

To integrate the last term over a period, Y , we apply the divergence theorem. From the continuation of our solutions, these integrals are reduced to $Y \setminus S$ or S . From periodicity, the contributions from the external boundary vanish leaving the contributions from the interface.

$$\begin{aligned}\int_Y \nabla_y \cdot (k_1 \nabla_x u_1^1 + k_1 \nabla_y u_1^2) dy &= \int_{Y \setminus S} \nabla_y \cdot (k_1 \nabla_x u_1^1 + k_1 \nabla_y u_1^2) dy \\ &= \int_{\Sigma} (k_1 \nabla_x u_1^1 + k_1 \nabla_y u_1^2) \cdot \hat{m} ds \\ &= \int_{\Sigma} f(u_1^0, u_2^0) ds.\end{aligned}$$

Rearranging yields a form similar to a diffusion equation with body reaction:

$$\begin{aligned}-\frac{\partial}{\partial x_i} k_1^{eff} \frac{\partial u_1^0}{\partial x_k} &= |\Sigma| f(u_1^0, u_2^0) \\ -\frac{\partial}{\partial x_i} k_2^{eff} \frac{\partial u_2^0}{\partial x_k} &= -|\Sigma| f(u_1^0, u_2^0).\end{aligned}$$

The effective transport and reaction behavior is calculated via

$$\begin{aligned} k_{1,ik}^{eff} &= \int_{Y \setminus S} k_{1,ij} \left(\delta_{jk} + \frac{\partial U_1^k}{\partial y_j} \right) dy, \\ k_{2,ik}^{eff} &= \int_{Y \setminus S} k_{2,ij} \left(\delta_{jk} + \frac{\partial U_2^k}{\partial y_j} \right) dy, \\ |\Sigma| &= \int_{\Sigma} ds, \end{aligned}$$

Note that the diffusivity of each species depends on the microstructure via the cell problem, but is not dependent on the interfacial exchange. Instead, we end up with a macroscopic body reaction source and sink for each species, taking the same form, but scaled with the measure in surface area in the unit cell. As the effective surface area increases, the reaction increases, but the conductivity would also be reflective of the design of the unit cell. Various forms of this reaction contribution are examined explicitly in the following section. Additionally, [103] presents a full analysis of laminar structures.

Summary of other interfacial scalings

We return to the original problem statement with the intention of examining alternate interfacial scalings, p :

$$\begin{aligned} -\nabla \cdot (k_1(y) \nabla u_1) &= 0 && \text{in } \Omega_p^\varepsilon, \\ -\nabla \cdot (k_2(y) \nabla u_2) &= 0 && \text{in } \Omega_s^\varepsilon, \\ -(k_1(y) \nabla u_1) \cdot \hat{n} &= -(k_2(y) \nabla u_2) \cdot \hat{n} = \varepsilon^p f(u_1, u_2) && \text{on } \Sigma^\varepsilon. \end{aligned}$$

The goal of this is to observe the extent to which the interface "strength" plays a role in the effective transport. The corresponding effective behavior and cell problems will be presented.

$\mathcal{O}(\varepsilon^p)$, $p \leq -2$

Using the definition presented here, a scaling of $\mathcal{O}(\varepsilon^p)$, $p = -2$ represents a classical conduction problem in a composite with barrier resistance. The effective behavior reduces to a single Poisson equation over Y , i.e. $u_1 = u_2$:

$$\begin{aligned} \frac{\partial}{\partial x_i} k_\alpha^{eff} \frac{\partial u^0}{\partial x_k} &= 0, \\ k_{\alpha,ik}^{eff} &= \int_Y k_{\alpha,ij} \left(\delta_{jk} + \frac{\partial U^k}{\partial y_j} \right) dy, \end{aligned}$$

where $\alpha = 1$ in $Y \setminus S$ and $\alpha = 2$ in S . U^k is the solution Y-periodic solution to the cell problem

$$\frac{\partial}{\partial y_i} \left[k_{\alpha,ij} \left(\delta_{jk} + \frac{\partial U^k}{\partial y_j} \right) \right] = 0 \text{ in } Y$$

$$\tilde{U}^k = 0$$

$$k_{1,ij} \left(\delta_{jk} + \frac{\partial U^k}{\partial y_j} \right) n_i = k_{2,ij} \left(\delta_{jk} + \frac{\partial U^k}{\partial y_j} \right) n_i \text{ on } \Sigma,$$

where $\tilde{\cdot} = \frac{1}{|Y|} \int_Y \cdot dx$ denotes a volume average. Situations where the interface exchange is $\mathcal{O}(\varepsilon^p)$, $p \leq -2$ follow the same derivation.

$\mathcal{O}(\varepsilon^{-1})$

As the exchange is increased w.r.t. to ε , we find that we again have a single resulting macroscopic field

$$u_1^0(x) = u_2^0(x) = u^0(x),$$

that yields a similar cell-problem. However, the cell solutions are not the same in each phase, namely they are linear functions with respect to the gradient of the macroscopic field

$$u_1^1 = \sum_{i=1}^n U_1^i (\nabla_x u_1^0 \cdot \hat{e}^i) + \bar{U}_1^1(x)$$

$$u_2^1 = \sum_{i=1}^n U_2^i (\nabla_x u_2^0 \cdot \hat{e}^i) + \bar{U}_2^1(x).$$

$\bar{U}^1(x)$ is an arbitrary function independent of y . The resulting cell problem is

$$-\nabla_y \cdot (k_1 \nabla_y U_1^i) = \nabla_y \cdot (k_1 \hat{e}^i) \quad \text{in } Y \setminus S$$

$$-\nabla_y \cdot (k_2 \nabla_y U_2^i) = \nabla_y \cdot (k_2 \hat{e}^i) \quad \text{in } S$$

$$(k_1 \nabla_y U_1^i) \cdot \hat{n} - f(U_1^i, U_2^i) = -k_1 \hat{e}^i \quad \text{on } \Sigma$$

$$(k_2 \nabla_y U_2^i) \cdot \hat{n} - f(U_1^i, U_2^i) = -k_2 \hat{e}^i \quad \text{on } \Sigma,$$

with U_1^i, U_2^i being Y -periodic. Since the macroscopic fields are identical, we are left with a single, classical, transport equation where the conductivity is dependent on the interfacial exchange from the cell problem:

$$\frac{\partial}{\partial x_i} k_{\alpha}^{eff} \frac{\partial u^0}{\partial x_k} = 0,$$

$$k_{\alpha,ik}^{eff} = \int_Y k_{\alpha,ij} \left(\delta_{jk} + \frac{\partial U^k}{\partial y_j} \right) dy,$$

where U^k stands for U_1^k and U_2^k in $Y \setminus S$ and S respectively.

$\mathcal{O}(\varepsilon^0)$

At the next order, the process remains the same. However, the local problem forces a single macroscopic concentration field

$$u_1^0(x) = u_2^0(x) = u^0(x),$$

as in the previous example. From the increased scaling, the interfacial behavior does not carry over to the cell problems, and so the resulting effective behavior is independent of the interface. Accordingly,

$$\begin{aligned} -\nabla_y \cdot (k_1 \nabla_y U_1^i) &= \nabla_y \cdot (k_1 \hat{e}^i) && \text{in } Y \setminus S \\ -\nabla_y \cdot (k_2 \nabla_y U_2^i) &= \nabla_y \cdot (k_2 \hat{e}^i) && \text{in } S \\ (k_1 \nabla_y U_1^i) \cdot \hat{n} &= -k_1 \hat{e}^i && \text{on } \Sigma \\ (k_2 \nabla_y U_2^i) \cdot \hat{n} &= -k_2 \hat{e}^i && \text{on } \Sigma, \end{aligned}$$

with U_1^i, U_2^i being Y -periodic. Again we are left with a single, classical, transport equation where the conductivity is now independent of the interfacial exchange:

$$\begin{aligned} \frac{\partial}{\partial x_i} k_\alpha^{eff} \frac{\partial u^0}{\partial x_k} &= 0. \\ k_{\alpha,ik}^{eff} &= \int_Y k_{\alpha,ij} \left(\delta_{jk} + \frac{\partial U^k}{\partial y_j} \right) dy. \end{aligned}$$

$\mathcal{O}(\varepsilon^p), p \geq 1$

For situations with $p > 1$, the procedure and cell problems are identical to $p = 1$, but with the interface exchange being removed. Results can be obtained by simply setting $f = 0$ in the relevant sub-problems.

Examples of effective interfacial contribution

The approach described uses an general interface reaction form $f(u_1, u_2)$. If we instead consider the typical interface adsorption condition or resistive interface where

$$f(u_1, u_2) = k_s(u_1 - u_2),$$

we can investigate the contribution of the interface to the homogenized behavior. For the case discussed above where the interface is $\mathcal{O}(\varepsilon^1)$, the macroscale field has

a body source term

$$\begin{aligned} \frac{1}{|Y|} \int_{\Sigma} f(u_1^0, u_2^0) ds &= \frac{1}{|Y|} \int_{\Sigma} k_s(u_1^0 - u_2^0) ds \\ &= k_s(u_1^0 - u_2^0) \frac{1}{|Y|} \int_{\Sigma} ds. \end{aligned}$$

So, for various microstructures, we wish to examine the surface area/volume (S) as a function of volume fraction of phase 1, V . The results of these are summarized in Fig. 5.2, with comparison to the model implemented in Ch. 6 for the homogenized reaction, $\rho(1 - \rho)$, with ρ denoting the volume fraction in the unit cell.

Hexagonal arrangement of triangles

Centering a flipped isosceles triangle of dimension r in a unit isosceles, the surface area between the two phases increases as r increases to a point and then decreases as the second phase takes over:

$$V = \begin{cases} r^2 & r < 1/2 \\ \frac{-1}{3} (x(x-4) + 1) & r > 1/2 \end{cases}$$

$$S = \begin{cases} 4\sqrt{3}r & r < 1/2 \\ 4/\sqrt{3}(2-x) & r > 1/2 \end{cases}$$

Close packed disks

Centering a disks of dimension r at the corners of a unit isosceles, we approximate a hexagonal packing of disks:

$$V = \begin{cases} \frac{2\pi}{\sqrt{3}} r^2 & r < 1/2 \\ \frac{1}{\sqrt{3}} \left(\sqrt[3]{4r^2 - 1} + 2r^2(\pi - 6 \operatorname{arcsec}(2r)) \right) & r > 1/2 \end{cases}$$

$$S = \begin{cases} \frac{4}{\sqrt{3}} \pi r & r < 1/2 \\ \frac{4}{\sqrt{3}} \left(\pi r - 6r \arccos(1 - 1/(2r)(2r - 1)) \right) & r > 1/2 \end{cases}$$

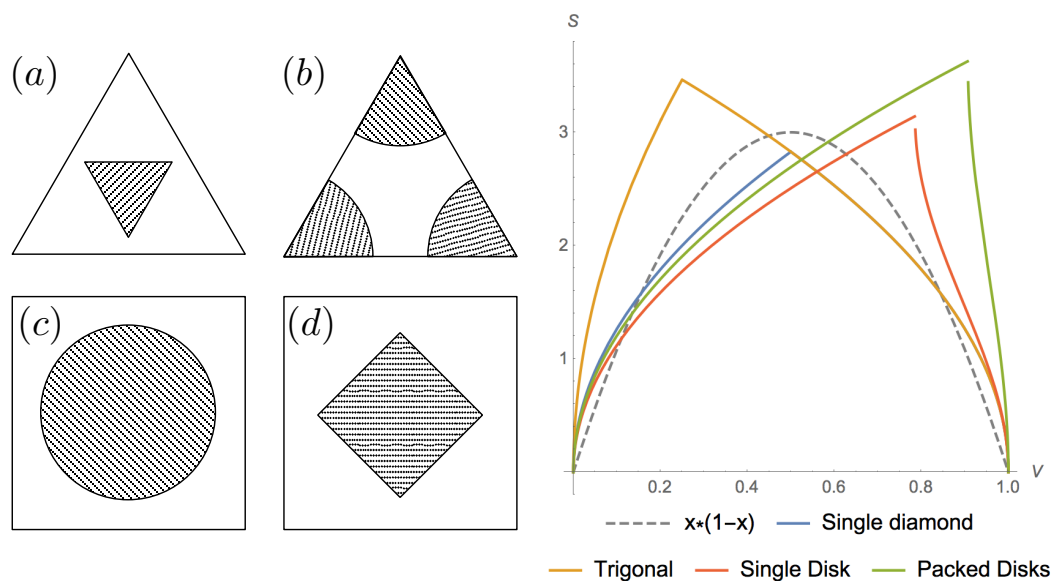


Figure 5.2: (a) Hexagonal arrangement of triangles; (b) close packed disks; (c) single disk; (d) single diamond.

Single disk

Centering a disk of radius r in a unit square, the surface area between the two phases increases as ϵ increases to a point and then decreases as the second phase takes over:

$$V = \begin{cases} \pi r^2 & r < 1/2 \\ \pi r^2 - 4(r^2 \arccos(1/(2r))) - \frac{1}{2}\sqrt{r^2 - 1/4} & r > 1/2 \end{cases}$$

$$S = \begin{cases} 2\pi r & r < 1/2 \\ 2\pi r^2 - 8r \arccos(1/(2r)) & r > 1/2 \end{cases}$$

Single diamond

Centering a rotated square of length l in a unit square, the surface area between the two phases increases as l increases to a point and then decreases as the second phase takes over:

$$S(V) = \begin{cases} 4\sqrt{V} & V < 1/2 \\ 4\sqrt{1-V} & V > 1/2 \end{cases}$$

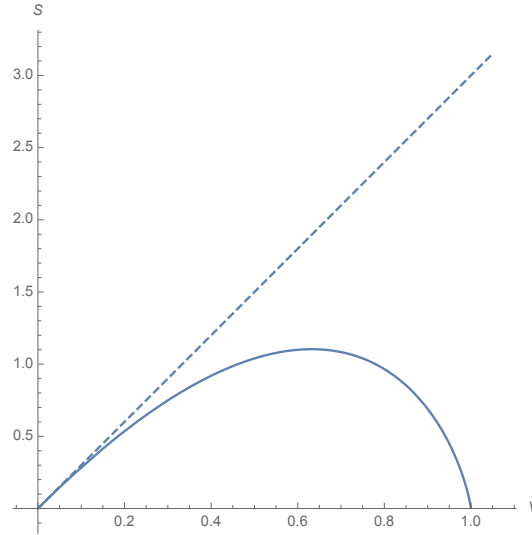


Figure 5.3: Dashed plot corresponds to the rigid case ($\lambda = 1$), and solid is the fully penetrable case ($\lambda = 0$).

Random collection of disks

Using the model of S. Torquato [144], we look at the collection of fully penetrable spheres ($\lambda = 0$) and fully rigid spheres $\lambda = 1$:

$$V = \begin{cases} \rho \frac{4}{3} \pi r^3 & \lambda = 1 \\ 1 - \exp\left\{-\rho \frac{4}{3}\pi r^3\right\} & \lambda = 0 \end{cases}$$

$$S = \begin{cases} \rho 4\pi r^2 & \lambda = 1 \\ \rho 4\pi r^2 \exp\left\{-\rho \frac{4}{3}\pi r^3\right\} & \lambda = 0 \end{cases}$$

Here, ρ is the number of spheres per volume. For the plot generated, we use unit disks in a 10×10 square domain. The volume fraction is controlled by the number of spheres considered. For the rigid case, 0 to 25 disks are calculated, whereas for the fully penetrable case ($\lambda = 0$), 200 spheres were necessary to completely cover the domain. Notice that the fully rigid model is only applicable to 0.9, or the hexagonal packing fraction of disks. For the penetrable case, the random arrangement maximizes the surface area as the number of disks increases, but as overlap increases, the effective interface between the two phases decreases.

5.2 Convection-Absorption-Diffusion

We expand on the previous problem to now address reactive flow through a porous material involving two species with flow rates falling into the Stokes regime. The goal is to work through the typical asymptotic analysis and homogenization of a

coupled system of equations tracking the gas velocity field (through Stokes flow), the gaseous species concentration at steady-state (convection-diffusion), and finally the solid species concentration at steady-state (diffusion equation). For the interfacial reaction, we now restrict ourselves to the case of linearized exchange, or absorption, between phases.

As with the previous problem, scaling the transport behavior and contribution determine the effective behavior observed after the asymptotic analysis. In particular, we must properly choose these scalings to capture the coupling between each of the transport regimes that we are considering and the included reaction. In this particular case, we consider the transport of the gaseous species being dominated by convective transport. Thus, we incorporate a ε^{-2} scaling for the convective term, with ε representing the characteristic length scale of our porous medium. Different scalings will be investigated as a way of looking at the influence of having surface-limited reaction or diffusion-limited transport, and have been examined thoroughly with having volumetric reaction but without the interfacial contributions [102, 100]. We start with the interfacial-scaling from the previous examination corresponding to macroscopic reaction terms as well as a conductivity depending on the interface; the boundary condition will be of order $\mathcal{O}(\varepsilon)$. In this problem, most of the techniques are found in Sanchez-Palencia [88] and Allaire [109] for the homogenization of the Stokes problem and convection-diffusion, respectively. We will work through each of these separately, being that the homogenization of the Stokes equations remains unchanged from Sanchez-Palencia's presentation.

Coupled set of equations

We now consider the pressure p and velocity fields \underline{b} , the concentration of gaseous species u and solid species v , and their interaction through Stokes flow, convection-

diffusion, and diffusion respectively:

$$\begin{cases} -\nabla p + \Delta b = 0 & \text{in } \Omega_p^\varepsilon \\ \nabla \cdot b = 0 & \text{in } \Omega_p^\varepsilon \\ b = 0 & \text{on } \Sigma \end{cases}$$

$$\begin{cases} \frac{1}{\varepsilon^2} b \cdot \nabla u_1 - \nabla \cdot k_1(y) \nabla u_1 = 0 & \text{in } \Omega_p^\varepsilon \\ (-k_1 \nabla u_1) \cdot \hat{n} = \varepsilon k_s (u_1 - u_2) & \text{on } \Sigma \end{cases}$$

$$\begin{cases} -\nabla \cdot k_2 \nabla u_2 = 0 & \text{in } \Omega_s^\varepsilon \\ (-k_2 \nabla u_2) \cdot \hat{n} = \varepsilon k_s (u_1 - u_2) & \text{on } \Sigma \end{cases}$$

Here, the diffusivities are set to vary with the pore length scale ($y = x/\varepsilon$), but could be taken to be constant in each of the domains considered.

Asymptotics

The typical hypothesis for asymptotic behavior is that the resulting solutions $\underline{b}^\varepsilon$, p^ε , u_1^ε and u_2^ε can be written as series expansions in terms of our characteristic length scale that are periodic over our unit cells. In this case we use a standard expansion for most of the fields in question, except increase the powers of ε on our velocity field, \underline{b} , as per Sanchez-Palencia [88]:

$$\underline{b}^\varepsilon(x, y) = \sum_{j=0}^{\infty} \varepsilon^{j+2} b^j(x, y),$$

$$p^\varepsilon = p^0(x) + \sum_{j=1}^{\infty} \varepsilon^j p^j(x, y),$$

$$u_1^\varepsilon(x, y) = \sum_{j=0}^{\infty} \varepsilon^j u_1^j(x, y),$$

and a similar expansion for u_2^ε . Now, noting the chain rule

$$\nabla(\cdot) = (\nabla_x + \varepsilon^{-1} \nabla_y)(\cdot),$$

$$\Delta(\cdot) = (\Delta_x^2 + \varepsilon^{-1} \operatorname{div}_x \nabla_y + \varepsilon^{-1} \operatorname{div}_y \nabla_x + \varepsilon^{-2} \Delta_y^2)(\cdot),$$

we can start breaking our governing PDE system into subproblems corresponding to orders of ε .

Stokes homogenization

Since the homogenization of the Stokes equations is found in the work of Sanchez-Palencia [88], we will just present the major results. From the chosen scaling,

the fluid transport and corresponding velocity field have been (up to the orders considered) uncoupled from the other transport models. We obtain the macroscopic equation from our incompressibility requirement:

$$\operatorname{div}_x b^0 + \operatorname{div}_y b^1 = 0.$$

Averaging over the unit cell Y , we find:

$$\operatorname{div}_x \bar{b}^0 = 0.$$

Looking at the $O(1)$, $O(\varepsilon)$, $O(\varepsilon^2)$

$$\begin{aligned} -\frac{\partial p^1}{\partial y^i} + \Delta_y b_i^0 + (f_i - \frac{\partial p^0}{\partial x^i}) &= 0 \quad \text{in } Y \setminus S, \\ \operatorname{div}_y b^0 &= 0 \quad \text{in } Y \setminus S, \\ b^0 &= 0 \quad \text{on } \Sigma. \end{aligned}$$

Examining the local problem, we define a function space of Y -periodic functions:

$$\begin{aligned} V_Y &= \{u; u \in H^1(Y \setminus S); u|_\Sigma = 0; \operatorname{div}_y u = 0; Y\text{-periodic}\}, \\ (u, w)_{V_Y} &= \int_{Y \setminus S} \frac{\partial u_i}{\partial y_k} \frac{\partial w_i}{\partial y_k} dy. \end{aligned}$$

Now, to find a variational formulation of our local problem, we take $w \in V_Y$, multiply our local PDE and integrate over Y_f to obtain

$$(v^0, w)_{V_Y} = (f_i - \frac{\partial p^0}{\partial x^i}) \int_{Y \setminus S} w_i dy \quad \forall w \in V_Y.$$

Thus, we reduce the local problem to finding b^0 satisfying this condition. The proposed solution $b^0(x, y)$ is given by $f_i(x)$ and $\partial p^0 / \partial x^i$ as

$$b^0 = (f_i - \frac{\partial p^0}{\partial x^i}) b^i,$$

with b^i satisfying

$$(b^i, w)_{V_Y} = \int_{Y \setminus S} w_i dy \quad \forall w \in V_Y.$$

When we average this over the unit cell, add in the contribution of viscosity, and neglect the source contribution we find the computed version of Darcy's law yielding the desired macroscopic velocity field:

$$\bar{b}_j^0 = -\frac{K_{ij}}{\mu} \frac{\partial p^0}{\partial x^i}; \quad K_{ij} = \bar{b}_j^i.$$

The volume averaged permeability K_{ij} is dependent on the microstructure through the volume-averaged cell solutions \bar{b}_j^i , and explicit calculation would require explicit solving (either numerically or analytically) over a known microstructure.

Coupled diffusion homogenization

Starting with the $O(\varepsilon^{-2})$ terms from the PDE's and the boundary conditions of $O(\varepsilon^{-1})$, we find

$$\begin{aligned} \nabla_y \cdot (k_1 \nabla_y u_1^0) &= 0 & \text{in } Y \setminus S, \\ \nabla_y \cdot (k_2 \nabla_y u_2^0) &= 0 & \text{in } S, \\ (-k_1 \nabla_y u_1) \cdot \hat{n} &= (-k_2 \nabla_y u_2) \cdot \hat{n} = 0 & \text{on } \Sigma. \end{aligned}$$

As before, we find our macroscopic relation stating that our homogenized solution is independent of our fine scale structure:

$$u_1^0 = u_1^0(x), \quad u_2^0 = u_2^0(x).$$

Collecting the $O(\varepsilon^{-1})$ terms from the governing PDE's, and the $O(\varepsilon^0)$ terms from the boundary conditions, we can write the local problem:

$$\begin{aligned} -\nabla_y \cdot (k_1 (\nabla_x u_1^0 + \nabla_y u_1^1)) &= 0 & \text{in } Y \setminus S, \\ -\nabla_y \cdot (k_2 (\nabla_x u_2^0 + \nabla_y u_2^1)) &= 0 & \text{in } S, \\ -k_1 (\nabla_x u_1^0 + \nabla_y u_1^1) \cdot \hat{n} &= -k_2 (\nabla_x u_2^0 + \nabla_y u_2^1) \cdot \hat{n} = 0 & \text{on } \Sigma. \end{aligned}$$

The cell problems are therefore written as:

$$\begin{aligned} -\nabla_y \cdot (k_1 \nabla_y U_1^i) &= \nabla_y \cdot (k_1 \hat{e}^i) & \text{in } Y \setminus S, \\ -\nabla_y \cdot (k_2 \nabla_y U_2^i) &= \nabla_y \cdot (k_2 \hat{e}^i) & \text{in } S, \\ (k_1 \nabla_y U_{1i}) \cdot \hat{n} &= -k_1 \hat{e}^i & \text{on } \Sigma, \\ (k_2 \nabla_y U_{2i}) \cdot \hat{n} &= -k_2 \hat{e}^i & \text{on } \Sigma, \end{aligned}$$

and are Y -periodic. We write the solution to our local problem as the superposition:

$$\begin{aligned} u_1^1 &= \sum_{i=1}^n U_1^i (\nabla_x u_1^0 \cdot \hat{e}^i) + \bar{U}_1^1(x), \\ u_2^1 &= \sum_{i=1}^n U_2^i (\nabla_x u_2^0 \cdot \hat{e}^i) + \bar{U}_2^1(x), \end{aligned}$$

where $\bar{U}_1^1(x)$ and $\bar{U}_2^1(x)$ are arbitrary functions independent of y .

Equipped with our local solutions u_1^1 and u_2^1 , we move on to the transport equations at $O(\varepsilon^0)$ and boundary conditions at $O(\varepsilon^1)$ to obtain the compatibility conditions

for our homogenization and the homogenized form of the transport equations:

$$\begin{aligned}
b^0 \cdot \nabla_x u_1^0 + b_0 \cdot \nabla_y u_1^1 - \nabla_x \cdot (k_1 \nabla_x u_1^0) + \nabla_x \cdot (k_1 \nabla_y u_1^1) - \nabla_y \cdot (k_1 \nabla_x u_1^1 + k_1 \nabla_y u_1^2) &= 0 \quad \text{in } Y \setminus S, \\
- \nabla_x \cdot (k_2 \nabla_x u_2^0) - \nabla_x \cdot (k_2 \nabla_y u_2^1) + \nabla_y \cdot (k_2 \nabla_x u_2^1 + k_2 \nabla_y u_2^2) &= 0 \quad \text{in } S, \\
- k_1 (\nabla_x u_1^1 + \nabla_y u_1^2) \cdot \hat{n} &= k_s (u_1^0 - u_2^0) \quad \text{on } \Sigma, \\
- k_2 (\nabla_x u_2^1 + \nabla_y u_2^2) \cdot \hat{n} &= k_s (u_1^0 - u_2^0) \quad \text{on } \Sigma.
\end{aligned}$$

The homogenized behavior is found by volume averaging over the unit cell Y . We again rely on the zero-continuation of each of our solutions to restrict the integration to the separate domains in consideration. Rearranging the first terms and taking the derivatives with respect to x out of the integral:

$$\begin{aligned}
\int_Y \nabla_x \cdot (k_1 \nabla_x u_1^0) dy &= \nabla_x \cdot \int_{Y \setminus S} k_1(y) dy \nabla_x u_1^0, \\
\int_Y \nabla_x \cdot (k_2 \nabla_x u_2^0) dy &= \nabla_x \cdot \int_S k_2(y) dy \nabla_x u_2^0.
\end{aligned}$$

With the set of second terms, we apply the local solutions. Starting with the terms involving u_1 :

$$\begin{aligned}
\int_Y \nabla_x \cdot (k_1 \nabla_y u_1^1) dy &= \nabla_x \cdot \int_{Y \setminus S} k_2 \nabla_y u_1^1 dy \\
&= \frac{\partial}{\partial x_i} \int_{Y \setminus S} k_{1,ij} \left(\frac{\partial U^k}{\partial y_j} \frac{\partial u_1^0}{\partial x_k} \right) dy,
\end{aligned}$$

and similarly for our other quantity:

$$\begin{aligned}
\int_Y \nabla_x \cdot (k_2 \nabla_y v^1) dy &= \nabla_x \cdot \int_S k_2 \nabla_y u_2^1 dy \\
&= \frac{\partial}{\partial x_i} \int_S k_{2,ij} \left(\frac{\partial V^k}{\partial y_j} \frac{\partial u_2^0}{\partial x_k} \right) dy.
\end{aligned}$$

To integrate the last term over a period, Y , we apply the divergence theorem. From the continuation of our solutions, these integrals are reduced to $Y \setminus S$ or S . From periodicity, the contributions from the external boundary vanish leaving the contributions from the interface. Under the assumed interfacial boundary conditions, this

becomes the exchange coefficient normalized by the measure of interface.

$$\begin{aligned}
\int_Y \nabla_y \cdot (k_1 \nabla_x u_1^1 + k_1 \nabla_y u_1^2) dy &= \int_{Y \setminus S} \nabla_y \cdot (k_1 \nabla_x u_1^1 + k_1 \nabla_y u_1^2) dy \\
&= \int_{\Sigma} (k_1 \nabla_x u_1^1 + k_1 \nabla_y u_1^2) \cdot \hat{n} ds \\
&= - \int_{\Sigma} (k_1 \nabla_x u_1^1 + k_1 \nabla_y u_1^2) \cdot \hat{n} ds \\
&= \int_{\Sigma} k_s (u_1^0 - u_2^0) ds \\
&= \mathcal{H}^{n-1}(\Sigma) k_s (u_1^0 - u_2^0) = |\Sigma| k_s (u_1^0 - u_2^0).
\end{aligned}$$

Rearranging these yields a form similar to a diffusion equation with body reaction:

$$\begin{aligned}
b_k^{eff} \frac{\partial u_1^0}{\partial x_k} - \frac{\partial}{\partial x_i} k_1^{eff} \frac{\partial u_1^0}{\partial x_k} &= k_s^{eff} (u_1^0 - u_2^0) \\
- \frac{\partial}{\partial x_i} k_2^{eff} \frac{\partial u_2^0}{\partial x_k} &= -k_s^{eff} (u_1^0 - u_2^0).
\end{aligned}$$

Here,

$$\begin{aligned}
b_k^{eff} &= \int_{Y \setminus S} b_j^0 \left(\delta_{jk} + \frac{\partial U_1^k}{\partial y_j} \right) dx, \\
k_1^{eff} &= \int_{Y \setminus S} k_{1,ij} \left(\delta_{jk} + \frac{\partial U_1^k}{\partial y_j} \right) dy \\
k_2^{eff} &= \int_Y k_{2,ij} \left(\delta_{jk} + \frac{\partial U_2^k}{\partial y_j} \right) dy, \\
k_s^{eff} &= \int_{\Sigma} k_s ds.
\end{aligned}$$

Thus, we notice that we have obtained an effective diffusivity for each species that takes into account the solutions to the cell problem, as well as a body source term that depends on the adsorption boundary conditions that we prescribe. In the case of the porous species, we find that we take into account the averaged fluid velocity is found only in the convective term, and does not factor into the chemistry. Thus, we have effectively decoupled the Stokes-flow from the rest of the transport regimes. At higher flows, a different scaling would be more realistic. At alternate scalings, the convective behavior will find its way into the source term and conductivity, as the cell problems become convective.

Alternate interface scaling

As explored previously, the scaling of the interface changes the macroscopic behavior. The convective contribution remains unchanged, and the results are nearly the same as seen in 5.1.

$O(\varepsilon^p)$, $p \leq -2$

The corresponding effective behavior and cell problems will be presented. Using the definition presented here, a scaling of $O(\varepsilon^p)$, $p = -2$ represents a classical conduction problem in a composite with barrier resistance. The effective behavior reduces to a single Poisson equation over Y

$$\begin{aligned} b_k^{eff} \frac{\partial u^0}{\partial x_k} - \frac{\partial}{\partial x_i} k_{\alpha,ik}^{eff} \frac{\partial u^0}{\partial x_k} &= 0, \\ b_k^{eff} &= \int_{Y \setminus S} b_j^0 \left(\delta_{jk} + \frac{\partial U_1^k}{\partial y_j} \right) dx, \\ k_{\alpha,ik}^{eff} &= \int_Y k_{\alpha,ij} \left(\delta_{jk} + \frac{\partial U^k}{\partial y_j} \right) dy, \end{aligned}$$

where $\alpha = 1$ in $Y \setminus S$ and $\alpha = 2$ in S . U^k is the solution Y -periodic solution to the cell problem

$$\begin{aligned} \frac{\partial}{\partial y_i} \left[k_{\alpha,ij} \left(\delta_{jk} + \frac{\partial U^k}{\partial y_j} \right) \right] &= 0 \text{ in } Y \\ \tilde{U}^k &= 0 \\ k_{1,ij} \left(\delta_{jk} + \frac{\partial U^k}{\partial y_j} \right) n_i &= k_{2,ij} \left(\delta_{jk} + \frac{\partial U^k}{\partial y_j} \right) n_i \text{ on } \Sigma, \end{aligned}$$

where $\tilde{\cdot} = \frac{1}{|Y|} \int_Y \cdot dx$ denotes a volume average. Situations where the interface exchange is $O(\varepsilon^p)$, $p \leq -2$ follow the same derivation.

$O(\varepsilon^{-1})$

As the exchange is increased with respect to ε , we find that we again have a single resulting macroscopic field

$$u_1^0(x) = u_2^0(x) = u^0(x),$$

that yields a similar cell-problem to what we examined. However, the cell solutions are not the same in each phase, namely they are linear functions with respect to the

gradient of the macroscopic field

$$u_1^1 = \sum_{i=1}^n U_{1i}(\nabla_x u_1^0 \cdot \hat{e}^i) + \bar{U}_1^1(x)$$

$$u_2^1 = \sum_{i=1}^n U_{2i}(\nabla_x u_2^0 \cdot \hat{e}^i) + \bar{U}_2^1(x).$$

$\bar{U}^1(x)$ is an arbitrary function independent of y . The resulting cell problem is

$$\begin{aligned} -\nabla_y \cdot (k_1 \nabla_y U_1^i) &= \nabla_y \cdot (k_1 \hat{e}^i) && \text{in } Y \setminus S \\ -\nabla_y \cdot (k_2 \nabla_y U_2^i) &= \nabla_y \cdot (k_2 \hat{e}^i) && \text{in } S \\ (k_1 \nabla_y U_1^i) \cdot \hat{n} + f(U_1^i, U_2^i) &= -k_1 \hat{e}^i && \text{on } \Sigma \\ (k_2 \nabla_y U_2^i) \cdot \hat{n} - f(U_1^i, U_2^i) &= -k_2 \hat{e}^i && \text{on } \Sigma, \end{aligned}$$

with U_1^i, U_2^i being Y -periodic. Since the macroscopic fields are identical, we are left with a single, classical, transport equation where the conductivity is dependent on the interfacial exchange from the cell problem:

$$\begin{aligned} b_k^{eff} \frac{\partial u_1^0}{\partial x_k} - \frac{\partial}{\partial x_i} k_{\alpha,ik}^{eff} \frac{\partial u^0}{\partial x_k} &= 0, \\ b_k^{eff} &= \int_{Y \setminus S} b_j^0 \left(\delta_{jk} + \frac{\partial U_1^k}{\partial y_j} \right) dx, \\ k_{\alpha,ik}^{eff} &= \int_Y k_{\alpha,ij} \left(\delta_{jk} + \frac{\partial U^k}{\partial y_j} \right) dy, \end{aligned}$$

where U^k stands for U_1^k and U_2^k in $Y \setminus S$ and S respectively.

$\mathcal{O}(\varepsilon^0)$

At the next order, the process remains the same. However, the local problem forces a single macroscopic concentration field

$$u_1^0(x) = u_2^0(x) = u^0(x),$$

as in the previous example. From the increased scaling, the interfacial behavior does not carry over to the cell problems, and so the resulting effective behavior is independent of the interface. Accordingly,

$$\begin{aligned} -\nabla_y \cdot (k_1 \nabla_y U_1^i) &= \nabla_y \cdot (k_1 \hat{e}^i) && \text{in } Y \setminus S \\ -\nabla_y \cdot (k_2 \nabla_y U_2^i) &= \nabla_y \cdot (k_2 \hat{e}^i) && \text{in } S \\ (k_1 \nabla_y U_1^i) \cdot \hat{n} &= -k_1 \hat{e}^i && \text{on } \Sigma \\ (k_2 \nabla_y U_2^i) \cdot \hat{n} &= -k_2 \hat{e}^i && \text{on } \Sigma, \end{aligned}$$

with U_1^i, U_2^i being Y -periodic. Again we are left with a single, classical, transport equation where the conductivity is now independent of the interfacial exchange:

$$b_k^{eff} \frac{\partial u_1^0}{\partial x_k} - \frac{\partial}{\partial x_i} k_{\alpha,ik}^{eff} \frac{\partial u^0}{\partial x_k} = 0,$$

$$b_k^{eff} = \int_{Y \setminus S} b_j^0 \left(\delta_{jk} + \frac{\partial U_1^k}{\partial y_j} \right) dx,$$

$$k_{\alpha,ik}^{eff} = \int_Y k_{\alpha,ij} \left(\delta_{jk} + \frac{\partial U^k}{\partial y_j} \right) dy.$$

$\mathcal{O}(\varepsilon^p)$, $p \geq 1$

For situations with $p > 1$, the procedure and cell problems are identical to $p = 1$, but with the interface exchange being removed. Results can be obtained by simply setting $f = 0$ in the relevant sub-problems.

5.3 Summary

We have examined the homogenization of mass transport in porous mixed conductors under two separate models: one dealing with diffusion through each phase coupled through a nonlinear interface exchange, the other tracking fluid flow, convective-diffusion, and bulk diffusion with a linearized interface exchange. In both situations, we have found that the effective behavior depends strongly on the prescribed scaling of the interface. When the interface exchange is very large with respect to diffusion, the averaged behavior reduces to a single convective-diffusion equation over the averaged material where the concentrations of each species are equal. At the interface scaling order $\mathcal{O}(\varepsilon^{-1})$, we again find a single concentration field, but the effective behavior is now dependent on the interface at the cell level. The final "class" of effective behaviors results when the interface scales with $\mathcal{O}(\varepsilon^1)$, where we find two separate fields being described by a volume-averaged convective-diffusion equation and a diffusive equation in the pore space and the bulk, respectively. Here, the interface exchange carries through to the effective behavior as a volume-averaged body source (or sink) dependent on the amount of interface between phases in each cell. We have sketched this reaction contribution for a variety of simple cell designs as a function of volume fraction, and found that the reaction is maximized for intermediate densities. In the next chapter, we implement this behavior in a relaxed optimal design problem for a similar transport model. Similar, more rigorous, couplings between homogenization and optimal design are common in literature [109], and offer a path to topology optimization at two separate length scales for the

development of hierarchical materials.

We notice that because of the chosen scaling on the convective transport in the second formulation, the fluid flow homogenization has been uncoupled from the other transport regimes and yields the traditional form of Darcy's law. Examining additional convective scalings requires higher-order equations describing the fields at the level of the cell-problem, i.e. additional sub-problems would need to be introduced in order to fully compute the effective behavior. We have reduced the problem to only studying the scaling between diffusion and interface exchange, which explains the similarities with the first problem presented. We chose to neglect a surface concentration, but similar analysis have addressed such a situation [101, 98]. Additionally, we have assumed steady-state behavior in this analysis. Introduction of drift into our two-scale expansions is a method to account for any temporal effects on the process [102, 145].

Chapter 6

OPTIMAL DESIGN

6.1 Introduction

In this chapter, we study a model system motivated by metal oxides in solar-driven thermochemical conversion devices. We have a two phase material (solid oxide and pore) where reactions at the surface create (gaseous) oxygen in the carrier gas in the pores and bound oxygen in the solid oxide; the oxygen diffuses through the carrier gas in the porous region and bound oxygen diffuses through the solid oxide. We seek to understand the arrangement of the solid and porous regions to maximize the transport given sources and sinks for the gaseous oxygen and vacancies.

We begin with the formulation of the physical problem, shown in Figure 6.1, in Section 6.2. We start with a sharp interface formulation. However, the optimal design of the sharp interface model is mathematically ill-posed, and therefore we study the analogous diffuse interface model. We also note that homogenization of the sharp interface model leads to equations of the same form as the diffuse interface equations. The transport of two chemical species with concentration u_1 and u_2 is governed by the following reaction diffusion equations for $i = 1, 2$:

$$\begin{cases} \nabla \cdot k_i \nabla u_i = f_i, & \text{in } \Omega, \\ k_i \nabla u_i \cdot \hat{n} = 0 & \text{on } \partial\Omega \setminus \partial_i\Omega \\ u_i = u_i^* & \text{on } \partial_i\Omega, \end{cases} \quad (6.1)$$

where the isotropic conductivities are

$$k_1(x) = k_{11}\chi(x) + k_{12}(1 - \chi(x)), \quad k_2(x) = k_{21}\chi(x) + k_{22}(1 - \chi(x)); \quad (6.2)$$

with $k_{11}, k_{22} \gg k_{12}, k_{21} > 0$, and the sources are

$$f_1 = -f_2 = \chi(1 - \chi)k_s(u_1 - u_2) \quad (6.3)$$

for $k_s > 0$ and $\chi : \Omega \rightarrow [0, 1]$. Briefly, we have a two-material system and χ describes the volume fraction of material 1 (say solid phase). Chemical species 1 (say bound oxygen) diffuses preferentially in material 1 ($\chi = 1$) while species 2 (say oxygen gas) diffuses preferentially in material 2 (say pore, $\chi = 0$). The species react

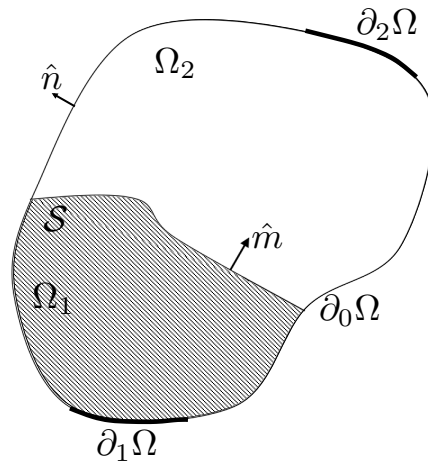


Figure 6.1: The physical setting: chemical species 1 enters through the source $\partial_1\Omega$, diffuses through Ω_1 , is converted to chemical species 2 through a surface reaction at the interface \mathcal{S} , chemical species 2 diffuses through Ω_2 and leaves through the sink $\partial_2\Omega$.

and therefore there is a source at the interface $\chi \neq 0, 1$. For future use, we write the source as $f = \chi(1 - \chi)Au$ where $f = \{f_1, f_2\}$, $u = \{u_1, u_2\}$ and

$$A = k_s \begin{pmatrix} 1 & -1 \\ -1 & 1 \end{pmatrix}.$$

This problem allows a variational formulation, and the direct method of the calculus of variation allows us to prove existence of a solution.

We study the optimal design problem of maximizing the flux of species through the reactor over all possible arrangements χ in Section 6.3. We show that this gives rise to a saddle point problem. We then obtain an explicit characterization which shows that the mixed phase regions arise naturally. To understand this further through particular examples, we introduce a phase field formulation in Section 6.5. Specifically, we add an Allen-Cahn type energy to that associated with the variational formulation of the transport problem and then solve the gradient flow associated with this energy. We solve this numerically in selected examples and conduct a parameter study. These show that the optimal design can be quite intricate as it seeks to balance transport and reaction.

6.2 Formulation

Sharp interface formulation

Consider an open, bounded region $\Omega \subset \mathbb{R}^n$ with Lipschitz boundary separated into two regions Ω_1 and Ω_2 by an interface \mathcal{S} show in Figure 6.1. We consider the

diffusion of one species with concentration u_1 in region Ω_1 with isotropic diffusivity $K_1 > 0$, and a second species with concentration u_2 in region Ω_2 with isotropic diffusivity $K_2 > 0$. The two species meet at the interface and react with reaction rate $k_s > 0$. The boundary of Ω is divided into three regions $\partial\Omega = \partial_1\Omega \cup \partial_2\Omega \cup \partial_0\Omega$ where $\partial_i\Omega \subset \partial\Omega_i$. The concentration of species i is held at a prescribed value u_i^* on $\partial_i\Omega$ while $\partial_0\Omega$ is insulating. This is described by the following system of equations:

$$\begin{cases} \nabla \cdot K_i \nabla u_i = 0 & \text{in } \Omega_i \\ -K_i \nabla u_i \cdot \hat{m} = k_s(u_1 - u_2) & \text{on } \mathcal{S} \\ u_i = u_i^* & \text{on } \partial_i\Omega \\ K_i \nabla u_i \cdot \hat{n} = 0 & \text{on } \partial\Omega \setminus \partial_i\Omega \end{cases} \quad (6.4)$$

for $i = 1, 2$ where \hat{m} represents the normal to \mathcal{S} pointing from Ω_1 pointing to Ω_2 , and \hat{n} represents the outward normal to $\partial\Omega$.

Diffuse interface formulation

It is often convenient to work with a smooth or diffuse interface formulation of the problem above. We now show formally that the diffuse interface formulation in (6.1)-(6.3) leads to the sharp interface formulation in (6.4) in an asymptotic limit. Let χ be the characteristic function of Ω_1 as defined in Section 6.2. Let χ^η be the mollification of χ with a standard mollifier at length-scale η : $\chi^\eta = \varphi^\eta * \chi$ where $\varphi^\eta(x) = \eta^{-n} \varphi(x/\eta)$. Let k_1^η, k_2^η be as in (6.2) with $\chi = \chi^\eta$ and $k_{12}^\eta = (1 - \exp(-\eta))k_{12}$, $k_{21}^\eta = (1 - \exp(-\eta))k_{21}$, and $f_i^\eta(x) = f_i(x/\eta)$. Let u_i^η solve

$$\nabla \cdot k_i^\eta \nabla u_i^\eta = \eta^2 f_i^\eta, \quad i = 1, 2 \quad \text{in } \Omega. \quad (6.5)$$

First consider the outer expansion $\eta \rightarrow 0$, and note that (6.5) formally gives (6.4)_{1,3,4} in $\Omega_{1,2}$. Further, note that u_1 (respectively u_2) is indeterminate on Ω_2 (respectively Ω_1). However, this outer expansion does not give any condition on the interface \mathcal{S} . To obtain this condition, denote the limiting values on the interface to be \bar{u}_1, \bar{u}_2 . We seek to relate these to the flux as in (6.4)₂.

Now consider the inner expansion. Pick a point $x_0 \in \mathcal{S}$ and change variables $x \mapsto (x - x_0)/\eta$. We obtain

$$\nabla \cdot k_i \nabla u_i = f_i, \quad i = 1, 2 \quad (6.6)$$

where $k_i = k_i^1$. Further, as $\eta \rightarrow 0$, χ and hence the solution depend only on one dimension that is normal to the interface. We take this direction to be x_1 by

changing variables if necessary. Let U_i solve (6.6) for the boundary conditions $(u_1, u_2)(x_1) \rightarrow (1, 0)$ as $x_1 \rightarrow -\infty$ and $(u_1, u_2)(x_1) \rightarrow (0, 1)$ as $x_1 \rightarrow \infty$, and V_i solve (6.6) for the boundary conditions $(u_1, u_2)(x_1) \rightarrow (1, 0)$ as $x_1 \rightarrow -\infty$ and $(u_1, u_2)(x_1) \rightarrow (0, -1)$ as $x_1 \rightarrow \infty$. Note that

$$u_i = \alpha U_i + \beta V_i + \gamma$$

also solves (6.6) for any arbitrary scalars α, β, γ , and satisfies the boundary conditions

$$u_1 \rightarrow \alpha + \beta + \gamma \text{ as } x_1 \rightarrow -\infty, \quad u_2 \rightarrow \alpha - \beta + \gamma \text{ as } x_1 \rightarrow \infty.$$

Further, by integrating (6.6), we find that the flux

$$J = [[-k_i \nabla u_1 \cdot e_1]]_{-\infty}^{\infty} = K_1 u_1'(-\infty) = [[k_i \nabla u_2 \cdot e_1]]_{-\infty}^{\infty} = -K_2 u_2'(+\infty) = \alpha J_U + \beta J_V$$

where J_U, J_V are the fluxes associated with the solutions U and V respectively. It is easy to verify that we can find α, β, γ to satisfy the boundary conditions $u_1(-\infty) = \bar{u}_1, u_2(\infty) = \bar{u}_2$ as well as the flux condition $J = k_s(\bar{u}_1 - \bar{u}_2)$. We obtain (6.4)₂.

Homogenization of the sharp interface formulation

We briefly revisit the relevant results from Ch. 5. Consider the situation where the domain Ω is made of a periodic microstructure at a scale $\varepsilon \ll 1$. Specifically, let Y be the unit cube consisting of two subdomains Y_1 and Y_2 separated by an interface Σ ; $Y = Y_1 \cup Y_2 \cup \Sigma$. We assume that $\Omega_1^\varepsilon = \cup_i \varepsilon(a_i + Y_1)$, $\Omega_2^\varepsilon = \cup_i \varepsilon(a_i + Y_2)$, and $S^\varepsilon = \cup_i \varepsilon(a_i + \Sigma)$. We assume that the equations (6.4) hold in this domain with the reaction coefficient of order ε : i.e., $k_s = \varepsilon K_s$ for some $K_s > 0$ independent of ε . Peter and Böhm [146] (also see Auriault and Ene [103]) show that this periodic system can be homogenized, and the homogenized equations are given by (6.1) where k_1, k_2 are given by the usual unit cell problem of diffusion and

$$f_1 = -f_2 = K_s \text{Area}(\Sigma)(\bar{u}_1 - \bar{u}_2)$$

where \bar{u}_i is the solution to the unit cell problem. Therefore, k_i, f_i depend not only on the volume fraction but also other aspects of the microstructure. However, we may view (6.2) and (6.3) as simple models for these.

Variational formulation

The following theorem provides a variational formulation of the problem (6.1) above.

Theorem 6.2.1. *Let $\Omega \subset \mathbb{R}^n$ be a bounded, connected open set with Lipschitz boundary,*

$$\chi \in \mathcal{X} = \{\chi \in L^2(\Omega; [0, 1])\}$$

be a given design and $\lambda \in \mathbb{R}$. The problem

$$\inf \left\{ L(u, \chi) = \int_{\Omega} \frac{1}{2} \sum_{i=1,2} k_i |\nabla u_i|^2 + \frac{1}{2} \chi(1 - \chi) u \cdot Au - \lambda \chi \, dx : u \in \mathcal{V} \right\}$$

where

$$\mathcal{V} = \{v \in H^1(\Omega; \mathbb{R}^2) : v_i = u_i^* \text{ on } \partial_i \Omega, i = 1, 2\}$$

attains its minimum. Further, the minimum is unique and satisfies the Euler-Lagrange equation

$$\int_{\Omega} \left(\sum_{i=1,2} k_i \nabla u_i \cdot \nabla \varphi_i + \chi(1 - \chi) \varphi \cdot Au \right) dx = 0 \quad (6.7)$$

for all $\varphi \in \mathcal{V}_0 = \{v \in H^1(\Omega; \mathbb{R}^2) : v_i = 0 \text{ on } \partial_i \Omega, i = 1, 2\}$.

Proof. Set

$$\inf \{L(u, \chi) : u \in \mathcal{V}\} = m$$

and observe that because our integrand is finite and satisfies the growth conditions

$$-\lambda \chi(x) \leq f(x, v, \xi) \leq c(1 + |v|^2 + |\xi|^2),$$

we have that $-\infty < m < +\infty$. Let u^ν be a minimizing sequence, i.e. $L(u^\nu, \chi) \rightarrow m$ as $\nu \rightarrow \infty$. For ν sufficiently large,

$$m + 1 \geq L(u^\nu, \chi) \geq \gamma_1 \|\nabla u^\nu\|_{L^2}^2 + \gamma_2 \|u^\nu\|_{L^2}^2 - \int_{\Omega} |\gamma_3(x)| \, dx \geq \gamma_1 \|\nabla u^\nu\|_{L^2}^2 - \gamma_4$$

with $\gamma_k > 0$ independent of ν since Ω is bounded. It follows that

$$\|u^\nu\|_{W^{1,2}} \leq \gamma_5.$$

appealing to our version of Poincaré's inequality (Lemma 6.2.2 below). We deduce that there exists a $\bar{u} \in \mathcal{V}$ and a subsequence (still denoted u^ν) that converges weakly in $W^{1,2}$: $u^\nu \rightharpoonup \bar{u}$ in $W^{1,2}$ as $\nu \rightarrow \infty$. It follows from the convexity of

the integrand (since $k_1, k_2, k_s > 0$) that the functional is sequentially weakly lower semicontinuous. Therefore,

$$\liminf_{\nu \rightarrow \infty} L(u^\nu, \chi) \geq L(\bar{u}, \chi)$$

and hence \bar{u} is a minimizer of (P).

A simple calculation shows that any minimizer satisfies the Euler-Lagrange equation (6.7). We prove the uniqueness of the minimum by contradiction. Suppose $L(u, \chi) = L(v, \chi) = m$. Then,

$$\int_{\Omega} \left(\frac{1}{2} \sum_{i=1,2} k_i (|\nabla u_i|^2 - |\nabla v_i|^2) + \frac{1}{2} \chi(1 - \chi)(u \cdot Au - v \cdot Av) \right) dx = 0.$$

Further, since $u, v \in \mathcal{V}$, $u - v \in \mathcal{V}_0$. Therefore, from the Euler-Lagrange equation (6.7) for v , we conclude

$$\int_{\Omega} \left(\sum_{i=1,2} k_i |\nabla v_i|^2 + \chi(1 - \chi)v \cdot Av - \sum_{i=1,2} k_i \nabla u_i \cdot \nabla v_i - \chi(1 - \chi)v \cdot Au \right) dx = 0$$

Adding these two equations,

$$\frac{1}{2} \int_{\Omega} \left(\sum_{i=1,2} k_i |\nabla u_i - \nabla v_i|^2 + \chi(1 - \chi)(u - v) \cdot A(u - v) \right) dx = 0.$$

It follows that $\nabla u_i = \nabla v_i$ a.e. and $u - v = \psi(x)\{1, 1\}$. Together, we conclude that ψ is constant and from the boundary condition that $\psi = 0$. Thus $u = v$, giving us a contradiction. \square

We have used the following lemma.

Lemma 6.2.2. (Poincaré's inequality, adapted from [147]) *Let Ω and \mathcal{V} be as in the theorem above. There exists a constant c , depending only on n and Ω such that*

$$\|u - \bar{u}\|_{L^2} \leq c \|\nabla u\|_{L^2}$$

for each function $u \in \mathcal{V}$, where \bar{u} denotes the average over Ω .

6.3 Optimal design problem

We seek to find the arrangement of the two phases with a given volume of phase 1, v , that maximizes the normalized flux through the material:

$$O := \sup \left\{ \int_{\partial_1 \Omega} u_1^* k_1 \nabla u_1 \cdot \hat{n} dA - \int_{\partial_2 \Omega} u_2^* k_2 \nabla u_2 \cdot \hat{n} dA : \chi \in \mathcal{X}, \int_{\Omega} \chi dx = v \right\}. \quad (6.8)$$

Note that $k_i \nabla u_i \cdot \hat{n}$ gives the inward flux per unit area of species i into Ω . We normalize each flux by the prescribed concentration. Integrating by parts, using the variational characterization of the governing equations, and introducing a Lagrange multiplier to enforce the constraint on the given volume of phase 1, yields

$$O = \sup_{\chi \in \mathcal{X}} \inf_{u \in \mathcal{V}} \left\{ L(u, \chi) = \int_{\Omega} \frac{1}{2} \sum_{i=1,2} k_i |\nabla u_i|^2 + \frac{1}{2} \chi (1 - \chi) u \cdot Au - \lambda \chi \, dx \right\}. \quad (\text{P})$$

6.4 Characterization of the optimal design problem

Saddle point theorem

We begin by showing that we can exchange the order of finding the supremum and infimum in the saddle point problem (P).

Theorem 6.4.1. *There exists $\bar{v} \in \mathcal{V}$, $\bar{\chi} \in \mathcal{X}$ such that*

$$L(\bar{v}, \bar{\chi}) = \sup_{\chi \in \mathcal{X}} \inf_{v \in \mathcal{V}} L(v, \chi) = \inf_{v \in \mathcal{V}} \sup_{\chi \in \mathcal{X}} L(v, \chi).$$

for the saddle point problem (P).

The proof of this draws from the following theorem adapted from Ekeland and Témam [148].

Theorem 6.4.2 (Proposition 2.4 of [148]). *Suppose two reflexive Banach spaces V and Z satisfy*

- (i) $\mathcal{A} \subset V$ is convex, closed and non-empty,
- (ii) $\mathcal{B} \subset Z$ is convex, closed and non-empty.

Further let the function $L : \mathcal{A} \times \mathcal{B} \mapsto \mathbb{R}$ satisfy

- (iii) $\forall u \in \mathcal{A}$, $p \rightarrow L(u, p)$ is concave and upper semicontinuous,
- (iv) $\forall p \in \mathcal{B}$, $u \rightarrow L(u, p)$ is convex and lower semicontinuous,
- (v) *there exists $p_0 \in \mathcal{B}$ for \mathcal{B} bounded such that*

$$\lim_{\substack{u \in \mathcal{A} \\ \|u\| \rightarrow \infty}} L(u, p_0) = +\infty.$$

Then L possesses at least one saddle point on $\mathcal{A} \times \mathcal{B}$.

We apply this theorem with L as in problem (P), $V = W^{1,2}(\Omega; \mathbb{R}^2)$, $Z = L^2(\Omega; [0, 1])$, $\mathcal{A} = \mathcal{V}$ and $\mathcal{B} = \mathcal{X}$. Clearly, V and Z are reflexive Banach spaces as required by the theorem above. We now show that these satisfy the rest of hypothesis (H).

Proposition 6.4.3. *Both \mathcal{X} and \mathcal{V} are convex, closed, and non-empty.*

Proof. The point of concern is showing that our space \mathcal{X} is in fact closed. So consider a sequence $\chi_i \in \mathcal{X}$ such that $\chi_i \rightarrow \chi$ in L^2 . We seek to show that the limit function $\chi \in \mathcal{X}$. From the definition of \mathcal{X} , $\|\chi_i\|_{L^\infty} \leq 1$. Thus, we can pick a subsequence χ_{i_k} of χ_i such that $\chi_{i_k} \xrightarrow{*} \bar{\chi}$, in L^∞ as $k \rightarrow \infty$. It follows $\chi_{i_k} \rightarrow \bar{\chi}$, in L^2 as $k \rightarrow \infty$. Therefore, $\chi = \bar{\chi}$ and $\text{ess sup } \chi \leq 1$. Similarly we can show $\text{ess inf } \chi \geq 0$. Thus, $\chi \in \mathcal{X}$ and \mathcal{X} is closed. \square

Proposition 6.4.4. *For each $\chi \in \mathcal{X}$, $v \mapsto L(v, \chi)$ is convex and lower semicontinuous.*

Proof. This follows trivially from the fact that the integrand in L is a sum of a positive definite quadratic term in ∇u_i and a positive semidefinite quadratic form in u . \square

Proposition 6.4.5. *For each $v \in \mathcal{V}$, $\chi \mapsto L(v, \chi)$ is concave and upper semicontinuous.*

Proof. This follows trivially from the fact that the integrand in L is a sum of a negative definite quadratic term and two linear terms in χ . \square

Proof of Theorem 6.4.1. From the aforementioned propositions, we have satisfied requirements (i) – (iv) of the theorem. To show (v), set $\chi(x) = 1/2$. We have

$$\begin{aligned} L(u, 0.5) &= \int_{\Omega} \left(\frac{1}{2} \sum_{i=1,2} \bar{k}_i |\nabla u_i|^2 + \frac{1}{8} u \cdot Au - \frac{1}{2} \lambda \right) dx \\ &\geq \int_{\Omega} \left(\frac{1}{2} \sum_{i=1,2} \bar{k}_i |\nabla u_i|^2 - \frac{1}{2} \lambda \right) dx \\ &\geq c_1 \|\nabla u\|_{L^2} - c_2 \geq c_3 \|u\|_{H^1} - c_2 \end{aligned}$$

for suitable positive constants c_i , where we use the derived form of Poincaré's inequality in the final step. The requirement (v) follows. \square

Explicit characterization

We are now ready to obtain the explicit characterization of the optimal design problem (P).

Theorem 6.4.6. *We have*

$$O = \min_{v \in \mathcal{V}} \int_{\Omega} \overline{W}(v, \nabla v) dx.$$

where

$$\overline{W}(v, \xi) = \begin{cases} \frac{1}{2} (|\xi_1|^2 k_{21} + |\xi_2|^2 k_{22}) & (v, \xi) \in \mathcal{R}_0, \\ \frac{(\sum_i \Delta k_i |\xi_i|^2)^2 + 2 \sum_i |\xi_i|^2 (k_v (k_{i1} + k_{i2}) - 2\lambda \Delta k_i) + (k_v - 2\lambda)^2}{8k_v} & (v, \xi) \in \mathcal{R}, \\ \frac{1}{2} (|\xi_1|^2 k_{11} + |\xi_2|^2 k_{12} - 2\lambda) & (v, \xi) \in \mathcal{R}_1 \end{cases}$$

with

$$\mathcal{R}_0 = \{(v, \xi) : \sum_i \Delta k_i |\xi_i|^2 - 2\lambda \leq -k_v\},$$

$$\mathcal{R} = \{(v, \xi) : -k_v < \sum_i \Delta k_i |\xi_i|^2 - 2\lambda < k_v\},$$

$$\mathcal{R}_1 = \{(v, \xi) : \sum_i \Delta k_i |\xi_i|^2 - 2\lambda \geq k_v\},$$

and

$$\Delta k_i = k_{i1} - k_{i2}, \quad k_v = k_s (v_1 - v_2)^2.$$

The function \overline{W} is shown in Figure 6.2 as a function of ξ for a fixed v with various parameters. The shaded regions indicate the gradients for which mixed phases ($\chi \in (0, 1)$) occur. Note that mixed phases occur where the gradients of both species are comparable in magnitude, and pure phases occur otherwise.

Proof. For $v \in \mathbb{R}^2$, $\xi \in \mathbb{R}^{2 \times 2}$, $\chi \in \mathbb{R}$, set

$$W(v, \xi, \chi) = \frac{1}{2} \sum_{i=1,2} (\chi k_{i1} + (1 - \chi) k_{i2}) |\xi_i|^2 + \frac{k_s}{2} \chi (1 - \chi) v \cdot Av - \lambda \chi$$

and

$$\overline{W}(v, \xi) = \max_{\chi \in [0,1]} W(v, \xi, \chi). \quad (6.9)$$

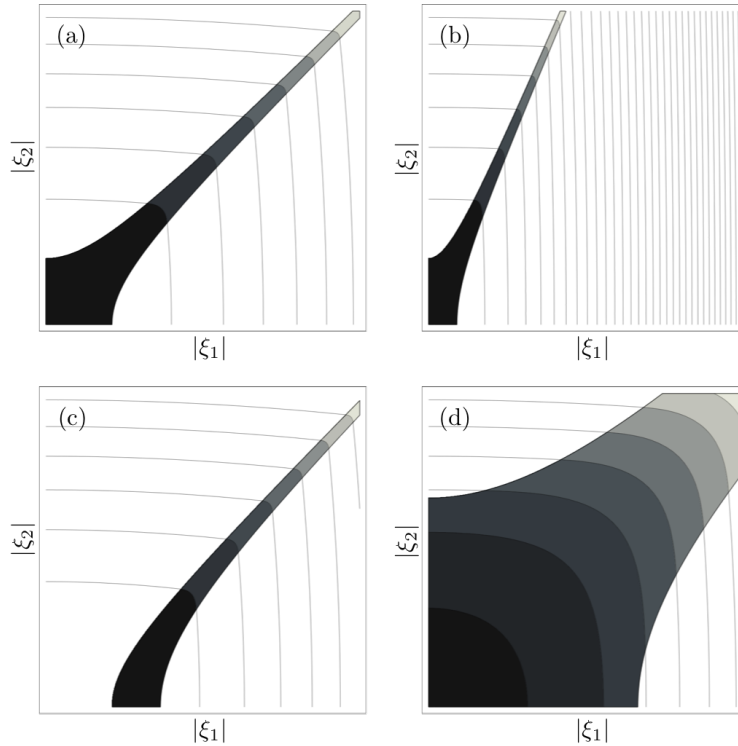


Figure 6.2: Contour plot of \overline{W} for fixed v, λ . The shaded regions indicate where mixed phase ($\chi \in (0, 1)$) occurs. (a) $k_{11} = k_{22} = k_s = 1, k_{12} = k_{21} = 0.1, (v_1 - v_2)^2 = 1, \lambda = 0$. (b) Parameters as in (a) except $k_{11} = 5$, (c) Parameters as in (a) except $\lambda = 1$, (d) Parameters as in (a) except $(v_1 - v_2)^2 = 10$.

In light of the saddle point theorem,

$$O = \inf_{v \in \mathcal{V}} \sup_{\chi \in \mathcal{X}} \int_{\Omega} W(v, \nabla v, \chi) dx = \inf_{v \in \mathcal{V}} \int_{\Omega} \overline{W}(v, \nabla v) dx.$$

It remains to compute \overline{W} . To that end, note that for a fixed v, ξ , $W(v, \xi, \chi)$ is quadratic in χ and

$$\frac{\partial W}{\partial \chi}(v, \xi, \chi) = 0$$

has an unique solution $\chi = \chi^*$. A simple calculation reveals

$$\chi^*(v, \xi) = \frac{\sum_i \Delta k_i |\xi_i|^2 + k_s (v_1 - v_2)^2 - 2\lambda}{2k_s (v_1 - v_2)^2}.$$

Notice that

$$\chi^*(v, \xi) \begin{cases} \leq 0 & (v, \xi) \in \mathcal{R}_0, \\ \in (0, 1) & (v, \xi) \in \mathcal{R}, \\ \geq 1 & (v, \xi) \in \mathcal{R}_1. \end{cases}$$

A longer, but straightforward, calculation reveals that

$$W(v, \xi, \chi^*) = \frac{\left(\sum_i \Delta k_i |\xi_i|^2\right)^2 + 2 \sum_i (|\xi_i|^2 k_v (k_{i1} + k_{i2}) - 2\lambda \Delta k_i) + (k_v - 2\lambda)^2}{8k_v}.$$

Similarly,

$$\begin{aligned} W(v, \xi, 0) &= \frac{1}{2} \left(|\xi_1|^2 k_{21} + |\xi_2|^2 k_{22} \right), \\ W(v, \xi, 1) &= \frac{1}{2} \left(|\xi_1|^2 k_{11} + |\xi_2|^2 k_{12} - 2\lambda \right). \end{aligned}$$

Now, we can verify by explicit calculation that

$$\begin{aligned} W(v, \xi, \chi^*) - W(v, \xi, 0) &= \frac{k_v}{2} (\chi^*(v, \xi))^2 \\ W(v, \xi, \chi^*) - W(v, \xi, 1) &= \frac{1}{4} (\chi^*(v, \xi) - 1)^2 \\ W(v, \xi, 1) - W(v, \xi, 0) &= \frac{1}{2} \left(\sum_i \Delta k_i |\xi_i|^2 - 2\lambda \right) \end{aligned} \tag{6.10}$$

We obtain the desired result by recalling (6.9), rewriting

$$\overline{W}(v, \xi) = \max\{\Psi(v, \xi)W(v, \xi, \chi^*), W(v, \xi, 0), W(v, \xi, 1)\}$$

where

$$\Psi(v, \xi) = \begin{cases} 1 & (v, \xi) \in \mathcal{R} \\ -\infty & \text{else} \end{cases}$$

and using (6.10). □

6.5 Phase-field formulation of the optimal design problem

The min-max problem based on the functional L is difficult to solve numerically due to the fact that χ is only in L^2 and because of the constraint $\chi \in [0, 1]$. The relaxed functional is also difficult to solve numerically since \overline{W} is not strictly convex. Therefore, we now pursue an alternative approach to the optimal design problem

that is amenable to numerical treatment. We regularize the functional $L(u, \chi)$ by adding the L^2 norm of $\nabla \chi$ and requiring $\chi \in H^1$. We also replace the constraint $\chi \in [0, 1]$ with a penalty. Finally, from a practical point of view, it would also be beneficial to have solutions that prefer the pure phases $\chi \in \{0, 1\}$. Therefore, we add a term to the energy that penalizes any deviation from this set.

We consider the functional

$$\mathcal{L}(u, \chi) = \int_{\Omega} \left(\frac{1}{2} \sum_{i=1,2} k_i |\nabla u_i|^2 + \frac{1}{2} \chi(1 - \chi) u \cdot Au - \lambda \chi - (\alpha W(\chi) + \beta |\nabla \chi|^2) \right) dx, \quad (6.11)$$

where

$$W(\chi) = \chi^2(1 - \chi)^2,$$

has two wells at $\chi \in \{0, 1\}$.

The additional terms in parenthesis form the integrand of the Allen-Cahn functional [121]. Minimizers of this functional partition the domain into regions where $\chi \approx 0$ and $\chi \approx 1$ separated by transition layers with thickness $\sim \sqrt{\beta/\alpha}$. In our setting, we expect this to be modified by the transport energy.

We seek to find the saddle point by considering a gradient flow:

$$\begin{aligned} \int_{\Omega} \frac{\partial \chi}{\partial t} \varphi \, dx &= \frac{1}{d_{\chi}} \langle \delta_{\chi}, \varphi \rangle \\ \int_{\Omega} \frac{\partial u}{\partial t} \psi \, dx &= -\frac{1}{d_u} \langle \delta_u, \psi \rangle \end{aligned}$$

for every $\varphi, \psi \in H^1(\Omega; \mathbb{R}^N)$ subject to the appropriate boundary conditions where $\langle \cdot, \cdot \rangle$ denotes the L^2 inner product and $d_{\chi}, d_u > 0$ are the inverse mobilities. We obtain the following system of equations:

$$d_{\chi} \frac{\partial \chi}{\partial t} = \sum_{i=1,2} \frac{k'_i}{2} |\nabla u_i|^2 + \frac{1}{2} u \cdot Au(1 - 2\chi) - \lambda + \beta \nabla^2 \chi - \alpha W'(\chi), \quad (6.12)$$

$$d_u \frac{\partial u_i}{\partial t} = \nabla \cdot k_i \nabla u_i - \chi(1 - \chi) A_{ij} u_j. \quad (6.13)$$

6.6 Numerical study of the optimal design problem

We have implemented the phase field formulation of the optimal design problem (6.12, 6.13) using the commercial software COMSOL [149]. All our simulations are in two dimensions ($n = 2$). We work with non-dimensional units where the size of the domain, the concentration at a boundary and the (diagonal components of the)

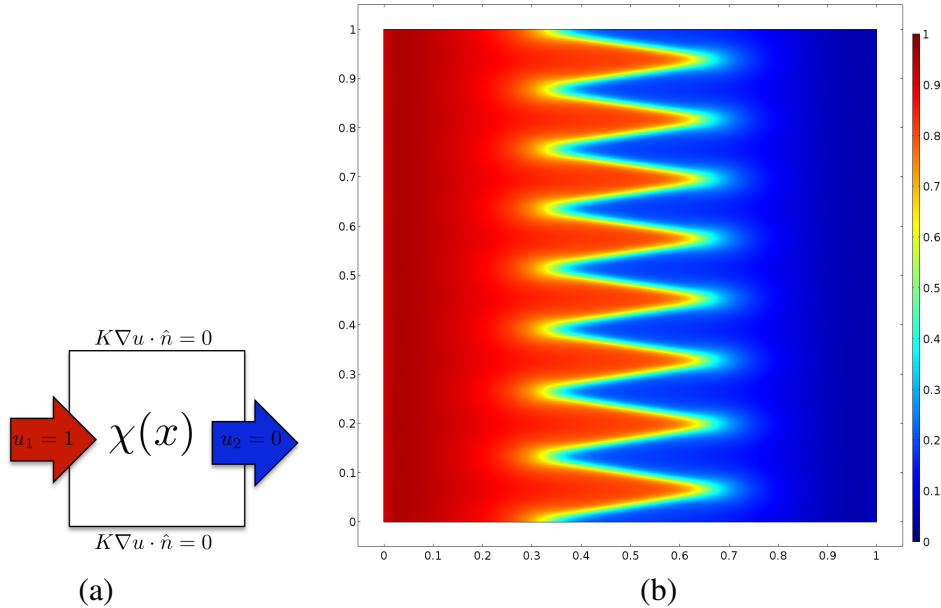


Figure 6.3: (a) Square reactor with a source of species 1 on the left and a sink of species 2 on the right. (b) Optimal design (χ) for the parameters in (6.14).

diffusion coefficient are $\mathcal{O}(1)$. We discretize the problem spatially using linear finite elements generated by Delaunay triangulation, and integrate the resulting ordinary differential equation in time by using the backward differentiation formula. We impose the volume constraint as a global constraint that is built into COMSOL. Additionally, we impose a point-wise constraint restricting $\chi \in [0, 1]$. We typically begin with an initial guess of uniform χ , and run the simulations until an apparent steady state is reached (i.e., when the right hand sides of (6.12, 6.13) become small compared to a given tolerance). The simulations can get stuck in local optima, but we try to avoid this by doing parameter sweeps and studying additional initial conditions.

Square reactor

We begin with a square domain, $\Omega = (0, 1)^2$, shown in Figure 6.3(a). We prescribe $u_1 = 1$ on the left face $\partial_1\Omega = \{0\} \times (0, 1)$ corresponding to a source of species 1, $u_2 = 0$ on the right face $\partial_2\Omega = \{1\} \times (0, 1)$ corresponding to a sink of species 2, and zero-flux boundary conditions otherwise. We also impose a zero flux boundary condition on our phase-field variable χ .

The resulting optimal design χ is shown in Figure 6.3(b) for the parameters

$$\begin{aligned} k_{11} = k_{22} = 1, k_{12} = k_{21} = 1 \times 10^{-6}, k_s = 1 \times 10^2, \\ \alpha = 1, \beta = 2 \times 10^{-5}, d_\chi = 2 \times 10^{-2}, d_u = 2 \times 10^{-3}, \\ v = 0.5. \end{aligned} \quad (6.14)$$

This simulation had a mesh with 67068 elements, took 50 non-dimensional units of time over 845 time steps and the L^2 norm of the time derivative of χ is 3.945×10^{-4} at the end of the simulation. We have verified that the design does not change by refining the mesh and driving the L^2 norm of the time derivative of χ to 10^{-12} .

The resulting design has a clear intuitive explanation. Given the boundary conditions, the design seeks to draw in species 1 from the left, react it in the center to convert species 1 to species 2, and expel species 2 at the right. Therefore, the design puts material 1, which has a high diffusivity of species 1, on the left so that it can easily transport species 1 from the source to the interface where the reaction consumes it. Material 2, which has a high diffusivity of species 2, is placed on the right so that it can easily transport species 2 from the interface, where the reaction generates it, to the sink. The design maximizes the reaction by creating a zig-zag interface between the two materials.

We now begin a parameter study for the same problem. Figure 6.4 shows the resulting designs for a volume fraction $v = 0.5$ for various diffusivities k_{11}, k_{22} . Figures 6.5 and 6.6 show the corresponding concentration fields u_1 and u_2 respectively while Figure 6.7 shows the corresponding reactions.

We begin at the center for the case $k_{11} = k_{22} = 1$, which is what we described earlier. Decreasing both diffusivities by moving up on the diagonal to $k_{11} = k_{22} = 0.1$ leads to a similar segregation of the material but the interface is sharper and straight. On the other hand, increasing both diffusivities by moving down the diagonal to $k_{11} = k_{22} = 10$ still segregates the material, but in a very diffuse manner with an almost constant gradient. Note that the interface width changes despite the fact that length-scale, $\sqrt{\beta/\alpha}$, predicted by the phase-field alone is held fixed. This is because of the relative importance of the diffusion and the reaction. When the diffusivities are both small, $k_{11} = k_{22} = 0.1$ as in the upper-left, the reaction is relatively easy and diffusion difficult. Thus one only needs a narrow region for the reaction, saving much of the pure material for optimal transport. Conversely, when the diffusivities are both large, $k_{11} = k_{22} = 10$ as in the bottom-right, the reaction is relatively

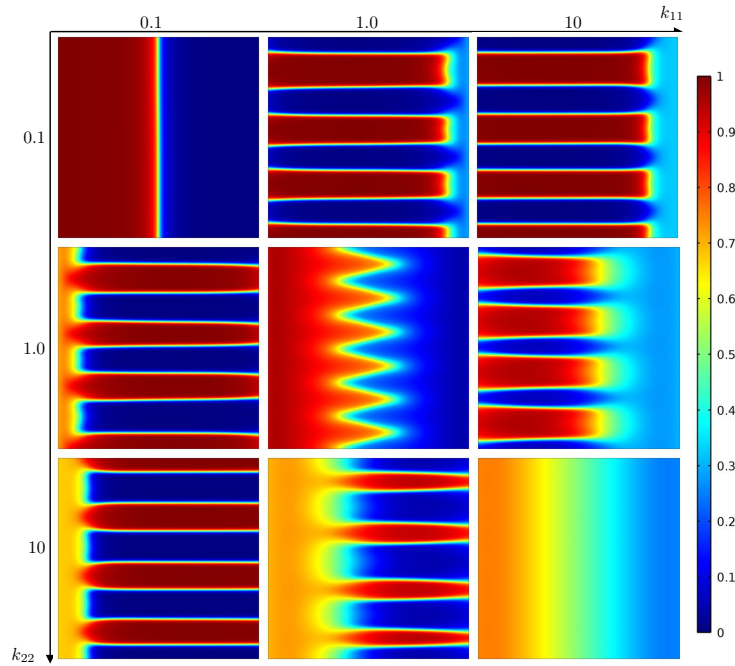


Figure 6.4: Designs with volume fraction $\nu = 0.5$ as we vary diffusion coefficients with $\alpha = 0.1$, $\beta = 5 \times 10^{-5}$, $k_{12} = 10^{-3} \times k_{11}$, $k_{21} = 10^{-3} \times k_{22}$, $d_\chi = 1 \times 10^{-2} - 1.5 \times 10^{-2}$, $d_u = 7 \times 10^{-4} - 1 \times 10^{-3}$, $k_s = 1 \times 10^2$.

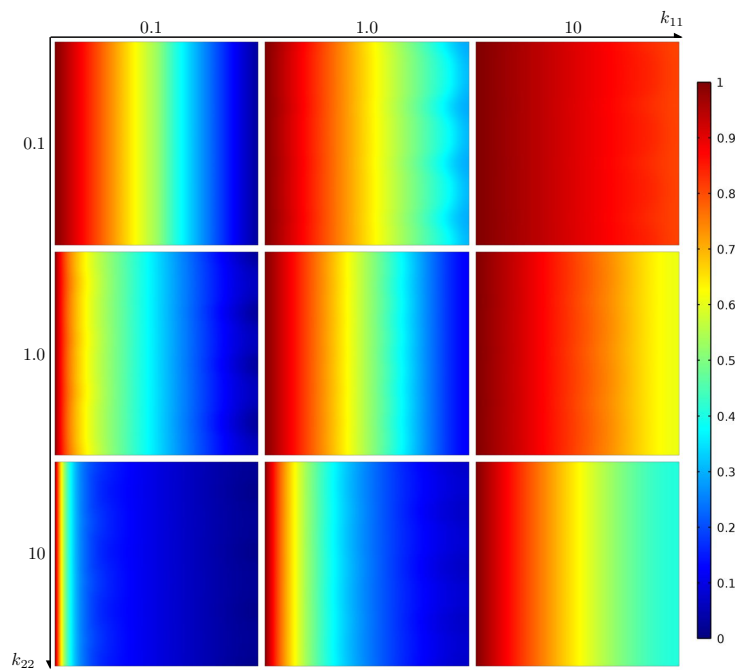


Figure 6.5: Concentration field u_1 associated with the designs presented in Figure 6.4.

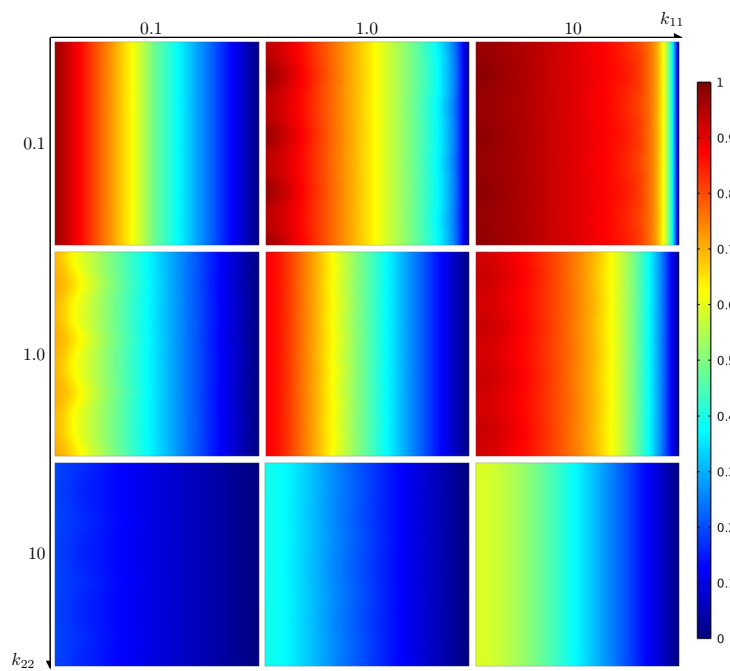


Figure 6.6: Concentration field u_2 associated with the designs presented in Figure 6.4.

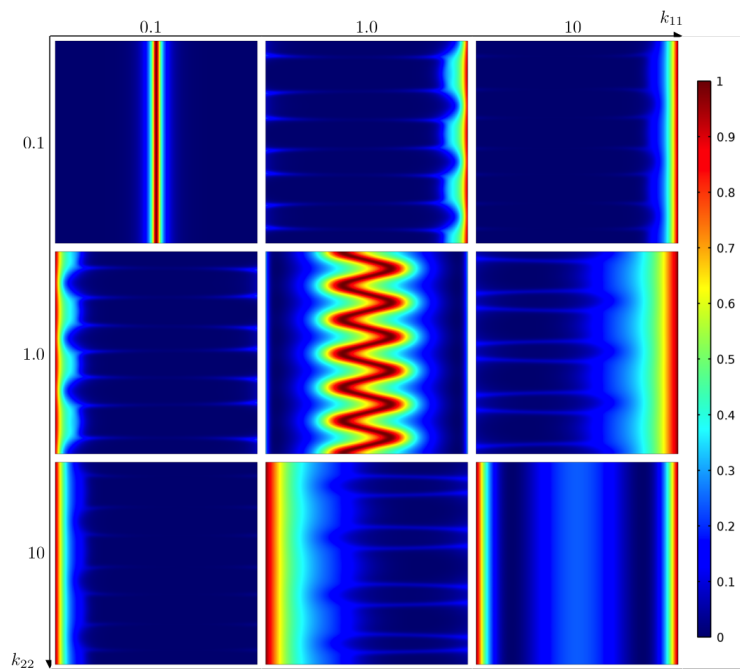


Figure 6.7: Distribution of reaction zones associated with the designs presented in Figure 6.4; normalized units.

Table 6.1: Contributions to the energy functional $L(u, \chi)$, the phase field regularization, the flux J_i of each species calculated at the boundary, and the reaction (right hand side of Eq. (6.1)₁) integrated on the domain for $\nu = 0.5$.

k_{11}	k_{22}	Transport Energy $\int \frac{1}{2} \sum k_i \nabla u_i ^2$	Reaction Energy $\int \frac{1}{2} \chi(1 - \chi) u \cdot Au$	Phase Field	$J_{1,\text{in}}$ $\int k_1 \nabla u_1 \cdot \hat{n}$	$J_{2,\text{out}}$ $-\int k_2 \nabla u_2 \cdot \hat{n}$	Reaction
0.1	0.1	0.0451	0.0023	0.0203	0.0948	0.0948	0.0949
0.1	1	0.1706	0.0285	0.0748	0.3866	0.3977	0.3983
0.1	10	0.2952	0.2022	0.0779	0.9610	0.9947	0.9948
1	0.1	0.1706	0.0285	0.0550	0.3977	0.3864	0.3983
1	1	0.4276	0.0340	0.1070	0.9202	0.9201	0.9232
1	10	0.9044	0.3595	0.1502	2.5015	2.5256	2.5278
10	0.1	0.2953	0.2021	0.0574	0.9946	0.9602	0.9947
10	1	0.9044	0.3596	0.1150	2.5257	2.5011	2.5278
10	10	2.2730	0.9990	0.1699	6.5257	6.5254	6.5440

difficult and diffusion easy. Thus, one creates a very diffuse interface to optimize the reaction.

We now turn to the situation when the diffusivities are different. Consider the case when $k_{11} = 1, k_{22} = 0.1$ as shown on the top-center. The diffusion of species 1 is considerably easier than that of species 2. Therefore, it is advantageous to have the reaction close to the sink. Species 1 is transported by the long arms of material 1 (red) which protrude from the left to the right where it reacts very close to the sink, thereby reducing the distance that species 2 has to be transported. The excess material 2 (blue) is ‘hidden’ on the left in arms that do not participate in the transport. The case $k_{11} = 10, k_{22} = 0.1$ shown on the top-right is similar with a slightly wider interface since reaction is more difficult compared to the transport. The case $k_{11} = 10, k_{22} = 1$ shown on the right-middle is also similar except the interfacial region is even wider. The cases $k_{11} = 0.1, k_{22} = 1$; $k_{11} = 0.1, k_{22} = 10$ and $k_{11} = 1, k_{22} = 10$ are the analogous, with the roles of material 1 and 2 reversed.

The phase-field functional, the domain, and the boundary conditions have a symmetry, and we examine if the resulting designs reflect this symmetry. Specifically, note that if $\{u_1, u_2, \chi\}$ is a solution for a problem with k_1, k_2 on the square domain, then $\{1 - u_2, 1 - u_1, 1 - \chi\}$ is a solution for a problem with k_2, k_1 on the square domain obtained by changing x to $1 - x$. We see that our designs reflect this symmetry. Specifically, compare the case $k_{11} = 0.1, k_{22} = 1$ and the resulting design χ_1 shown in middle-left of Figure 6.4 and the case $k_{11} = 1, k_{22} = 0.1$ and the resulting design χ_2 shown in top-center of Figure 6.4. We see that $\chi_1(x, y) \approx 1 - \chi_2(1 - x, 1 - y)$.

Table 6.1 shows how the different contributions to the energy change for the various cases. It also shows how the flux varies. Further, it shows the the flux at the source,

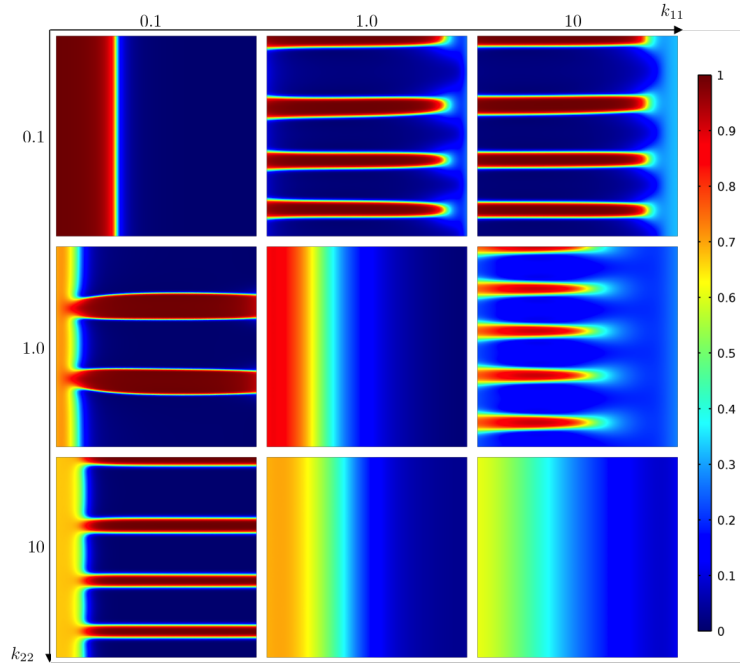


Figure 6.8: Parameter sweep with $\nu = 0.3$, $\alpha = 0.1$, $\beta = 5 \times 10^{-5}$, $k_{12} = 10^{-3} \times k_{11}$, $k_{21} = 10^{-3} \times k_{22}$, $d_\chi = 1 \times 10^{-2} - 2 \times 10^{-1}$, $d_u = 7 \times 10^{-4} - 2 \times 10^{-2}$, $k_s = 1 \times 10^2$.

sink, and reaction zone all agree.

Figure 6.8 shows the designs for the same parameters, but for a volume fraction $\nu = 0.3$. The designs are similar, except the interface is more to the left.

Cylindrical reactor

Many reactors designed for thermochemical conversion devices implement a cylindrical ceramic structure that allow for even heating and easy transport of reactant gas. Thus, for the second example we look at an annular structure where the inner edge with $r = 0.2$ is held as the source of the first chemical species ($\partial_1 \Omega$ where $u_1 = 1$) and the outer at $r = 1$ is set as a sink for the second ($\partial_2 \Omega$ where $u_2 = 0$). We consider the same parameters as (6.14). The resulting design is shown in Figure 6.9(b). The first species enters from the inside, reacts and converts to the second species which exits from the outside. Thus, we see much of the first material on the inside and the second on the outside. Further, to enable sufficient reaction, the interface region is graded. If we decrease the phase field coefficients by an order of magnitude, we obtain the design in Figure 6.9(a) where the mixed region increases as the penalty for deviating from the pure materials is reduced. On the other hand, increasing the phase field coefficients by an order of magnitude yields the design in

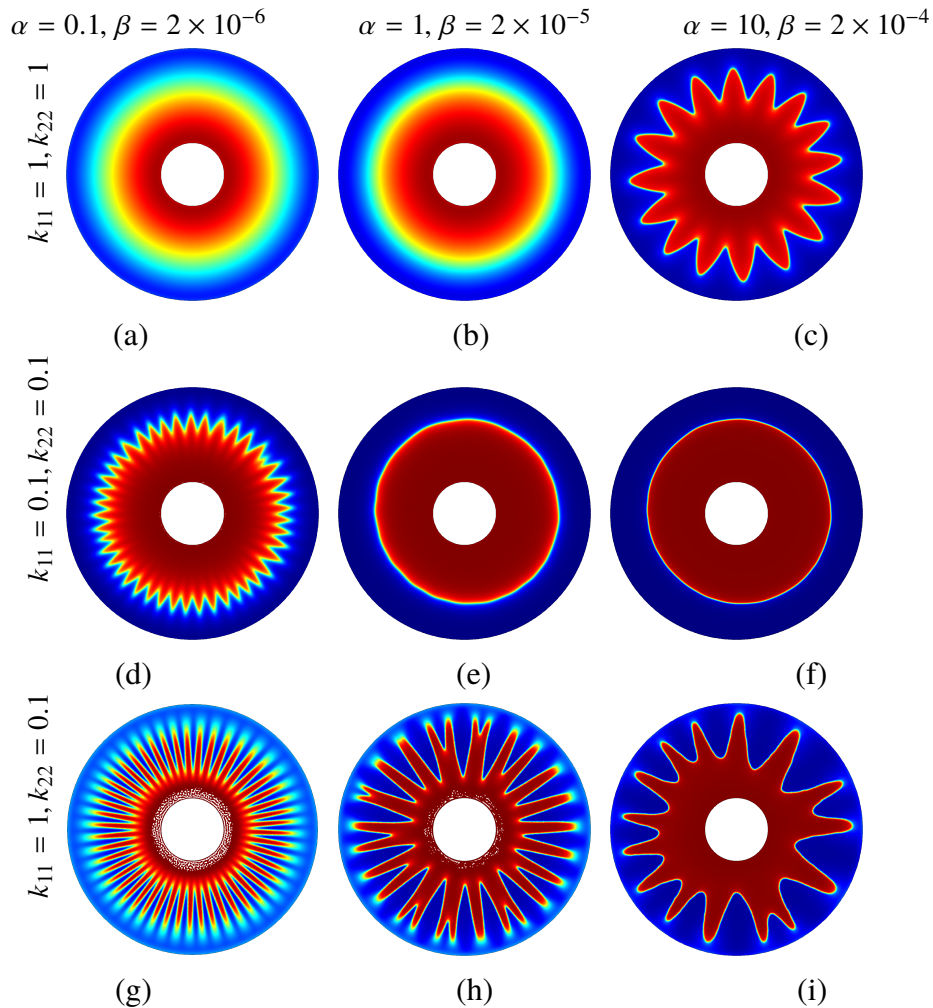


Figure 6.9: Designs for a cylindrical reactor with a source of the first species at the inner edge and a sink for the second species at the outer edge. The parameters are in (6.14) except as noted in the rows and columns of the figure. Further, $k_{12} = 10^{-2} \times k_{11}$, $k_{21} = 10^{-2} \times k_{22}$.

Figure 6.9(c). Indeed, here, the penalty for deviation from the pure phases increases and therefore the interface becomes corrugated allowing sufficient reaction.

The second row of Figure 6.9 show the analogous result when the diffusivity is reduced by an order of magnitude. Transport is now harder compared to the reaction, and therefore nearly pure phases dominate to ensure transport and complex interfaces are avoided due to the phase field. Again, increasing the phase field parameters promotes pure phases. The final row of Figure 6.9 show the results for unequal conductivity. Since the transport of first species is easier, material 1 forms long arms to transport the first species to close to the outlet where the reaction takes. Further, increasing the phase field parameters promotes pure phases and leads to

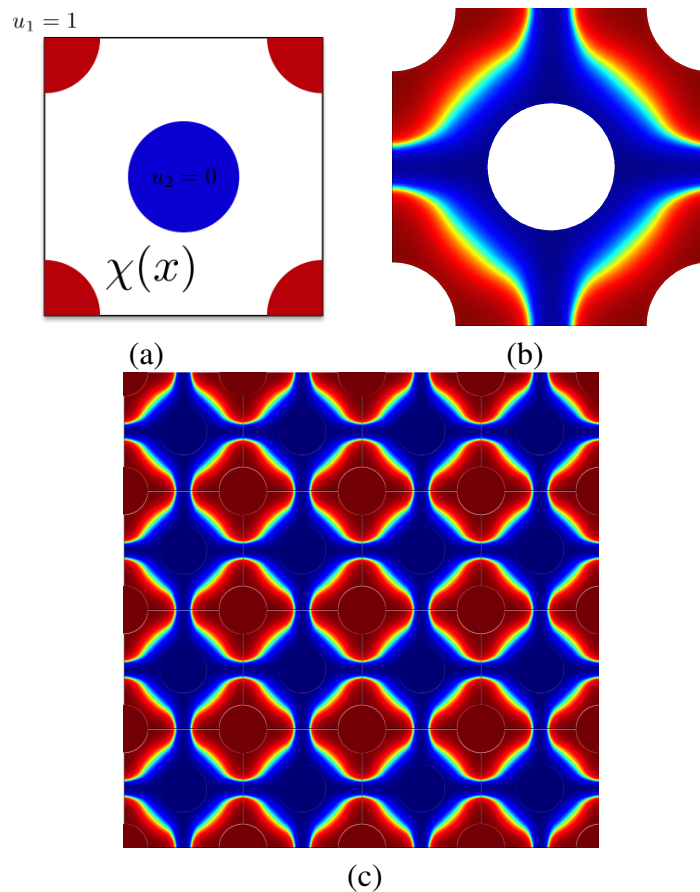


Figure 6.10: Periodic square distribution of circular sources and sinks. (a) Unit domain, (b) Resulting design on the unit domain, (c) Periodic design.

fewer arms.

Periodic cellular reactor

It is common to construct reactors as a periodic tubular array where the first species enter the reactor through one set of tubes while the second species is extracted from the reactor with a different set of tubes. Looking at a cross-section, one sees a square array of inlets and a square array of outlets. This motivates our next example where the reactor is taken to be periodic with the unit cell shown in Figure 6.10(a). The source is at the corners of the cell while the outlet is at the center. We look for a periodic design to optimize the transport as before. The resulting unit design for the parameters shown in (6.14) is shown in Figure 6.10(b). It is repeated periodically in Figure 6.10(c).

Chapter 7

CONCLUSIONS

The art of structure is where to put
the holes

Robert le Ricolais

Through this work, we have examined problems motivated by metal oxides used in solar-driven thermochemical conversion devices. We focused on exploring the link between microstructural material design and efficiency in energy conversion. Our goal was to develop a framework for designing materials that is not specific to one application, but instead can be modified to optimize any energy conversion device.

The mixed ionic and electronic transport behavior of ceria for its application in thermochemical conversion was derived from the continuum mechanics standpoint. This was achieved by considering a mixed conductor exposed to an externally-applied electric potential in an oxygen environment with mechanical constraints using various balance laws and constitutive equations. Local thermodynamic potentials, transport laws, and associated boundary conditions capture the coupling between the chemical, electrical, thermal, and mechanical environments of the material. Accordingly, we obtain a system of partial differential equations describing ambipolar diffusion (or the diffusion-drift equation) that are consistent with those used in experimental literature under certain specific constitutive relations. The extension of this model to numerical implementation would allow for time-dependent behavior of mixed conductors to be analyzed in the multi-physics setting, and for reconstructed microstructures.

The applicability of strain-engineering as a way to improve the behavior of thermochemical conversion devices was then explored. The chemical expansivity observed with varying degrees of reduction of mixed conductors was exploited to increase the amount of vacancies at equilibrium. By formulating the problem as a thin film of ceria onto an inert substrate with a thermal mismatch, we find that equilibrium of the system yields an implicit relationship between temperature, oxygen environment, and non-stoichiometry in the film that is shifted from stress-free experimental data because of the strain accommodation. Alternate geometries could be considered

and optimized for different applications. Instead of assuming an idealized thin-film problem, both the equilibrium relation derived here and the time-dependent behavior described in the previous chapter could be adapted to a finite element or finite difference scheme to examine the kinetic behavior in an arbitrary material configuration.

In continuing towards optimal microstructure of mixed conductors in energy conversion devices, we examine the pairing between microscale behavior and the volume-averaged behavior when the pore scale is very small. We considered two-phase transport through a porous mixed conductor using a coupled system of fluid flow via Stokes-flow, convective-diffusion in the gas phase, and diffusion in the bulk phase. At the interface between the two phases, we prescribe a non-linear exchange term and then a linearized flux condition like those obtained in Ch. 3. By varying the scaling (strength) of the interface reaction with respect to the other transport properties and the unit cell size, we obtain different effective regimes. Most notably, we obtain an intuitive volume-averaged system consisting of Darcy's law for the homogenized Stokes-flow independent of a system of coupled transport describing the gaseous species and solid species. We obtain an averaged convective-diffusion with reaction describing the averaged species previously residing in the pore space, and a separate reactive-diffusion field associated with the species residing in the solid phase. The interfacial exchange is shifted to becoming a body-source/sink that is dependent on the amount of interface in the unit cells. Additionally, the averaged fluid velocity and diffusivity are dependent on the pore-scale solutions to the original transport models.

The main goal of this project was examining numerical methods of designing optimal microstructures for energy conversion. We used a coupled, two-phase, reactive-diffusion system describing the transport of two chemical species each residing in separate phases (pore space and solid), and undergoing an interfacial conversion reaction. We relax this problem to one allowing intermediate densities, such that we obtain an equation form similar to the homogenized behavior derived in Ch. 5, where we restrict the chemistry to areas of intermediate density. The resulting system is formulated variationally and analyzed. We found that the optimal design problem associated with maximizing the through-put through a device (or cell structure) can be formulated as a saddle-point problem. Implementing the relaxation requirement indicates that in most configurations, designs with large areas of composite regions are preferred. We then investigate the optimal design

problem numerically using a phase field method, where these intermediate densities are penalized to ensure manufacturability and an inherent length scale. Optimal interface shapes are dependent on transport parameters, but in general, saw-tooth or branched structures are obtained. These optimal structures effectively yield designs with arbitrary length scales, and could be coupled well with additive manufacturing techniques to be experimentally verified.

7.1 Future work

With advances in battery structures spanning a variety of length-scales, similar optimal design questions can be investigated. Anode, cathode, and overall battery architecture directly impact the charge/discharge ability and storage capacity of batteries and can be improved with novel design. Additionally, new structures that accommodate the volume change associated with intercalation-deintercalation of lithium can be explored using optimal design using models describing the chemical expansivity. Extending these models, especially those developed in Ch. 3 and combining with optimal design would be an interesting extension of these methods. Similar optimization possibilities are seen in fuel cells, separation membranes, or any system requiring a balance of interfacial measure and bulk transport in optimizing material behavior.

The methods and models described here are far from optimal and complete. The continuum mechanics presented in Ch. 3 could be verified using experimental data, and transient studies using reconstructed microstructures would be of interest in the experimental community. Additional considerations including radiative heat transfer and a more thorough examination of entropy would benefit the rigor of the model and could potentially elucidate new multi-physics coupling. Application to other classes of mixed-conductors would be fairly straight-forward given the necessary thermodynamic and kinetic data for validation. The strain engineering presented could be easily combined with the optimization to explore new geometries to maximize the strain-effect. Through the homogenization under different convective scalings, more advanced methods are required to fully describe the effective behavior. Coupling the solutions obtained with bounds on conductivity and reactivity from the composites community would be of interest. Finally, the optimization method presented was chosen because of its simplicity, and many techniques could be developed or adapted to improve the implementation and computational cost. Examining interface-tracking methods and three-dimension topology optimization would be natural extensions to the general framework presented here. Finally, cou-

pling with advances is directed synthesis and additive manufacturing for realization of these optimal designs would be the ideal conclusion to this work.

BIBLIOGRAPHY

- [1] Nathan S Lewis and Daniel G Nocera. “Powering the planet: Chemical challenges in solar energy utilization”. In: *Proceedings of the National Academy of Sciences* 103.43 (2006), pp. 15729–15735.
- [2] Greg P Smestad and Aldo Steinfeld. “Review: Photochemical and thermochemical production of solar fuels from H₂O and CO₂ using metal oxide catalysts”. In: *Industrial & Engineering Chemistry Research* 51.37 (2012), pp. 11828–11840.
- [3] James R. Wilson et al. “Three-dimensional reconstruction of a solid-oxide fuel-cell anode”. In: *Nat Mater* 5.7 (July 2006), pp. 541–544.
- [4] Grant A. Umeda et al. “Inverse opal ceria-zirconia: architectural engineering for heterogeneous catalysis”. In: *Energy Environ. Sci.* 1 (4 2008), pp. 484–486.
- [5] WooChul Jung et al. “High electrode activity of nanostructured, columnar ceria films for solid oxide fuel cells”. In: *Energy Environ. Sci.* 5 (9 2012), pp. 8682–8689.
- [6] Zhenhai Wen et al. “In situ growth of mesoporous SnO₂ on multiwalled carbon nanotubes: A novel composite with porous-tube structure as anode for lithium batteries”. In: *Advanced Functional Materials* 17.15 (2007), pp. 2772–2778.
- [7] Yu Li, Zheng-Yi Fu, and Bao-Lian Su. “Hierarchically structured porous materials for energy conversion and storage”. In: *Advanced Functional Materials* 22.22 (2012), pp. 4634–4667.
- [8] Neelima Mahato et al. “Progress in material selection for solid oxide fuel cell technology: A review”. In: *Progress in Materials Science* 72 (2015), pp. 141–337.
- [9] Stuart B Adler. “Factors governing oxygen reduction in solid oxide fuel cell cathodes”. In: *Chemical reviews* 104.10 (2004), pp. 4791–4844.
- [10] JG Swallow et al. “Chemomechanics of ionically conductive ceramics for electrical energy conversion and storage”. In: *Journal of Electroceramics* 32.1 (2014), pp. 3–27.
- [11] Jeffrey Hanna et al. “Fundamentals of electro-and thermochemistry in the anode of solid-oxide fuel cells with hydrocarbon and syngas fuels”. In: *Progress in Energy and Combustion Science* 40 (2014), pp. 74–111.
- [12] Yu Liu, Moses Tade, and Zongping Shao. “Electrolyte Materials for Solid Oxide Fuel Cells (SOFCs)”. In: *Solid Oxide Fuel Cells*. 2013, pp. 26–55.

- [13] JR Smith et al. "Evaluation of the relationship between cathode microstructure and electrochemical behavior for SOFCs". In: *Solid State Ionics* 180.1 (2009), pp. 90–98.
- [14] James R. Wilson et al. "Effect of composition of $(\text{La}_{0.8}\text{Sr}_{0.2}\text{MnO}_3\text{-Y}_2\text{O}_3\text{-stabilized ZrO}_2)$ cathodes: Correlating three-dimensional microstructure and polarization resistance". In: *Journal of Power Sources* 195.7 (2010), pp. 1829–1840.
- [15] A. Atkinson et al. "Advanced anodes for high-temperature fuel cells". In: *Nat Mater* 3.1 (Jan. 2004), pp. 17–27.
- [16] Toshio Suzuki et al. "Impact of anode microstructure on solid oxide fuel cells". In: *Science* 325.5942 (2009), pp. 852–855.
- [17] J Scott Cronin, James R Wilson, and Scott A Barnett. "Impact of pore microstructure evolution on polarization resistance of Ni-Yttria-stabilized zirconia fuel cell anodes". In: *Journal of Power Sources* 196.5 (2011), pp. 2640–2643.
- [18] Ryan MC Clemmer and Stephen Francis Corbin. "Influence of porous composite microstructure on the processing and properties of solid oxide fuel cell anodes". In: *Solid State Ionics* 166.3 (2004), pp. 251–259.
- [19] David E Stephenson et al. "Modeling 3D microstructure and ion transport in porous Li-ion battery electrodes". In: *Journal of The Electrochemical Society* 158.7 (2011), A781–A789.
- [20] Y-H Chen et al. "Porous cathode optimization for lithium cells: Ionic and electronic conductivity, capacity, and selection of materials". In: *Journal of Power Sources* 195.9 (2010), pp. 2851–2862.
- [21] Peter G Bruce, Bruno Scrosati, and Jean-Marie Tarascon. "Nanomaterials for rechargeable lithium batteries". In: *Angewandte Chemie International Edition* 47.16 (2008), pp. 2930–2946.
- [22] Francesco Ciucci and Wei Lai. "Derivation of micro/macro lithium battery models from homogenization". In: *Transport in porous media* 88.2 (2011), pp. 249–270.
- [23] Y-S Hu et al. "Synthesis of hierarchically porous carbon monoliths with highly ordered microstructure and their application in rechargeable lithium batteries with high-rate capability". In: *Advanced Functional Materials* 17.12 (2007), pp. 1873–1878.
- [24] Haiping Jia et al. "Novel Three-Dimensional Mesoporous Silicon for High Power Lithium-Ion Battery Anode Material". In: *Advanced Energy Materials* 1.6 (2011), pp. 1036–1039.
- [25] Naoki Nitta et al. "Li-ion battery materials: present and future". In: *Materials today* 18.5 (2015), pp. 252–264.

- [26] Antonino Salvatore Arico et al. “Nanostructured materials for advanced energy conversion and storage devices”. In: *Nature materials* 4.5 (2005), pp. 366–377.
- [27] Subrahmanyam Goriparti et al. “Review on recent progress of nanostructured anode materials for Li-ion batteries”. In: *Journal of Power Sources* 257 (2014), pp. 421–443.
- [28] Hong Huang et al. “High-performance ultrathin solid oxide fuel cells for low-temperature operation”. In: *Journal of the Electrochemical Society* 154.1 (2007), B20–B24.
- [29] GX Wang et al. “Nanostructured Si–C composite anodes for lithium-ion batteries”. In: *Electrochemistry Communications* 6.7 (2004), pp. 689–692.
- [30] Simon Ackermann et al. “Reticulated porous ceria undergoing thermochemical reduction with high-flux irradiation”. In: *International Journal of Heat and Mass Transfer* 107 (2017), pp. 439–449.
- [31] Hagedorn Yves-Christian et al. “Net shaped high performance oxide ceramic parts by selective laser melting”. In: *Physics Procedia* 5 (2010), pp. 587–594.
- [32] Loïc Baggetto, Dmitry Danilov, and Peter HL Notten. “Honeycomb-Structured Silicon: Remarkable Morphological Changes Induced by Electrochemical (De) Lithiation”. In: *Advanced Materials* 23.13 (2011), pp. 1563–1566.
- [33] Jos FM Oudenhoven, Loïc Baggetto, and Peter HL Notten. “All-Solid-State Lithium-Ion Microbatteries: A Review of Various Three-Dimensional Concepts”. In: *Advanced Energy Materials* 1.1 (2011), pp. 10–33.
- [34] William C. Chueh et al. “High-Flux Solar-Driven Thermochemical Dissociation of CO₂ and H₂O Using Nonstoichiometric Ceria”. In: *Science* 330.6012 (2010), pp. 1797–1801.
- [35] William C. Chueh and Sossina M. Haile. “A thermochemical study of ceria: exploiting an old material for new modes of energy conversion and CO₂ mitigation”. In: *Philosophical Transactions of the Royal Society of London A: Mathematical, Physical and Engineering Sciences* 368.1923 (2010), pp. 3269–3294.
- [36] Aldo Steinfeld. “Solar thermochemical production of hydrogen—a review”. In: *Solar energy* 78.5 (2005), pp. 603–615.
- [37] Somnath C Roy et al. “Toward solar fuels: photocatalytic conversion of carbon dioxide to hydrocarbons”. In: *Acs Nano* 4.3 (2010), pp. 1259–1278.
- [38] H.J.M. Bouwmeester and A.J. Burggraaf. “Chapter 10 Dense ceramic membranes for oxygen separation”. In: *Fundamentals of Inorganic Membrane Science and Technology*. Ed. by A.J. Burggraaf and L. Cot. Vol. 4. Membrane Science and Technology. Elsevier, 1996, pp. 435–528.

- [39] M. H. Hecht, J. A. Hoffman, and Moxie Team. “The Mars Oxygen ISRU Experiment (MOXIE) on the Mars 2020 Rover”. In: *Lunar and Planetary Science Conference*. Vol. 46. Lunar and Planetary Science Conference. Mar. 2015, p. 2774.
- [40] J Sunarso et al. “Mixed ionic–electronic conducting (MIEC) ceramic-based membranes for oxygen separation”. In: *Journal of Membrane Science* 320.1 (2008), pp. 13–41.
- [41] Dario Marrocchelli et al. “Understanding Chemical Expansion in Non-Stoichiometric Oxides: Ceria and Zirconia Case Studies”. In: *Advanced Functional Materials* 22.9 (2012), pp. 1958–1965.
- [42] E Perry Murray, T Tsai, and SA Barnett. “A direct-methane fuel cell with a ceria-based anode”. In: *Nature* 400.6745 (1999), pp. 649–651.
- [43] Piotr Jasinski, Toshio Suzuki, and Harlan U Anderson. “Nanocrystalline undoped ceria oxygen sensor”. In: *Sensors and Actuators B: Chemical* 95.1 (2003), pp. 73–77.
- [44] Luke J. Venstrom et al. “The Effects of Morphology on the Oxidation of Ceria by Water and Carbon Dioxide”. In: *Journal of Solar Energy Engineering* 134.1 (Nov. 2011), pp. 011005–011005.
- [45] Stéphane Abanades and Gilles Flamant. “Thermochemical hydrogen production from a two-step solar-driven water-splitting cycle based on cerium oxides”. In: *Solar Energy* 80.12 (2006), pp. 1611–1623.
- [46] William C Chueh. *Electrochemical & Thermochemical Behavior of Cerium (IV) Oxide delta*. California Institute of Technology, 2011.
- [47] Anastasia Stamatiou, Peter G Loutzenhiser, and Aldo Steinfeld. “Syngas production from H₂O and CO₂ over Zn particles in a packed-bed reactor”. In: *AIChE Journal* 58.2 (2012), pp. 625–631.
- [48] R.J. Panlener, R.N. Blumenthal, and J.E. Garnier. “A thermodynamic study of nonstoichiometric cerium dioxide”. In: *Journal of Physics and Chemistry of Solids* 36.11 (1975), pp. 1213–1222.
- [49] M Ricken, J Nölting, and I Riess. “Specific heat and phase diagram of nonstoichiometric ceria (CeO_{2-x})”. In: *Journal of Solid State Chemistry* 54.1 (1984), pp. 89–99.
- [50] Chirranjeevi Balaji Gopal and Sossina M. Haile. “An electrical conductivity relaxation study of oxygen transport in samarium doped ceria”. In: *J. Mater. Chem. A* 2 (7 2014), pp. 2405–2417.
- [51] J.A. Lane and J.A. Kilner. “Measuring oxygen diffusion and oxygen surface exchange by conductivity relaxation”. In: *Solid State Ionics* 136-137 (2000). Proceedings of the 12th International Conference on Solid State Ionics, pp. 997–1001.

- [52] Wei Lai and Sossina M Haile. “Impedance spectroscopy as a tool for chemical and electrochemical analysis of mixed conductors: a case study of ceria”. In: *Journal of the American Ceramic Society* 88.11 (2005), pp. 2979–2997.
- [53] Philipp Furler et al. “Thermochemical CO₂ splitting via redox cycling of ceria reticulated foam structures with dual-scale porosities”. In: *Physical Chemistry Chemical Physics* 16.22 (2014), pp. 10503–10511.
- [54] Liang-Shu Zhong et al. “3D flowerlike ceria micro/nanocomposite structure and its application for water treatment and CO removal”. In: *Chemistry of Materials* 19.7 (2007), pp. 1648–1655.
- [55] James R Wilson and Scott A Barnett. “Solid oxide fuel cell Ni–YSZ anodes: effect of composition on microstructure and performance”. In: *Electrochemical and Solid-State Letters* 11.10 (2008), B181–B185.
- [56] Carl Wagner. “Equations for transport in solid oxides and sulfides of transition metals”. In: *Progress in solid state chemistry* 10 (1975), pp. 3–16.
- [57] Chirranjeevi Balaji Gopal. “Ab-Initio and Experimental Techniques for Studying Non-Stoichiometry and Oxygen Transport in Mixed Conducting Oxides”. PhD thesis. California Institute of Technology, 2015.
- [58] Yong Jiang et al. “Theoretical study of environmental dependence of oxygen vacancy formation in CeO₂”. In: *Applied Physics Letters* 87.14 (2005), p. 141917.
- [59] Bernard D. Coleman and Walter Noll. “The Thermodynamics of Elastic Materials with Heat Conduction and Viscosity”. In: *The Foundations of Mechanics and Thermodynamics: Selected Papers*. Berlin, Heidelberg: Springer Berlin Heidelberg, 1974, pp. 145–156.
- [60] Sophia Haussener and Aldo Steinfeld. “Effective heat and mass transport properties of anisotropic porous ceria for solar thermochemical fuel generation”. In: *Materials* 5.1 (2012), pp. 192–209.
- [61] Sophia Haussener et al. “Tomography-based heat and mass transfer characterization of reticulate porous ceramics for high-temperature processing”. In: *Journal of Heat Transfer* 132.2 (2010), p. 023305.
- [62] Sophia Haussener et al. “Tomography-based determination of effective transport properties for reacting porous media”. In: *Journal of Heat Transfer* 134.1 (2012), p. 012601.
- [63] Silvan Suter, Aldo Steinfeld, and Sophia Haussener. “Pore-level engineering of macroporous media for increased performance of solar-driven thermochemical fuel processing”. In: *International Journal of Heat and Mass Transfer* 78 (2014), pp. 688–698.
- [64] Silvan Suter and Sophia Haussener. “Morphology Engineering of porous media for enhanced solar fuel and power production”. In: *Jom* 65.12 (2013), pp. 1702–1709.

- [65] Stephen Whitaker. *The method of volume averaging*. Vol. 13. Springer Science & Business Media, 2013.
- [66] Stuart B. Adler. “Chemical Expansivity of Electrochemical Ceramics”. In: *Journal of the American Ceramic Society* 84.9 (2001), pp. 2117–2119.
- [67] Keith L. Duncan et al. “The role of point defects in the physical properties of nonstoichiometric ceria”. In: *Journal of Applied Physics* 101.4, 044906 (2007).
- [68] S.R. Bishop, K.L. Duncan, and E.D. Wachsman. “Defect equilibria and chemical expansion in non-stoichiometric undoped and gadolinium-doped cerium oxide”. In: *Electrochimica Acta* 54.5 (2009), pp. 1436–1443.
- [69] Sean R Bishop et al. “Chemical expansion of nonstoichiometric $\text{Pr}_{0.1}\text{Ce}_{0.9}\text{O}_{2-\delta}$: correlation with defect equilibrium model”. In: *Journal of the European Ceramic Society* 31.13 (2011), pp. 2351–2356.
- [70] FC Larché and JW Cahn. “A linear theory of thermochemical equilibrium of solids under stress”. In: *Acta Metallurgica* 21.8 (1973), pp. 1051–1063.
- [71] FC Larché and JW Cahn. “Thermochemical equilibrium of multiphase solids under stress”. In: *Acta Metallurgica* 26.10 (1978), pp. 1579–1589.
- [72] FC Larché and JW Cahn. “The effect of self-stress on diffusion in solids”. In: *Acta Metallurgica* 30.10 (1982), pp. 1835–1845.
- [73] FC Larché and JW Cahn. “The interactions of composition and stress in crystalline solids”. In: *J. Res. Natl. Bur. Stand.* 89.6 (1984), pp. 467–500.
- [74] R Krishnamurthy and BW Sheldon. “Stresses due to oxygen potential gradients in non-stoichiometric oxides”. In: *Acta Materialia* 52.7 (2004), pp. 1807–1822.
- [75] A Atkinson. “Chemically-induced stresses in gadolinium-doped ceria solid oxide fuel cell electrolytes”. In: *Solid State Ionics* 95.3-4 (1997), pp. 249–258.
- [76] A Atkinson and TMGM Ramos. “Chemically-induced stresses in ceramic oxygen ion-conducting membranes”. In: *Solid State Ionics* 129.1 (2000), pp. 259–269.
- [77] Bilge Yildiz. ““Stretching” the energy landscape of oxides: Effects on electrocatalysis and diffusion”. In: *MRS Bulletin* 39 (02 Feb. 2014), pp. 147–156.
- [78] William C Johnson and Hermann Schmalzried. “Phenomenological thermodynamic treatment of elastically stressed ionic crystals”. In: *Journal of the American Ceramic Society* 76.7 (1993), pp. 1713–1719.
- [79] William C Johnson. “Thermodynamic Equilibria in Two-Phase, Elastically Stressed Ionic Crystals”. In: *Journal of the American Ceramic Society* 77.6 (1994), pp. 1581–1591.

- [80] Jennifer LM Rupp et al. “Scalable Oxygen-Ion Transport Kinetics in Metal-Oxide Films: Impact of Thermally Induced Lattice Compaction in Acceptor Doped Ceria Films”. In: *Advanced Functional Materials* 24.11 (2014), pp. 1562–1574.
- [81] *Abstracts from the Workshop on Homogenization and Effective Moduli of Materials and Media*. IMA Preprints Series. Institute for Mathematics and Its Applications. 1984.
- [82] A. Braides. *Γ -convergence for Beginners*. Oxford lecture series in mathematics and its applications. Oxford University Press, 2002.
- [83] Gianni Dal Maso. *An introduction to Γ -convergence*. Vol. 8. Springer Science & Business Media, 2012.
- [84] Ole Sigmund and Salvatore Torquato. “Design of materials with extreme thermal expansion using a three-phase topology optimization method”. In: *Journal of the Mechanics and Physics of Solids* 45.6 (1997), pp. 1037–1067.
- [85] LV Gibiansky and S Torquato. “Thermal expansion of isotropic multiphase composites and polycrystals”. In: *Journal of the Mechanics and Physics of Solids* 45.7 (1997), pp. 1223–1252.
- [86] Martin Philip Bendsøe and Noboru Kikuchi. “Generating optimal topologies in structural design using a homogenization method”. In: *Computer methods in applied mechanics and engineering* 71.2 (1988), pp. 197–224.
- [87] Joseph B Keller. “Darcy’s law for flow in porous media and the two-space method”. In: *Nonlinear partial differential equations in engineering and applied science (Proc. Conf., Univ. Rhode Island, Kingston, RI, 1979)*. Vol. 54. Dekker New York. 1980, pp. 429–443.
- [88] Enrique Sanchez-Palencia and André Zaoui. “Homogenization techniques for composite media”. In: *Homogenization Techniques for Composite Media*. Vol. 272. 1987.
- [89] Grégoire Allaire. “Homogenization and two-scale convergence”. In: *SIAM Journal on Mathematical Analysis* 23.6 (1992), pp. 1482–1518.
- [90] Luc Tartar. *The general theory of homogenization: a personalized introduction*. Vol. 7. Springer Science & Business Media, 2009.
- [91] Alain Bensoussan, Jacques-Louis Lions, and George Papanicolaou. *Asymptotic analysis for periodic structures*. Vol. 5. North-Holland Publishing Company Amsterdam, 1978.
- [92] Nikolai Sergeevich Bakhvalov and G Panasenko. *Homogenisation: averaging processes in periodic media: mathematical problems in the mechanics of composite materials*. Vol. 36. Springer Science & Business Media, 2012.
- [93] François Murat and Luc Tartar. “H-convergence”. In: *Topics in the mathematical modelling of composite materials*. Springer, 1997, pp. 21–43.

- [94] Luc Tartar. “The compensated compactness method applied to systems of conservation laws”. In: *Systems of nonlinear partial differential equations*. Springer, 1983, pp. 263–285.
- [95] OA Oleinik and VV Zhikov. “On the homogenization of elliptic operators with almost-periodic coefficients”. In: *Milan Journal of Mathematics* 52.1 (1982), pp. 149–166.
- [96] Graeme W Milton. “The theory of composites”. In: *The Theory of Composites*, by Graeme W. Milton, pp. 748. ISBN 0521781256. Cambridge, UK: Cambridge University Press, May 2002. (2002), p. 748.
- [97] Andrej Cherkaev. *Variational methods for structural optimization*. Vol. 140. Springer Science & Business Media, 2012.
- [98] Ulrich Hornung and Willi Jäger. “Diffusion, convection, adsorption, and reaction of chemicals in porous media”. In: *Journal of differential equations* 92.2 (1991), pp. 199–225.
- [99] Gregori A Chechkin, Andrei L Piatnitski, and Aleksei S Shamev. *Homogenization: methods and applications*. Vol. 234. American Mathematical Soc., 2007.
- [100] Grégoire Allaire and Andrey Piatnitski. “Homogenization of nonlinear reaction-diffusion equation with a large reaction term”. In: *Annali dell Università di Ferrara* 56.1 (2010), pp. 141–161.
- [101] Grégoire Allaire and Harsha Hutridurga. “Homogenization of reactive flows in porous media and competition between bulk and surface diffusion”. In: *IMA Journal of Applied Mathematics* 77.6 (2012), pp. 788–815.
- [102] Grégoire Allaire and Anne-Lise Raphael. “Homogenization of a convection–diffusion model with reaction in a porous medium”. In: *Comptes Rendus Mathématique* 344.8 (2007), pp. 523–528.
- [103] Jean-Louis Auriault and Horia I Ene. “Macroscopic modelling of heat transfer in composites with interfacial thermal barrier”. In: *International journal of heat and mass transfer* 37.18 (1994), pp. 2885–2892.
- [104] Patrizia Donato and Kim Hang Le Nguyen. “Homogenization of diffusion problems with a nonlinear interfacial resistance”. In: *Nonlinear Differential Equations and Applications NoDEA* 22.5 (2015), pp. 1345–1380.
- [105] R Lipton and DRS Talbot. “Bounds for the effective conductivity of a composite with an imperfect interface”. In: *Proceedings of the Royal Society of London A: Mathematical, Physical and Engineering Sciences*. Vol. 457. 2010. The Royal Society. 2001, pp. 1501–1517.
- [106] Horia I Ene and Dan Polišeovski. “Model of diffusion in partially fissured media”. In: *Zeitschrift für angewandte Mathematik und Physik ZAMP* 53.6 (2002), pp. 1052–1059.

- [107] Robert Lipton. “Heat conduction in fine scale mixtures with interfacial contact resistance”. In: *SIAM Journal on Applied Mathematics* 58.1 (1998), pp. 55–72.
- [108] M.P. Bendsoe and O. Sigmund. *Topology Optimization: Theory, Methods, and Applications*. Engineering online library. Springer Berlin Heidelberg, 2003.
- [109] G. Allaire. *Shape Optimization by the Homogenization Method*. Applied Mathematical Sciences. Springer New York, 2001.
- [110] J Goodman, R V Kohn, and L Reyna. “Numerical Study of a Relaxed Variational Problem from Optimal Design”. In: *Comput. Methods Appl. Mech. Eng.* 57.1 (Aug. 1986), pp. 107–127.
- [111] Robert V. Kohn and Gilbert Strang. “Optimal design and relaxation of variational problems, I”. In: *Communications on Pure and Applied Mathematics* 39.1 (1986), pp. 113–137.
- [112] Luigi Ambrosio and Giuseppe Buttazzo. “An optimal design problem with perimeter penalization”. In: *Calculus of Variations and Partial Differential Equations* 1.1 (1993), pp. 55–69.
- [113] Blaise Bourdin and Antonin Chambolle. “Design-dependent loads in topology optimization”. In: *ESAIM: Control, Optimisation and Calculus of Variations* 9 (Aug. 2003), pp. 19–48.
- [114] Robert V Kohn and Gilbert Strang. “Optimal design and relaxation of variational problems, II”. In: *Communications on Pure and Applied Mathematics* 39.2 (1986), pp. 139–182.
- [115] Robert V Kohn and Gilbert Strang. “Optimal design and relaxation of variational problems, III”. In: *Communications on Pure and Applied Mathematics* 39.3 (1986), pp. 353–377.
- [116] P. M. Bendsøe and O. Sigmund. “Material interpolation schemes in topology optimization”. In: *Archive of Applied Mechanics* 69.9 (1999), pp. 635–654.
- [117] James A Sethian and Andreas Wiegmann. “Structural boundary design via level set and immersed interface methods”. In: *Journal of computational physics* 163.2 (2000), pp. 489–528.
- [118] Grégoire Allaire, François Jouve, and Anca-Maria Toader. “Structural optimization using sensitivity analysis and a level-set method”. In: *Journal of computational physics* 194.1 (2004), pp. 363–393.
- [119] Stanley J Osher and Fadil Santosa. “Level set methods for optimization problems involving geometry and constraints: I. frequencies of a two-density inhomogeneous drum”. In: *Journal of Computational Physics* 171.1 (2001), pp. 272–288.

- [120] John W Cahn and John E Hilliard. “Free energy of a nonuniform system. I. Interfacial free energy”. In: *The Journal of chemical physics* 28.2 (1958), pp. 258–267.
- [121] Samuel M Allen and John W Cahn. “A microscopic theory for antiphase boundary motion and its application to antiphase domain coarsening”. In: *Acta Metallurgica* 27.6 (1979), pp. 1085–1095.
- [122] Ryo Kobayashi. “Modeling and numerical simulations of dendritic crystal growth”. In: *Physica D: Nonlinear Phenomena* 63.3-4 (1993), pp. 410–423.
- [123] IS Aranson, VA Kalatsky, and VM Vinokur. “Continuum field description of crack propagation”. In: *Physical review letters* 85.1 (2000), p. 118.
- [124] Long-Qing Chen. “Phase-field models for microstructure evolution”. In: *Annual review of materials research* 32.1 (2002), pp. 113–140.
- [125] Blaise Bourdin and Antonin Chambolle. “The phase-field method in optimal design”. In: *IUTAM Symposium on Topological Design Optimization of Structures, Machines and Materials*. Springer. 2006, pp. 207–215.
- [126] Mathias Wallin, Matti Ristinmaa, and Henrik Askfelt. “Optimal Topologies Derived from a Phase-field Method”. In: *Struct. Multidiscip. Optim.* 45.2 (Feb. 2012), pp. 171–183.
- [127] Akihiro Takezawa, Shinji Nishiwaki, and Mitsuru Kitamura. “Shape and topology optimization based on the phase field method and sensitivity analysis”. In: *Journal of Computational Physics* 229.7 (2010), pp. 2697–2718.
- [128] Bing-Chung Chen and Noboru Kikuchi. “Topology optimization with design-dependent loads”. In: *Finite Elements in Analysis and Design* 37.1 (2001), pp. 57–70.
- [129] Allan Gersborg-Hansen, Martin P Bendsøe, and Ole Sigmund. “Topology optimization of heat conduction problems using the finite volume method”. In: *Structural and multidisciplinary optimization* 31.4 (2006), pp. 251–259.
- [130] Eduardo Alberto and Ole Sigmund. “Topology optimization of multiple physics problems modeled by Poisson’s equation”. In: *Latin American Journal of Solids and Structures* 1.2 (2004), pp. 169–184.
- [131] Seung-Hyun Ha and Seonho Cho. “Topological shape optimization of heat conduction problems using level set approach”. In: *Numerical Heat Transfer, Part B: Fundamentals* 48.1 (2005), pp. 67–88.
- [132] Tyler E Bruns. “Topology optimization of convection-dominated, steady-state heat transfer problems”. In: *International Journal of Heat and Mass Transfer* 50.15 (2007), pp. 2859–2873.
- [133] Thomas Borrvall and Joakim Petersson. “Topology optimization of fluids in Stokes flow”. In: *International journal for numerical methods in fluids* 41.1 (2003), pp. 77–107.

- [134] Fridolin Okkels and Henrik Bruus. “Design of micro-fluidic bio-reactors using topology optimization”. In: *Journal of Computational and Theoretical Nanoscience* 4.4 (2007), pp. 814–816.
- [135] Fridolin Okkels and Henrik Bruus. “Scaling behavior of optimally structured catalytic microfluidic reactors”. In: *Physical Review E* 75.1 (2007), p. 016301.
- [136] Daniel Schäpper et al. “Topology optimized microbioreactors”. In: *Biotechnology and bioengineering* 108.4 (2011), pp. 786–796.
- [137] Mikhail Osanov and James K Guest. “Topology Optimization for Architected Materials Design”. In: *Annual Review of Materials Research* 46 (2016), pp. 211–233.
- [138] Phanish Suryanarayana and Kaushik Bhattacharya. “Evolution of polarization and space charges in semiconducting ferroelectrics”. In: *Journal of Applied Physics* 111.3, 034109 (2012).
- [139] Mogens Mogensen, Nigel M Sammes, and Geoff A Tompsett. “Physical, chemical and electrochemical properties of pure and doped ceria”. In: *Solid State Ionics* 129.1 (2000), pp. 63–94.
- [140] SR Bishop et al. “Chemical expansion: implications for electrochemical energy storage and conversion devices”. In: *Annual Review of Materials Research* 44 (2014), pp. 205–239.
- [141] Hideko Hayashi et al. “Thermal expansion of Gd-doped ceria and reduced ceria”. In: *Solid State Ionics* 132.3 (2000), pp. 227–233.
- [142] Mogens Mogensen et al. “Physical properties of mixed conductor solid oxide fuel cell anodes of doped CeO₂”. In: *Journal of the Electrochemical Society* 141.8 (1994), pp. 2122–2128.
- [143] Malte A Peter and Michael Böhm. “Different choices of scaling in homogenization of diffusion and interfacial exchange in a porous medium”. In: *Mathematical Methods in the Applied Sciences* 31.11 (2008), pp. 1257–1282.
- [144] S Torquato and G Stell. “Microstructure of two-phase random media. IV. Expected surface area of a dispersion of penetrable spheres and its characteristic function”. In: *The Journal of chemical physics* 80.2 (1984), pp. 878–880.
- [145] Grégoire Allaire and Zakaria Habibi. “Homogenization of a conductive, convective, and radiative heat transfer problem in a heterogeneous domain”. In: *SIAM Journal on Mathematical Analysis* 45.3 (2013), pp. 1136–1178.
- [146] Malte A Peter and Michael Böhm. “Different choices of scaling in homogenization of diffusion and interfacial exchange in a porous medium”. In: *Mathematical Methods in the Applied Sciences* 31.11 (2008), pp. 1257–1282.

- [147] L.C. Evans. *Partial Differential Equations*. Graduate studies in mathematics. American Mathematical Society, 2010.
- [148] I. Ekeland and R. Témam. *Convex Analysis and Variational Problems*. Society for Industrial and Applied Mathematics, 1999.
- [149] Comsol. *Multiphysics Reference Guide for COMSOL 5.1*. 2015.

A p p e n d i x A

A Γ -CONVERGENCE RESULT

In this appendix, we wish to rationalize the transition from phase-field formulation of the optimal design problem (6.11) to the original optimal design problem (P) in Chapter 6. The optimal design problem using the phase-field model is written

$$\begin{aligned} & \sup_{\chi \in \mathcal{X}^2} \left\{ \inf_{v \in \mathcal{V}} L(v, \chi) - \int_{\Omega} W_{\epsilon}(\chi) + \epsilon^2 |\nabla \chi|^2 dx \right\}, \\ & := \sup_{\chi \in \mathcal{X}^2} \{J(\chi) - H_{\epsilon}(\chi)\}. \end{aligned}$$

Instead of the normal two-well chemical potential, we use one that depends on our prescribed length scale, ϵ :

$$W_{\epsilon}(\chi) = \begin{cases} \frac{1}{\epsilon^2} \chi^2 (1 - \chi)^2 & \text{if } \chi \notin [0, 1] \\ \epsilon^2 \chi^2 (1 - \chi)^2 & \text{if } \chi \in [0, 1]. \end{cases}$$

In the sense of Γ -convergence, we want to make sure that we obtain our original, unaltered, optimal design problem when we force the interface penalty to 0. We enforce the scaling on our two-well energy to rationalize taking this limit; instead of looking at a sharp-interface limit, where a consideration along the lines of Modica-Mortola would be more relevant. The scaling we choose effectively forces the relaxation of the two-well energy in the limit in question.

As a reminder, we define Γ -convergence in the supremum setting directly from Braides [82].

Definition A.0.1 (Γ -limit for supremum problems). *We say that a sequence $f_j : X \rightarrow \mathbb{R}$ Γ^+ -converges w.r.t to the weak L^2 convergence in X to $f : X \rightarrow \mathbb{R}$ if for all $x \in X$, we have*

1. (*lim sup inequality*) for every every sequence (x_j) converging weakly in L^2 to x

$$f(x) \geq \limsup_j f_j(x_j);$$

2. (lim inf inequality) there exists a sequence (x_j) converging weakly in L^2 to x such that

$$f(x) \leq \liminf_j f_j(x_j);$$

Considering the behavior of the typical phase-transition problem, we will eventually be interested in the relaxation of our functional. Since we are maximizing our objective function over the design space, we are after the upper semicontinuous envelope for the through-put that we are concerned with.

Definition A.0.2 (Relaxed functional). (Adapted from Jöst) Let X satisfy the first axiom of countability. Then \bar{F} is the relaxed⁺ function for $F : X \rightarrow \bar{\mathbb{R}}$ iff the following two conditions are satisfied:

1. whenever $x_n \rightarrow x$

$$\bar{F}(x) \geq \limsup_{n \rightarrow \infty} F(x_n),$$

2. for every $x \in X$, there exists a sequence $x_n \rightarrow x$ with

$$\bar{F}(x) \leq \lim_{n \rightarrow \infty} F(x_n).$$

Additionally, we have that

$$\bar{F}(x) = \sup \{ \limsup F(x_n) : x_n \rightarrow x \in X \},$$

satisfies both of these requirements.

Theorem A.0.3. We let $\Omega \in \mathbb{R}^2$ be a rectangular domain and without loss of generality we'll define $\Omega = (0, 1) \times (0, 1)$. We define the optimal design problem as the functional

$$F_\epsilon(\chi) = \begin{cases} J(\chi) - H_\epsilon(\chi) & \text{if } \chi \in \mathcal{X}^2 \text{ and } \frac{1}{|\Omega|} \int_\Omega \chi = v \\ -\infty & \text{otherwise.} \end{cases}$$

The Γ^+ -limit of $F_\epsilon(\chi)$ as $\epsilon \rightarrow 0$ with respect to the weak L^2 convergence is

$$F(\chi) = \begin{cases} \bar{J}(\chi) & \text{if } \chi \in \mathcal{X}^2 \text{ and } \frac{1}{|\Omega|} \int_\Omega \chi = v \\ -\infty & \text{otherwise.} \end{cases}$$

Proof. From the definition of the relaxed⁺ functional, and the fact that our volume constraint is closed for the weak L^2 convergence, we obtain our lim sup inequality. Notice that

$$F_\epsilon(\chi_\epsilon) \leq J(\chi_\epsilon) \leq \bar{J}(\chi_\epsilon),$$

thus, taking the necessary lim sup and noting that our relaxation is upper semicontinuous, we find that

$$\limsup_{\epsilon \rightarrow 0} F_\epsilon(\chi_\epsilon) \leq \bar{J}(\chi).$$

For the lim inf inequality, we apply the definition of our relaxed⁺ functional. For every $\chi \in \mathcal{X}^2$, there exists a sequence χ_η s.t. $\chi_\eta \rightharpoonup \chi$ with respect to the L^2 topology. Since $\chi_\eta \in H^1$ for any η , and that $C^\infty(\bar{\Omega})$ is dense in $H^1(\Omega)$ for our domain Ω , we can approximate each χ_η with a smooth function $\bar{\chi}_{\eta,\epsilon} \in C^\infty(\bar{\Omega})$ such that

$$\|\chi_\eta - \bar{\chi}_{\eta,\epsilon}\|_{H^1} \leq \epsilon,$$

for any $\epsilon > 0$.

We wish to show that each of these $\bar{\chi}_{\eta,\epsilon}$ can be approximated by a sequence of piecewise affine functions that, in the limit, have a vanishing gradient. We break up $\Omega = (0, 1) \times (0, 1)$ into a square grid with spacing $\epsilon^{1/4}$. We separate each of these elements further, where the interior region, I , takes on a constant value equal to $\bar{\chi}_{\eta,\epsilon}$ evaluated at the center point. On each of the four sides, we linearly interpolate between the neighboring constant regions areas denoted by II . For the corners, we interpolate between three neighboring cells over triangular regions so that we maintain continuity of our approximation.

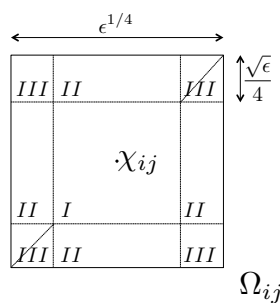


Figure A.1: A division for the piecewise affine approximation of $\bar{\chi}_{\eta,\epsilon}$.

There are two things that we must verify with this sequence $\chi_{\eta,\epsilon}$. One, we need to confirm that $\|\chi_{\eta,\epsilon} - \bar{\chi}_{\eta,\epsilon}\|_{L^2} \xrightarrow{\epsilon \rightarrow 0} 0$. Additionally, we must verify that in the limit of $\epsilon \rightarrow 0$, the gradient contribution to the Allen-Cahn functional vanishes.

We start by examining

$$\int_{\Omega} |\chi_{\eta,\epsilon} - \bar{\chi}_{\eta,\epsilon}|^2 dx = \sum_{i,j} \int_{\Omega_{ij}} |\chi_{\eta,\epsilon} - \bar{\chi}_{\eta,\epsilon}|^2 dx.$$

We know our continuously differentiable function $\bar{\chi}_{\eta,\bar{\chi}}$ also satisfies a (local) Lipschitz condition, i.e. there exists a nonnegative constant C such that

$$|\bar{\chi}_{\eta,\epsilon}(x) - \bar{\chi}_{\eta,\epsilon}(y)| \leq C\|x - y\|.$$

We apply this to a 3×3 grouping of elements, so that from the definition of $\chi_{\eta,\epsilon}$ we determine that there exists another constant such that

$$|\chi_{\eta,\epsilon}(x) - \bar{\chi}_{\eta,\epsilon}(y)| \leq C'\|x - y\|$$

for any x, y in this group of elements. By using the grid spacing we determine that

$$\begin{aligned} \int_{\Omega} |\chi_{\eta,\epsilon} - \bar{\chi}_{\eta,\epsilon}|^2 dx &= \sum_{i,j} \int_{\Omega_{ij}} |\chi_{\eta,\epsilon} - \bar{\chi}_{\eta,\epsilon}|^2 dx \\ &\leq \sum_{i,j} \int_{\Omega_{ij}} (C'\|x - y\|)^2 dx \\ &\leq \sum_{i,j} \int_{\Omega_{ij}} C'' (\epsilon^{1/4})^2 dx \\ &= C''\sqrt{\epsilon}. \end{aligned}$$

Thus, we have found that

$$\|\chi_{\eta,\epsilon} - \bar{\chi}_{\eta,\epsilon}\|_{L^2} \rightarrow 0.$$

Now, we look at the gradient contribution of the piecewise affine approximation by breaking up the domain into the various regions interpolations, *I*, *II*, *III*. Obviously, there is no contribution from region *I*, and then in regions *II*, where we linearly transition from the two neighboring cells, we end up with a contribution on the order of $(1/\sqrt{\epsilon})^2|II|$. The contribution of triangular regions *III*, where we interpolate between three separate values, can be bounded from above by a similar measure of the gradient. To aid in this, we combine the subdomains along each boundary of

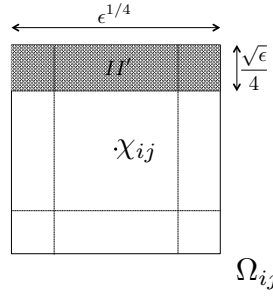


Figure A.2: Grouping regions II and III into linear transition regions II' .

the element, denoting them by I' , II' , III' , IV' . These regions are extensions of the regions II that interpolate between the two neighboring cells.

We start with

$$\begin{aligned}
 \int_{\Omega} \epsilon^2 |\nabla \chi_{\eta, \epsilon}|^2 dx &= \sum_{i,j} \int_{\Omega_{ij}} \epsilon^2 |\nabla \chi_{\eta, \epsilon}|^2 dx \\
 &= \sum_{i,j} \left(\int_{II} \epsilon^2 |\nabla \chi_{\eta, \epsilon}|^2 dx + \int_{III} \epsilon^2 |\nabla \chi_{\eta, \epsilon}|^2 dx \right) \\
 &\leq \sum_{i,j} \left(\int_{I'} \epsilon^2 |\nabla \chi_{\eta, \epsilon}|^2 dx + \int_{II'} \dots \right) \\
 &= \sum_{i,j} \left(\int_{I'} \epsilon^2 \left| \frac{2(\chi_{i-1,j} - \chi_{i,j})}{\sqrt{\epsilon}} \right|^2 dx + \int_{II'} \dots \right) \\
 &\leq 4M^2 \epsilon \sum_{i,j} \left(\int_{I'} dx + \int_{II'} dx + \dots \right) \\
 &= 4M^2 \epsilon \frac{1}{\sqrt{\epsilon}} \left(4 \frac{\sqrt{\epsilon}}{4} * \epsilon^{1/4} \right) \\
 &= 4M^2 \epsilon^{5/4}.
 \end{aligned}$$

We have used the fact our continuous approximation, $\bar{\chi}_{\eta, \epsilon}$, that provides the grid values χ_{ij} attains a maximum and minimum value over Ω and allows us to use the uniform bound, M . Accordingly, we have found that our piecewise affine sequence has a gradient contribution that vanishes in the limit $\epsilon \rightarrow 0$. At this point we have

that

$$\|\chi_{\eta,\epsilon} - \bar{\chi}_{\eta,\epsilon}\|_{L^2} \rightarrow 0$$

and

$$\|\chi_\eta - \bar{\chi}_{\eta,\epsilon}\|_{L^2} \rightarrow 0,$$

and thus, by the uniqueness of the L^2 limit,

$$\|\chi_\eta - \chi_{\eta,\epsilon}\|_{L^2} \rightarrow 0.$$

We obtain our recovery sequence, still denoted $\chi_{\eta,\epsilon}$, by applying a diagonal argument using the fact that $\chi_\eta \rightharpoonup \chi$ and $\chi_{\eta,\epsilon} \rightarrow \chi_\eta$, so that $\chi_{\eta,\epsilon} \rightharpoonup \chi$, with respect to the weak L^2 topology.

To appeal to the prescribed volume constraint, we have to modify $\chi_{\eta,\epsilon}$. We denote the volume average of our functions in question with

$$\begin{aligned} \frac{1}{|\Omega|} \int_{\Omega} \chi \, dx &= v \\ \frac{1}{|\Omega|} \int_{\Omega} \chi_{\eta,\epsilon} \, dx &= v_\epsilon \end{aligned}$$

We can modify $\chi_{\eta,\epsilon}$ only on $\Omega_\epsilon = (1 - \epsilon, 1) \times (0, 1)$ by setting

$$\chi_\epsilon(x, y) = \begin{cases} \chi_{\eta,\epsilon}(x, y) & \text{if } 0 < x \leq 1 - \epsilon \\ \chi_{\eta,\epsilon}(x, y) + \frac{2}{\epsilon}(v - v_\epsilon)(x - 1 + \epsilon) & \text{if } 1 - \epsilon < x \leq 1. \end{cases}$$

Moreover, we can verify that the modified recovery sequence also has the desired gradient behavior

$$\begin{aligned} & \lim_{\epsilon \rightarrow 0} \epsilon^2 \left| \int_{\Omega} (|\nabla \chi_{\eta,\epsilon}|^2 - |\nabla \chi_\epsilon|^2) \, dx \right| \\ &= \lim_{\epsilon \rightarrow 0} \epsilon^2 \left| \int_{\Omega_\epsilon} (|\nabla \chi_{\eta,\epsilon}|^2 - |\nabla \chi_\epsilon|^2) \, dx \right| \\ &\leq \lim_{\epsilon \rightarrow 0} \epsilon^2 \int_{\Omega_\epsilon} \left(\frac{2}{\epsilon} |\nabla \chi_{\eta,\epsilon}| |v - v_\epsilon| + \frac{4}{\epsilon^2} |v - v_\epsilon|^2 \right) \, dx = 0, \end{aligned}$$

Since we have showed that our recovery sequence χ_ϵ is suitable in that it has the desired gradient contribution and satisfies the volume constraint, we examine the

limit behavior of our function,

$$\begin{aligned}
\liminf_{\epsilon \rightarrow 0} F_\epsilon(\chi_\epsilon) &= \liminf_{\epsilon \rightarrow 0} \left(J(\chi_\epsilon) - \int_{\Omega} W_\epsilon(\chi_\epsilon) + \frac{\epsilon^2}{2} |\nabla \chi_\epsilon|^2 dx \right) \\
&\geq \liminf_{\epsilon \rightarrow 0} \left(J(\chi_\epsilon) - \int_{\Omega} W_\epsilon(\chi_\epsilon) dx \right) - \limsup_{\epsilon \rightarrow 0} \left(\int_{\Omega} \frac{\epsilon^2}{2} |\nabla \chi_\epsilon|^2 dx \right) \\
&= \liminf_{\epsilon \rightarrow 0} \left(J(\chi_\epsilon) - \int_{\Omega} W_\epsilon(\chi_\epsilon) dx \right) \\
&\geq \liminf_{\epsilon \rightarrow 0} J(\chi_\epsilon) - \limsup_{\epsilon \rightarrow 0} \left(\int_{\Omega} W_\epsilon(\chi_\epsilon) dx \right) \\
&\geq \liminf_{\epsilon \rightarrow 0} J(\chi_\epsilon) - \int_{\Omega} \limsup_{\epsilon \rightarrow 0} W_\epsilon(\chi_\epsilon) dx
\end{aligned}$$

What remains is showing the continuity of $J(\cdot)$ with respect to our recovery sequences to obtain the desired form of the Γ -limit. We make use the definition of χ_ϵ from χ_η to show that $J(\chi_\epsilon) \rightarrow J(\chi_\eta)$ as $\epsilon \rightarrow 0$. We have

$$|J(\chi_\epsilon) - J(\chi_\eta)| = \left| \inf_{u \in \mathcal{V}} L(u; \chi_\epsilon) - \inf_{u \in \mathcal{V}} L(u; \chi_\eta) \right|.$$

With $\bar{u}_\eta \in \mathcal{V}$ minimizing the latter of these functionals, we can use \bar{u}_η as a test function in the first functional to write

$$\begin{aligned}
|J(\chi_\epsilon) - J(\chi_\eta)| &\leq \left| L(\bar{u}_\eta; \chi_\epsilon) - L(\bar{u}_\eta; \chi_\eta) \right| \\
&= \left| \int_{\Omega} \frac{1}{2} \sum_{i=1,2} (k_i(\chi_\epsilon) - k_i(\chi_\eta)) |\nabla \bar{u}_\eta|^2 + \frac{k_s}{2} (\chi_\epsilon(1 - \chi_\epsilon) - \chi_\eta(1 - \chi_\eta)) \bar{u}_\eta \cdot A \bar{u}_\eta \right. \\
&\quad \left. - \lambda (\chi_\epsilon - \chi_\eta) dx \right| \\
&= \left| \int_{\Omega} \frac{1}{2} \sum_{i=1,2} (\chi_\epsilon - \chi_\eta) \Delta k_i |\nabla \bar{u}_\eta|^2 + \frac{k_s}{2} (\chi_\epsilon - \chi_\eta) (1 - (\chi_\eta + \chi_\epsilon)) \bar{u}_\eta \cdot A \bar{u}_\eta \right. \\
&\quad \left. - \lambda (\chi_\epsilon - \chi_\eta) dx \right| \\
&\leq \left\| \chi_\epsilon - \chi_\eta \right\|_{L^2} \left\| \frac{1}{2} \sum_{i=1,2} \Delta k_i |\nabla \bar{u}_\eta|^2 + \frac{k_s}{2} (1 - (\chi_\eta + \chi_\epsilon)) \bar{u}_\eta \cdot A \bar{u}_\eta - \lambda \right\|_{L^2}.
\end{aligned}$$

The last inequality follows from Hölder's inequality. Considering the properties of \bar{u}_η, χ_η and χ_ϵ we can bound the second norm on the right hand side by a suitable constant, c , independent of ϵ

$$|J(\chi_\epsilon) - J(\chi_\eta)| \leq c \left\| \chi_\epsilon - \chi_\eta \right\|_{L^2}.$$

Passing directly through the limit $\epsilon \rightarrow 0$ yields the desired result. With the chosen sequence χ_η , we can get arbitrarily close to the relaxation of $J(\cdot)$

$$\bar{J}(\chi) \leq J(\chi_\eta) + 1/\eta$$

for any index η . With our modified sequence, χ_ϵ , we can also get arbitrarily close to any χ_η , and it follows from the continuity of $J(\cdot)$ that

$$\bar{J}(\chi) \leq J(\chi_\epsilon) + \xi$$

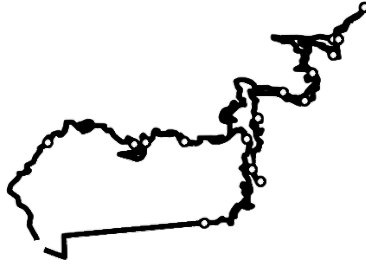
for any $\xi > 0$. Thus,

$$\bar{J}(\chi) \leq \liminf_{\epsilon \rightarrow 0} J(\chi_\epsilon).$$

Using the form of W_ϵ in the limit of $\epsilon \rightarrow 0$, we find that

$$\liminf_{\epsilon \rightarrow 0} F_\epsilon(\chi_\epsilon) \geq \begin{cases} \bar{J}(\chi) & \text{if } \chi \in [0, 1] \\ -\infty & \text{else.} \end{cases}$$

□



DFL >> DNF